

Effect of Styrene Butadiene Rubber Latex on Mechanical Properties of Eco Concrete: Limestone Powder Concrete • Radon Concentration in the Work Atmosphere of Cement Plants in the Sulaymaniyah Area, Iraq • The Use of Quadtree Range Domain Partitioning with Fast Double Moment Descriptors to Enhance FIC of Colored Image • Facial Expression Recognition Using Uniform Local Binary Pattern with Improved Firefly Feature Selection • Synthesis and Characterization of Iron(II), Cobalt(II), Nickel(II), Copper(II), and Zinc(II) Complexes Using Diphenylmethyl Xanthate Ligand • Synthesis and Antibacterial Activity of Isatin Schiff Base Derivative with 3-Aminoacetophenone and its Ni(II), Co(II) Transition Metals Complexes • Evaluating the Wear of Polycrystalline Diamond Compact Drill Bit Cutters using Indentation and Scratch Tests • A Hybrid of Artificial Bee Colony, Genetic Algorithm, and Neural Network for Diabetic Mellitus Diagnosing • Solid-works Simulation of Mechanical Properties of Recycled Plastics/Nanocomposite Faces Sandwich Panels • Determination of Natural Radioactivity and Radiological Hazards of ^{226}Ra , ^{232}Th , and ^{40}K in the Grains Available at Penang Markets, Malaysia, Using High-purity Germanium Detector

ARO-The Scientific Journal of Koya University

The ARO (“Today” in Hewramí Kurdish), is an international scientific journal published by the Koya University with p-ISSN: 2410-9355, e-ISSN: 2307-549X and DOI: 10.14500/2307-549X. ARO is a journal of original scientific research, global news, and commentary. The ARO Scientific Journal is a peer-reviewed, open access journal that publishes original research articles as well as review articles in all areas of Science.



ARO Executive Publisher

Dr. Wali M. Hamad; is the President of Koya University and the Executive Publisher of ARO.

ARO Editorial Board

The Editorial Board of ARO includes an eight-member Senior Executive Editorial Board and a seven-member Associate Editorial Board that help in setting journal policy; a Board of Reviewing Editors consisting of more than 210 leading scientists.

ARO Editorial Group

Senior Executive Editors: Dilan M. Rostam, Salah I. Yahya, Basim M. Fadhil, Fahmi F. Muhammad, Mohammed H. Zangana, Jorge Correia, Fouad Mohammed.

Associate Editors: Hamed M. Jassim, Husein A.H. Shekhhzainy, Iqbal M.G. Tahir, Saddon T. Ahmad, Sahar B. Mahmood, Tara F. Tahir and Yazan A. Khaleel.

This issue reviewers: Adil M. Hussein, Ahmed S. Mohammed, Akram Humoodi, Asaad H. Ismail, Bakhtyar K. Aziz, Bisan Al-Salibi, Bo Liu, Diyari I. Tofiq, Fami F. Muhammad, Faraidoon K. Kadir, Hamed M. Jassim, Jameela Harbi, Nada S. Salman, Rafea I. Yahya, Saddon T. Ahmad, Salah I. Yahya, Tara F. Tahir, Wasan A. Hashim and Wissam K. Alsaraj.

ARO Editorial Web and New Media: Dilan M. Rostam and Salah I. Yahya

Secretarial Office of the Journal: Haneen H. Falah

Journal Proofreader: Salah I. Yahya

ARO, the International journal of original scientific research and commentary is an online and published twice a year, as well, by Koya University. The published articles are free and online open access distributed under the Creative Commons Attribution License (CC BY-NC-SA 4.0: <https://creativecommons.org/licenses/by-nc-sa/4.0/>). Responsibility of the content rests upon the authors and not upon ARO or Koya University.

ARO the Scientific Journal Office

Koya University, University Park
Danielle Mitterrand Boulevard, Koya KOY45
Kurdistan Region - F.R. Iraq

Tel.: +964 (0) 748 012 7423

Mobile: +964 (0) 750 187 5489

E-mail: aro.journal@koyauniversity.org

url: aro.koyauniversity.org

June - 2018 | Poshper – 2718

ARO

The Scientific Journal of Koya University

Vol VI, No 1(2018)

Contents

Aro Editorial Words	iii
Bayan S. Al Numan, Faris R. Ahmed, Kamaran K. Hamad	01
Effect of Styrene Butadiene Rubber Latex on Mechanical Properties of Eco Concrete: Limestone Powder Concrete	
Adil M. Hussein, Kamal O. Abdullah, Kharman A. Faraj, Dara F. Hamamin	07
Radon Concentration in the Work Atmosphere of Cement Plants in the Sulaymaniyah Area, Iraq	
Bushra A. Sultan, Loay E. George, Nidaa F. Hassan	13
The Use of Quadtree Range Domain Partitioning with Fast Double Moment Descriptors to Enhance FIC of Colored Image	
Abdulla M.K. Elmadhoun, Md Jan Nordin	23
Facial Expression Recognition Using Uniform Local Binary Pattern with Improved Firefly Feature Selection	
Aeed S. Al-Fahdawi, Eman I. Alsalihi	33
Synthesis and Characterization of Iron(II), Cobalt(II), Nickel(II), Copper(II), and Zinc(II) Complexes Using Diphenylmethyl Xanthate Ligand	
Eman I. Alsalihi, Aeed S. Al-Fahdawi	38
Synthesis and Antibacterial Activity of Isatin Schiff Base Derivative with 3-Aminoacetophenone and its Ni(II), Co(II) Transition Metals Complexes	
Rafid K. Abbas, Ali R. Hassanpour	46
Evaluating the Wear of Polycrystalline Diamond Compact Drill Bit Cutters using Indentation and Scratch Tests	
Tarik A. Rashid, Saman M. Abdullah	55
A Hybrid of Artificial Bee Colony, Genetic Algorithm, and Neural Network for Diabetic Mellitus Diagnosing	
Ahmad T. Azeez, Serwan S. Mohammed	65
Solidworks Simulation of Mechanical Properties of Recycled Plastics/Nanocomposite Faces Sandwich Panels	
Najeba F. Salih	71
Determination of Natural Radioactivity and Radiological Hazards of ²²⁶ Ra, ²³² Th, and ⁴⁰ K in the Grains Available at Penang Markets, Malaysia, Using High-purity Germanium Detector	
General Information	79
Guide to Author	80
Aro Reviewer/Associate Editor Application Form	82

ARO Editorial Words

Dear readers, ARO-the Scientific Journal of Koya University is closing its tenth issue (Vol VI, No 1, 2018) after an exciting yet dynamic season of valuable inputs by our research community and supportive reviewers. ARO is publishing its 5th issue as an internationally listed Scientific Journal in Kurdistan Region of Iraq. Notably, ARO has been accepted for indexing in the Emerging Sources Citation Index (ESCI), a new edition of Web of Science™ as of Feb 2016. Content in this index is under consideration by Thomson Reuters to be accepted in the Science Citation Index Expanded™ (SCIE). ARO's individual articles are currently listed by Thomson Reuters using articles unique DOI numbers which is a historical achievement for our academic community. ARO is starting its sixth year journey in leading the quality of regional scientific publications with global impact. The editorial team has been working tirelessly to keep the novel mission and sustain ARO's future publications with greater impacts and citations. It is exciting that ARO has been awarded to DOAJ Seal listing which is an indication of a trusted high standard open access scientific work that so far haven allocated to 88 journals worldwide only. The upcoming new season will be an even more exciting period in ARO's life as Thomson Reuters will examine our journal for full permanent listing.

Despite all ongoing regional conflicts and economic downturn which still having a great impact on scientific research activities and funding of the regional universities in general and Koya University in particular, ARO is continuing to receive great numbers of well-motivated quality papers which shows its steadily growing trust among researchers in the region, demanding the increased volume of publication. Nevertheless, ARO is finding more focus in applied sciences with research values in current regional issues having International impacts.

ARO was created with long-term visions of becoming accessible to all researchers in Kurdistan and beyond, and covering a wide range of scholarly disciplines in sciences. ARO is a peer-reviewed, open access journal that publishes original scientific research, global news, letters and commentary as well as review articles in areas of natural sciences and technology. In this issue you will have access to original research papers in variety of areas, such as Physics, Biochemistry, Materials Science and Petroleum, Chemical and other fields of Engineering.

The great responses from researchers, academics and professionals in the last five years have made us to create a wider Editorial Board which serves the wider submitted scientific manuscripts. However, it is clear that having a dedicated and well organized editorial board for the journal is only one side of the coin. The other is the ability to attract submissions of quality research and scholarly work. We are thankful to all of those who put their trust in ARO and presented their original research work for publication in Vol VI, No 1 (2018) of the journal, as well as, our thanks are extended to the 19 peer-reviewers from the Universities worldwide for their efforts in reviewing and enabling this issue of ARO.

Your support and feedback are invited and appreciated.

Dilan M. Rostam
Editor-in-Chief

Wali M Hamad
Executive Publisher

Dilan M. Rostam, Salah I. Yahya, Basim M. Fadhil, Fahmi F. Muhammad, Mohammed H.S. Zangana, Jorge Correia and Fouad Muhammad
Executive Editorial Board

Effect of Styrene Butadiene Rubber Latex on Mechanical Properties of Eco Concrete: Limestone Powder Concrete

Bayan S. Al Numan¹, Faris R. Ahmed² and Kamaran K. Hamad³

¹Department of Civil Engineering, Faculty of Engineering, Ishik University, Erbil, Kurdistan Region - F.R. Iraq

²Department of Civil Engineering, Faculty of Engineering, Koya University, Kurdistan Region - F.R. Iraq

³Department of Geomatics (Surveying) Engineering, College of Engineering, Salahaddin University, Erbil, Kurdistan Region - F.R. Iraq

Abstract—To make concrete a truly green material, viable cement substitutes are available. This experimental investigation is performed to study the effect of using limestone powder (LSP) and styrene butadiene rubber (SBR) latex in the concrete mix. In this work, a concrete with 1:1.8:3 cementitious material:sand:gravel and water/cement ratio w/c of 0.5 is produced. First, LSP is used with 0, 5, 10, 15, and 20% replacements by weight of cements. The fineness of the LSP is measured using sieve No. 200 and showed about 30% pass. Second, and to improve the matrix of concrete due to the dilution effect, four ratios of SBR latex (0, 5, 10, and 15%) are added by weight of cements to the mix for each LSP ratio. Compressive strength at ages of 3, 7, 14, 28, and 90 days is tested for the concrete specimens mixed with LSP only to examine its effect on concrete strength's development with time, whereas strengths are recorded at the age of 28 days for the other concretes. Three prisms were cast for each ratio and tested at 28 days. The results show general improvements in terms of compressive and flexural strengths.

Index Terms—Compressive strength, Flexural strength, Limestone filler, Portland cement, Styrene butadiene rubber latex.

I. INTRODUCTION

It has been proved that every ton of cement produced leads to about 0.9 ton of CO₂ emissions and a typical cubic meter of concrete contains about 10% by weight of cement, that leads to about quarter tons of CO₂ (Obla, 2009). Many studies have been written about reducing the CO₂ emissions from concrete primarily through the reduction of amounts of cement used in concrete and replacing it with supplementary cementitious material (CM) such as

limestone powder (LSP), fly ash, polymers, nano-silica, and slag.

LSP and styrene butadiene rubber (SBR) latex have been used widely with many effects on the cement properties due to its action as a filler or binder between the concrete particles and producing a denser paste and densifying the interfacial zone between the aggregate and cement paste.

II. PREVIOUS WORKS ON LSP CONCRETE

The performance of LSP filler addition to Portland cement has been studied in pastes, mortars, and concretes. In general, limestone filler improves the hydration rate of cement compounds and consequently increases the strength at early ages. Tarun, et al., 2003, states that LSP filler in concrete leads to dilution of cement, high effective w/c ratio, and increases the strength at early ages. The use of LSP in concrete provides environmental and economic advantages by reducing Portland cement production and hence CO₂ emission, as well as improving the early and the later age compressive strength.

Ahmed, et al., 2009, discussed the effect of increasing temperature, when part of cement is replaced by LSP, on the compressive and tensile strength of concrete. Several LSP ratios were used (0, 10, 15, 20, and 25%) as compensating material. The temperature elevated to 200, 400, and 600°C. It has been concluded that when LSP ratio exceeds 15%, both compressive and tensile strength is reduced, and when exposed to high temperature, severe drop in concrete strengths occurs in different forms.

Thongsanitgarn, et al., 2011 studied the behavior of Portland cement paste when part of cement is replaced by LSP with percentages of 0, 5, 7.5, 10, 12.5, 15 and 20% by weight with three degrees of fineness for each percentage. The study covered the effect of LSP on the compressive strength and setting time of concrete. It has been concluded that replacing cement by LSP caused reduction in compressive strength and increasing the fineness of LSP will increase it but it would require more water. Both initial and final setting times were decreased with the increase of the LSP amount.

ARO-The Scientific Journal of Koya University
Volume VI, No 1(2018), Article ID: ARO.10212, 6 pages
DOI: 10.14500/aro.10212

Received 16 March 2017; Accepted 15 January 2018
Regular research paper: Published 18 February 2018

Corresponding author's e-mail: faris.rashied@koyauniversity.org
Copyright © 2018 Bayan S. Al Numan, Faris R. Ahmed and
Kamaran K. Hamad. This is an open access article distributed under
the Creative Commons Attribution License.



III. PREVIOUS WORKS ON POLYMER MODIFIED CONCRETE

The use of SBR emulsions in concrete has been increasing in concrete construction and repair work due to its benefits to flexure strength, adhesion, and impermeability.

Essa, et al., 2102, studied the effect of adding SBR on both cement paste and concrete. Several ratios chosen from 10% to 35% by volume of water were used to study the early and late strength of concrete. It has been concluded that adding SBR has a considerable negative effect on the early strength of concrete, but it has a positive effect for later ages. In addition, it showed an increase in compressive strength with increasing the added dosage of SBR. Furthermore, adding of SBR to concrete mix caused an increase in flexural strength at 28 days by 7%, 33%, and 53% for SBR dosage of 10%, 25%, and 35%, respectively.

Yao and Ge, 2012, evaluated the influence of different contents (0, 5, 10, 15, and 20% by cement) of SBR on the mechanical properties of concrete with the same w/c ratio. The compressive strength, flexure strength, permeability, and elastic modulus were studied. Experimental results showed that the compressive strength, elastic modulus, and permeability were decreased when SBR latex ratio increased while the flexural strength increased.

IV. MATERIAL AND EXPERIMENTAL PROGRAM

A. Cement

During the preparation of the mix, ordinary Portland cement (OPC) provided by Tassluja factory in Sulaymaniyah, Iraq, was used. The chemical composition and the physical properties of the cement are illustrated in Table I and it is conforming to the Iraqi specification IQS No. 5-1984.

B. SBR Latex

A milky-white fluid locally available by Sika-Synthetic Rubber Latex, as shown in Fig. 1, was used as SBR latex to produce latex-modified concrete. Table II presents that the SBR used complies with ASTM C1042 and C1059-99, Type I, redispersible bonding admixture.



Fig. 1. Styrene butadiene rubber used in the present work.

C. Fine Aggregate (Sand)

Natural sand is used throughout this work with the maximum size of 4.75 mm. The grading of the sand was conformed to the Iraqi specification No. 45/1984. Table III presents the sieve analysis of the fine aggregate used.

D. Coarse Aggregate

Natural river gravel with irregular shape is used with a maximum size of 12.5 mm for all mixes. The gravel was

TABLE I
CHEMICAL COMPOSITIONS AND PHYSICAL PROPERTIES OF PORTLAND CEMENT

Oxide		% by weight	IQS 5:1984 limits
Lime	CaO	62.13	-
Magnesia	MgO	2.24	≤5
Silica	SiO ₂	22.1	-
Sulfate	SO ₃	1.07	≤2.5 if C3A <5% ≤2.8 if C3A >5%
Iron oxide	Fe ₂ O ₃	3.53	-
Alumina	Al ₂ O ₃	5.49	-
Loss on ignition	LOI	1.45	≤4
Insoluble residue	IR	0.32	≤1.5
Lime saturation factor	LSF	0.86	0.66-1.02
Main compounds (Bogue's equation)			
Tricalcium silicate	C3S	38.55	
Dicalcium silicate	C2S	33.15	
Tricalcium aluminate	C3A	8.58	
Tetracalcium aluminoferrite	C4AF	10.73	
Physical properties		Test result	
Specific surface area (blain) cm ² /g		310	≥250
Soundness using autoclave method		0.19%	≤0.8
Initial setting (Vicat method) min		165	≥45
Final setting (Vicat method) h		04:05	≤10
Compressive strength (MPa)			
3 days		16.5	≥15
7 days		25.7	≥23

LOI: Loss on ignition, IR: Insoluble residue, LSF: Lime saturation factor

TABLE II
SBR LATEX USED IN THIS STUDY

Physical properties	Test result	ASTM limits
Density	Approx. 1 kg/L	
Solid content	Approx. 47%	
pH value	Approx. 10	
Compressive strength		
7 days	35 MPa	
28 days	45 MPa	≥31
Tensile strength		
7 days	3.5 MPa	
28 days	3.7 MPa	
Bond strength		
7 days	2.5 MPa	
28 days	3.0 MPa	≥2.8
Flexural strength		
7 days	6.0 MPa	
28 days	7.0 MPa	
Shrinkage (28 days)	Approx. <500 μm/m	
Elastic modulus (28 days)	Approx. 15 kN/mm ²	

washed, then stored in air to dry the surface, and then stored in containers in a saturated surface dry condition before using. Table IV shows the sieve analysis of the coarse aggregate used.

E. Mixing Water

Throughout the investigation, tap water supplied for drinking consumption was used for concrete mixing and curing the hardened concrete samples.

F. Limestone Filler

Limestone used consists essentially of calcium carbonate and generally with some magnesium carbonate and siliceous matter such as quartz grains. The limestone may be composed of four minerals: Calcite (CaCO₃), aragonite, dolomite (CaMg (CO₃)₂), and magnesite (MgCO₃) (Noori, 2016). Table V presents the specifications of LSP and it is conforming to the ASTM C150 standard.

G. Mix Preparation

The work was divided into two series; the first one is to study the effect of LSP on concrete physical properties (Table VI), whereas the second is to study the effect of

adding SBR latex to the concrete containing LSP (Table VII). For both series, constant concrete mix ratios were used in the experimental program, which are (W+SBR)/CM ratio of 0.5, and varying ratios of LSP/CM ratios of 0%, 5%, 10%, 15, and 20%, SBR/CM (0%, 5%, 10%, and 15%) with S/CM ratio of 1.8, and G/CM ratio of 3 as shown in Tables VI and VII.

First, LSP quantity was weighed, then water quantity was calculated by subtracting SBR quantity from the needed volume. The LSP was added to the mix with cement before adding the water, whereas the SBR latex was added to the water and mixed well before using. The quantity of cement needed was measured by subtracting the LSP quantity from total CM needed (350 kg/m³).

The cubes and prisms molds were prepared, oiled, and cast. Then, specimens were demolded after 24 h and cured in room temperature water. Three cubes and three prisms were cast for each ratio except for the 0% SBR, for which 15³ were cast to be tested at 3, 7, 14, 28, and 90 days to examine the LSP effect on early and longtime stages.

H. Samples Specifications

A total of 111 cubes were tested in compression and 51 prisms in flexure were designed to study all parameters in addition to the control mix made without limestone fines or SBR. Limestone fines were added in different percentages ranging from 0.0% to 20%, whereas SBR was ranging from 0.0% to 15% and both with 5% increments. All cubes were 100 mm in dimensions and all prisms were of size 100 mm × 100 mm × 450 mm with tested span of 400 mm.

I. Curing

All prisms and cubes are kept in a curing water tank to the test day, and then, they were taken out of water and tested after 1 h (Fig. 2).

J. Test Set-up

All the cubes were tested using standard testing machine (AUTOMAX5 made by CONTROL Group, as shown in Fig. 3a) with a capacity of 2000 kN. The test was conducted at ages of 3, 7, 14, 28, and 90 days. Each result of compressive strength obtained is the average for three specimens. The load was applied at a rate of 0.8 MPa/min.

TABLE III
SIEVE ANALYSIS OF FINE AGGREGATE

Sieve opening (mm)	% pass	Limits of Iraqi specification, No. 45/1984 zone 2
4.75	99.9	90-100
2.36	84.8	75-100
1.18	72.2	55-90
0.6	34.6	35-59
0.3	10.7	8-30
0.15	2.2	0-10
0.075	0.6	≤5%

TABLE IV
SIEVE ANALYSIS OF COARSE AGGREGATE

Sieve opening (mm)	% pass	Limits of Iraqi specification, No 45/1984 zone 2
12.5	100	35-70
9.5	96.5	
4.75	15.1	10-40
2.36	0.5	

TABLE V
CHEMICAL COMPOSITIONS AND PHYSICAL PROPERTIES OF LSP

Mat	Percentage	ASTM C150 limits
CaO	52.60	
MgO	1.446	≤6
SiO ₂	2.701	
SO ₃	0.170	≤3.0
Fe ₂ O ₃	0.395	
Al ₂ O ₃	1.196	
P ₂ O ₅	0.035	≤0.1
Na ₂ O	0.042	
K ₂ O	0.070	
MnO	0.005	
CaCO ₃	93.94	



Fig. 2. Some of cubes and prisms during curing.

Flexural strength test was done by third-point loading method as shown in Fig. 3(c). Prisms were tested for flexure in universal testing machine of capacity 100 kN (using ALPHA machine, as shown in Fig. 3b). The bearing surfaces of the supporting and loading rollers were wiped clean before loading. The prisms were placed in the machine in such a manner that the load was applied to the bottommost surface along the two lines spaced 40 cm apart. The axis of the specimen was aligned with the axis of the loading device. The load was applied at a rate of 2 mm/min. The specimen was loaded till it fails and the maximum load (P) applied to the specimen during test was recorded.

V. EXPERIMENTAL RESULTS AND DISCUSSION

A. Compressive Strength

Series I

Compressive strength measurements were carried out at ages of 3, 7, 14, 28, and 90 days. The compressive strength of LSP concrete was calculated from the average of three specimens and plotted as a function of limestone content. Fig. 4 shows the compressive strength of LSP concrete with time. The compressive strength is obviously related to the limestone content. It is found that the compressive strength of all LSP concrete specimens is lower than those of OPC control and decreased with increasing limestone content.

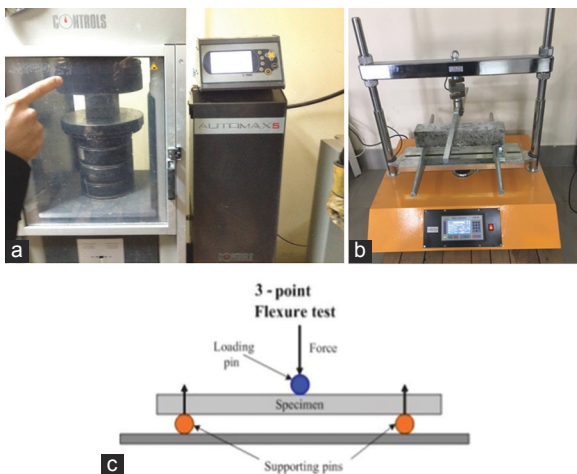


Fig. 3. Compression and flexural testing machines. (a) Testing compression machine, (b) testing flexural machine, (c) flexural test illustration.

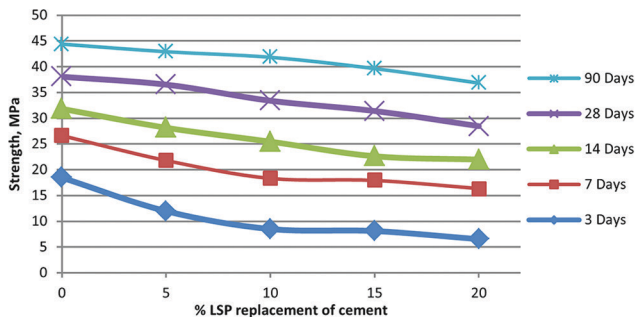


Fig. 4. Concrete compressive strength with limestone powder content.

The replacement of Portland cement by LSP caused a reduction in the compressive strength that can be explained as a result of cement dilution effect. It is indicated that the filler effect cannot compensate for the dilution effect at all ages. It was also found that all LSP concrete specimens show an increase in compressive strength with increasing curing time. Fig. 5 shows the compressive strength of LSP concrete at 3, 7, 14, 28, and 90 days of curing.

It has been found that addition of LSP into concrete improves the late strength such that the ratio of $f_{c90 \text{ days}}/$

TABLE VI
IDENTIFICATION AND MIX PROPORTIONS OF SERIES I

No.	ID	LSP (%)	CM	(W+SBR) CM	C	S CM	G CM
1	L00P00	0	1.0	0.5	1	1.8	3
2	L05P00	5	1.0	0.5	0.95	1.8	3
3	L10P00	10	1.0	0.5	0.9	1.8	3
4	L15P0.0	15	1.0	0.5	0.85	1.8	3
5	L20P00	20	1.0	0.5	0.8	1.8	3

C: Cement, P: SBR: Styrene butadiene rubber, W: Water, S: Sand, G: Gravel, LSP: Limestone powder, CM: C+LSP, Cementitious material content (CM) for all mixes was 350 kg/m³ all ratios are per weight for each line, 15 cubes and 3 prisms were cast.

TABLE VII.
IDENTIFICATION AND MIX PROPORTIONS OF SERIES II

No	ID	LSP (%)	SBR (%)	CM	(W+SBR) CM	C	S CM	G CM
1	L00P00	0	0	1.0	0.5	1	1.8	3
2	L00P05		5	1.0	0.5	1	1.8	3
3	L00P10		10	1.0	0.5	1	1.8	3
4	L00P15		15	1.0	0.5	1	1.8	3
5	L05P00	5	0	1.0	0.5	0.95	1.8	3
6	L05P05		5	1.0	0.5	0.95	1.8	3
7	L05P10		10	1.0	0.5	0.95	1.8	3
8	L05P15		15	1.0	0.5	0.95	1.8	3
9	L10P00	10	0	1.0	0.5	0.9	1.8	3
10	L10P05		5	1.0	0.5	0.9	1.8	3
11	L10P10		10	1.0	0.5	0.9	1.8	3
12	L10P15		15	1.0	0.5	0.9	1.8	3
13	L15P0.0	15	0	1.0	0.5	0.85	1.8	3
14	L15P05		5	1.0	0.5	0.85	1.8	3
15	L15P10		10	1.0	0.5	0.85	1.8	3
16	L15P15		15	1.0	0.5	0.85	1.8	3

Cementitious material content (CM) for all mixes was 350 kg/m³ LSP is a cement replacement ratio, whereas SBR is a water replacement ratio for each line, 3 cubes and 3 prisms were casted. LSP: Limestone powder, CM: Cementitious material, SBR: Styrene butadiene rubber

TABLE VIII
CONCRETE COMPRESSIVE STRENGTH (MPa) VARIATION WITH LSP AND SBR CONTENTS OF SERIES II

Lime	SBR			
	P00	P05	P10	P15
L00	38.06	35.03	32.32	30.26
L05	36.54	32.21	30.42	27.02
L10	33.41	30.44	27.01	25.24
L15	31.41	28.00	25.29	22.56

LSP: Limestone powder, SBR: Styrene butadiene rubber

fc28 days was 1.17 for the OPC, whereas it was 1.20, 1.25, 1.27, and 1.30 for LSP ratios of 5, 10, 15, and 20%, respectively. In other words, and as shown in Fig. 4, the drop in strength for late ages is less than the ones for early ages.

Series II

Compressive strength measurements at the age of 28 days are listed in Table VIII. The compressive strength of LSP concrete was calculated from the average of three specimens and plotted as a function of SBR content in Fig. 6 and plotted as a function of LSP content in Fig. 7.

As in Series I, the compressive strength is found to be decreased when SBR content increased. It has been found that addition of SBR into concrete by 5, 10, and 15% will slightly reduce the compressive strength by 10, 17, and 25%

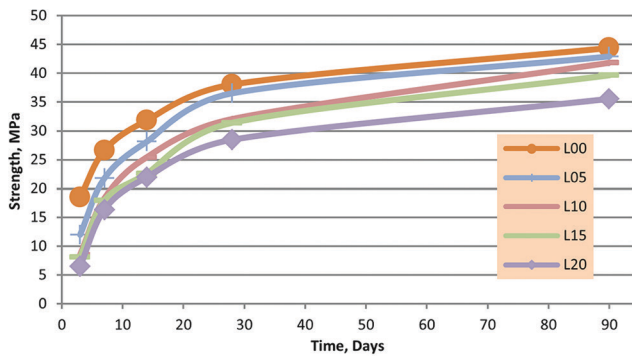


Fig. 5. Compressive strength of limestone powder concrete with time.

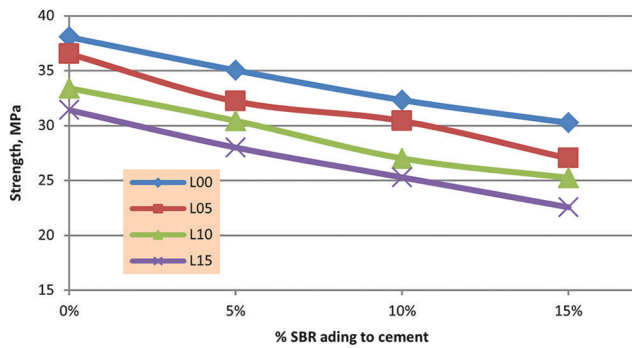


Fig. 6. 28-day compressive strength versus styrene butadiene rubber ratio of limestone powder concrete.

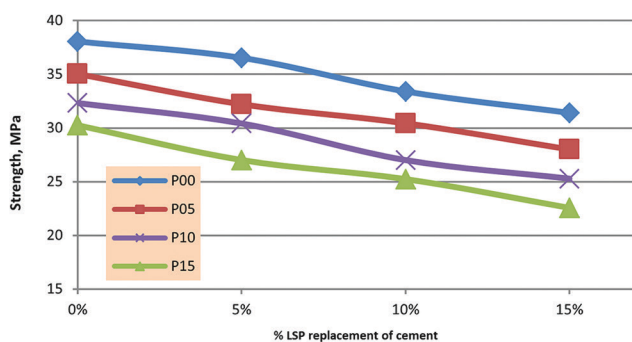


Fig. 7. 28-day compressive strength versus limestone powder ratio of polymer modified concrete.

in average for LSP content, respectively, as shown in Fig. 6. It is worth to mention that these results are consistent with other works, like Yao and Ge, 2012; Wang, et al., 2005; Abd Elkam and Abd Elmoaty, 2012 on their polymer modified concrete work.

B. Flexural strength

Series I

For evaluating the flexural strength, beam specimens of dimensions 100 mm × 100 mm × 450 mm were prepared. For testing, simple beam with third-point test was adopted on an effective span of 400 mm as per ASTM C 78-02. The test results are plotted in Fig. 8. It is seen that the 28-day flexural strength decreased up to 16% with LSP replacement of cement by 20% as shown.

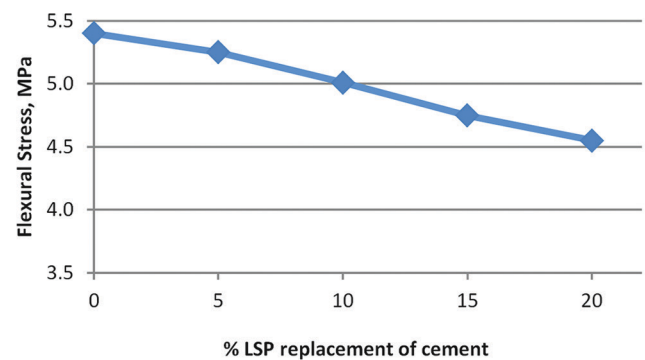


Fig. 8. Flexural strength of 28 days versus limestone powder content.

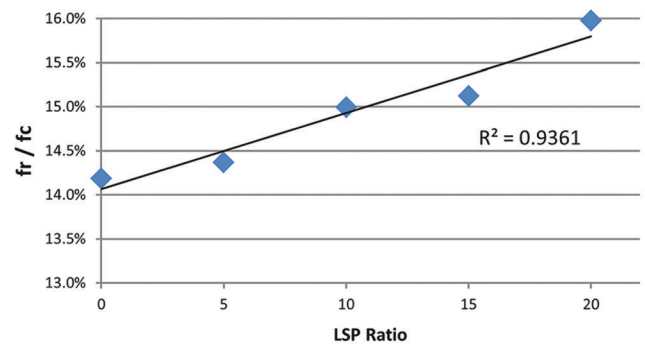


Fig. 9. Ratio f_c'/f_r versus limestone powder content at 28 days age.

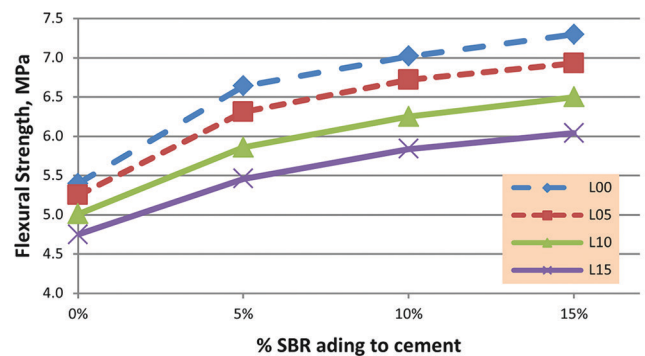


Fig. 10. Influence of styrene butadiene rubber latex on the flexural strength of concrete.

TABLE IX
CONCRETE FLEXURAL STRENGTH (MPA) VARIATION WITH LSP AND SBR
CONTENTS OF SERIES II

Lime	SBR			
	P00	P05	P10	P15
L00	5.40	6.64	7.02	7.30
L05	5.25	6.31	6.72	6.93
L10	5.01	5.86	6.25	6.50
L15	4.75	5.46	5.84	6.04

LSP: Limestone powder, SBR: Styrene butadiene rubber

Furthermore, when increasing LSP content, the ratio of flexural tensile strength to compressive strength (f_r/f_c) increased from 14.2% to about 16%, as shown in Fig. 9.

Series II

Table IX and Fig. 10 illustrate the effect of SBR content on the flexural strength of concrete. The results showed that the flexural strength of the concrete increased when the SBR content increased. In general, adding 5, 10, and 15% of SBR increased the flexural strength by 23, 30, and 35% for zero LSP content. This ratio decreased when LSP content increased and become 15, 23, and 27% for 15% LSP content.

This improvement in flexural behavior happened because the SBR enhances the bonding of the interface between Portland cement paste and aggregate.

For the f_r/f_c ratio, it is increased from 15% to 26% in general with insignificant effect toward the LSP content.

VI. CONCLUSIONS

Several conclusions have been recorded in this study for adding LSP or SBR into the concrete mix. The following conclusions can be drawn from the obtained experimental data:

1. Strength development of LSP concrete is either similar to or little slower than that of normal concrete. The ratio of 7/28 days was about 60% in average for LSP concrete and 70% for normal concrete.
2. Using LSP has reduced the 28 days cubes concrete strength by about 4, 12, 17, and 25% when replacing cement by 5, 10, 15, and 20%, respectively.
3. Further to point (2), the compressive strength (from 7 to 90 days) of LSP concrete was decreased with the increasing amount of limestone due to the dilution effect.
4. Using LSP has reduced the 28 days flexural strength by about 4, 8, 12, and 16% when replacing cement by 5, 10, 15, and

20%, respectively.

5. Using SBR latex has reduced the 28 days compressive strength by about 10, 17, and 25% when adding SBR latex by 5, 10, and 15%, respectively, in average for all LSP content.
6. Using SBR latex has increased the 28 days flexural strength by about 19, 27, and 31% when adding SBR by 5, 10, and 15%, respectively.

REFERENCES

- Abd Elkam, A.A., Abd Elmoaty, A.E., 2012. Experimental investigation on the properties of polymer modified SCC, Jr. *Construction and Building Materials*, 34, pp.584-592.
- Ahmed, A., Abdurrahman, A. and Mohammed, Z., 2009 Influence of limestone powder as partial replacement of cement on concrete and the effect of high temperature on it, *IASJ. Al-Rafidain Engineering Journal*, 18(5), pp.24-34.
- ASTM C1042-99, 1999. *Standard Test Method for Bond Strength of Latex Systems used with Concrete by Slant Shear (Withdrawn 2008)*. ASTM International, West Conshohocken.
- ASTM C1059/C1059M-99, 1999. *Standard Specification for Latex Agents for Bonding Fresh To Hardened Concrete*. ASTM International, West Conshohocken.
- ASTM C150/C150M-02, 2002. *Standard Specification for Portland Cement*. ASTM International, West Conshohocken.
- Essa, M., Abdul-Amir, A. and Hassan, N., 2012. Effect of ading (SBR) on concrete properties and bond between old and new concrete. *Kufa Journal of Engineering*, 4(1), pp.81-95.
- Noori, Z., 2016. Compaction and shear behaviour of low plasticity clayey soils treated by crushed lime. *International Journal of Engineering Technology, Management and Applied Sciences*, 4(6), pp.193-199.
- Obla, K. H., "What is Green Concrete," *Concrete InFocus*, V. 8, No. 2, Spring 2009. Available from: https://www.nrmca.org/research_engineering/Documents/What_is_Green_Concrete.pdf. [Last accessed on 2016 Sep 26].
- Tarun, R., Canpolat, F. and Chun, Y., 2003. Limestone Powder Use in Cement and Concrete, Report No. CBU-2003-31, REP-525. Available from: <http://www4.uwm.edu/cbu/Papers/2003%20CBU%20Reports/REP-525.pdf>. [Last accessed on 2016 Nov 10].
- Thongsanitgarn, P., Wongkeo, W., Sinthupinyo, S. and Chaipanich, A., 2011. *Effect of Limestone Powders on Compressive Strength and Setting Time of Portland-Limestone Cement Pastes*. Tiche International Conference 2011, November 10-11, At Hatyai, Songkhla Thailand.
- Wang, R., Wang, M. and Li, X.G., 2005. Physical and mechanical properties of styrene-butadiene rubber emulsion modified cement mortars. *Journal Cement and Concrete Research*, 35, pp.900-906.
- Yao, S. and Ge, Y., 2012. Effect of styrene butadiene rubber latex on mortar and concrete properties. *Advanced Engineering Forum*, 5, pp.283-288.

Radon Concentration in the Work Atmosphere of Cement Plants in the Sulaymaniyah Area, Iraq

Adil M. Hussein¹, Kamal O. Abdullah¹, Kharman A. Faraj¹, Dara F. Hamamin²

¹Advance Nuclear Laboratory, Physics Department, College of Science, University of Sulaimani, Kurdistan Region – F.R. Iraq

²Department of Geology, College of Science, University of Sulaimani, Sulaimani, Kurdistan Region – F.R. Iraq

Abstract–This work reports the radon concentration level in the work environment of cement plants (CPs) located in the Sulaymaniyah city-North of Iraq. This survey for the radon concentration is performed in 24 sectors of three different CPs including Tasluja, Mass, and Bazian. The measurements were recorded using solid state nuclear track detector (CR-39 NTDs). The radon effective dose $\mu\text{Sv/hr}$ correlated weakly with the gamma effective dose $\mu\text{Sv/hr}$ to enhance the radon concentration measuring. The detector was fixed in different places of the plants such Crusher, Correction stores, Raw Mill (Grinding Mill), Preheater (Tower), Clinker, and Cement Storage. The arithmetic mean (AM) value of radon concentration (C_a) was found to be 98 ± 9 , 101 ± 10 , and $125 \pm 10 \text{ Bq m}^{-3}$ and the arithmetic mean value of annual effective dose (E) of radon was 0.767, 0.753, and 0.962 mSv y^{-1} for Tasluja, Mass, and Bazian CPs, respectively. The maximum values of about $222 \pm 20 \text{ Bq m}^{-3}$ and 1.402 mSv y^{-1} , respectively, in sector III (Grinding) at Bazian CP. The achieved results reveal that the maximum value of radon concentration in all sectors of the CPs is below the international standard value (300 Bq m^{-3}) of both the World Health Organization and International Commission on Radiological Protection.

Index Terms–Annual effective dose, cement plants, CR-39 detector, Radon concentration.

I. INTRODUCTION

Radon is an odorless noble natural radioactive gas directly produced by ^{226}Ra decay in the natural uranium series chain (^{238}U) which is distributed everywhere in the earth's crust. Its half-life (3.82 days) is long enough to permit the gas diffusion in the soil or groundwater and the successive transfer to the atmosphere or, through cracks or penetrations in the building foundations, into houses (Ciolini and Mazed, 2010). The level of radon in the air varies widely according to the geological nature of the ground, with low levels in areas of basalt and high levels in granite-rich areas (Bajwa

and Virk, 1997). Radon is a primary radiation source, in which exposure risk duplicates in public places, workplaces, closed area, and underground places. In recent years, there has been an increased awareness of the exposure of radon and thoron in workplaces other than mines (IAEA, 2011). Many workplaces are often located above the ground, such as offices, schools, old bazaar, and factories. Recently, the normal limit of indoor radon concentration determined by International Commission on Radiological Protection (ICRP) to be 200 Bq m^{-3} , and ICRP recommended the maximum level of indoor radon concentration of 300 Bq m^{-3} in dwelling and workplace (ICRP, 2012; Lecomte, et al., 2014). In addition, the World Health Organization proposed a reference level of 100 Bq m^{-3} to minimize the health hazards of indoor exposure due to ^{222}Rn . They stated that “if this level cannot be reached under the prevailing country-specific conditions, the chosen reference level should not be exceeded than 300 Bq m^{-3} ” (Kathleen, et al., 2009; Bochicchio, 2014).

^{222}Rn and ^{220}Rn get into the atmosphere mainly by crossing the ground-air or building material-air interfaces. Concentrations of ^{222}Rn and ^{220}Rn in soil and building materials are found to be up to $1\text{E}+04$ times higher than in the atmosphere (Gurau, et al., 2014). Previous studies reported that the risk of stomach cancer increased among the workers of some Korean cement industry due to the dust exposure (dust carried radon) (Koh, et al., 2013). The direct exposure of workers to cement dust in the construction industry and the cement manufacturing industry is expected. This is due to the inhalation of short-lived decay productions of ^{222}Rn and ^{220}Rn (thoron) from the atmosphere and their subsequent deposit along the walls of the various airways of the bronchial tree. Radon emanates by two ways; first come from the walls and ceiling and the other from the raw materials (UNSCEAR, 2000). Therefore, it is the role of researchers and associations of environmental radioactivity in all countries to provide sufficient information to the workers in cement plant (CP) and construction industry to reduce the risk of cancer. On the other hand, cement is a crucial, economical, and high-quality construction material used in construction projects worldwide. Knowledge about the physics and chemistry of cement products is important since they are directly related to the people's life. Portland cement is the most prevalent one among other types of cement. The natural radionuclide in raw and processed materials can vary considerably depending on their

ARO-The Scientific Journal of Koya University
Volume VI, No.1 (2018), Article ID: ARO.10329, 6 pages
DOI: 10.14500/aro.10329

Received 27 November 2017; Accepted: 12 January 2018

Regular research paper: Published 02 March 2018

Corresponding author's, e-mail: adel.hossien@univsul.edu.iq

Copyright © 2018 Adil M. Hussein, Kamal O. Abdullah,

Kharman A. Faraj, Dara F. Hamamin. This is an open access article distributed under the Creative Commons Attribution License.



geological source and geochemical characteristics (El-Taher, et al., 2010). The essential constituents of cements such as lime, silica, and alumina are derived from the earth's crust in which radioactive elements such as uranium and thorium are also present in varying amounts almost everywhere (Nain, 2006).

In this work, passive detection technique (CR-39 detector) was used for recording radon concentration. CR-39 detector offers several advantages over alternative charged particle detectors. It is resistant to electromagnetic radiation, especially X-rays. CR-39 detector is mainly used in the field of health physics (Jain, et al., 2013). Many studies have been performed on a local scale with passive detectors to determine the radon concentration value in homes and workplaces. According to Alsaedi, et al. (2013) recent study, the CR-39 detectors can be used successfully to measure the radon concentration in cement products of Iraq cement companies. They observed that the radon concentration values vary from 18 to 178 Bq m⁻³ and the highest radon exhalation rates were found in Bazian CP - Sulaymaniyah, Iraq. In general, raw materials used in Bazian and Tasluja regions for cement production are naturally more radioactive than other CPs. Moreover, a lot of information about the radioactivity of cement has been recorded in worldwide studies. The cement radioactivity in each sector of cement processing was studied by Turhan, 2008 in which he added one inorganic material such as blast furnace slag, natural pozzolanas (trass), silica fume, fly ash, burnt shale (schist), and limestone. The above fact encouraged us to assess the radon level in the mentioned CPs and to focus on the radon exposure to workers directly in each sector of cement processing. The main objective of the present work is to record the radon concentration in different sectors of CPs established in Sulaymaniyah city - Iraq, using the CR-39 technique. CP sectors are divided into two main categories, some of them are close storage and the other is open. Hence, the indoor and outdoor radiations were measured in the present work. The results of this work can identify the radon concentration level inhaled by workers in each operating sector of the CPs can be identified. In addition, the total effective dose was measured directly by a portable dosimeter (UltraRadic - Canberra, model - MRAD111), at least to determine the terrestrial radium concentration which acts as a main source (parent) of the measured radon.

II. MATERIALS AND METHODS

A. Studied area description

Experimental measurements were carried out in Tasluja, Mass, and Bazian CPs located 30–40 km west and south-west of Sulaymaniyah city. The area is characterized by the most suitable geological formation for cement production. Capacity of Tasluja, Mass, and Bazian CPs are about 2.3, 6.0, and 2.5 million t/annum, respectively. The CPs provide different types of cement (CEM I 42.5 R-OPC, high sulfate resistance-HSR, Al-Gesr, and CEM II/A-L 42.5 R) for many Iraqi and Kurdistan cities (Holcim, 2016; Mass Group Holding, 2016). In general, this area characterizes as a dense industrial zone. Each CP contains various sectors, CR-39 chambers were

hanged in open position of some of sectors but the other were hang in closed area such as (I) crusher is closed area, (II) proportioning equipment is closed area (correction storage for adding sand, iron, and gypsum), (III) grinding mill is closed area, (IV) preheater tower is open area, (V) clinker is open area, (VI) clinker cooler is open area, (VII) cement storage is closed area, and the last one is (VIII) background is open area as are shown in Fig. 1. Some of these sectors are big closed storage for raw and mixed material.

B. Experimental Method

In this work, the radon concentrations were measured in all sectors of the above mentioned CPs. For this purpose, the survey was performed from May to August 2016. Sufficient pieces of CR-39 (made by Track Analysis System Ltd., Bristol, United Kingdom) detectors are calibrated using standard alpha emitter source (²⁴¹Am). The detail of this procedure can be seen elsewhere (Abu-Jarad, 1988). The dimensions of CR-39 pieces were 1 × 1.5 cm² and placed in the upper part of a chamber. The alpha particles emitted in the radon decay inside the chamber leave tracks in the CR-39 detector. These dosimeter chambers were fixed at the height of 165 cm in each sector for the sake of simulating worker radon inhalation, especially at the location where workers have done their responsibility. A total of 24 dosimeters were suspended on the walls of each sector as shown in Fig. 2a and b.

After 90 days of exposure, the suspended dosimeters were collected and the track density recorded based on the method mentioned in Abdulla, 2013. The radon concentration is estimated from the following equation:

$$\rho = K \times C_a \times T, \quad (1)$$

where, ρ is track density (Tr/cm²), K is calibration factor, C_a is ²²²Rn concentration in airspace inside the dosimeter chamber which is measured by Bq m⁻³, and T offers exposure time which that is 90 days in the present work. The K value is calculated for the cylindrical chamber as shown in Fig. 2,

its value equal to 0.0582, $\frac{\text{Tr cm}^{-2} \text{ hr}^{-1}}{\text{Bq m}^{-3}}$ which based on the

method mentioned in Abdulla, 2013; Barillon, et al., 1993.

The ²²²Rn emanate from the raw materials and its dose exposed to the workers in each sector of the CPs. The famous criteria for measuring radon risk are an annual effective dose (E in mSv y⁻¹) due to the inhalation of the decay products of ²²²Rn as reported in UNSCEAR, 2000, which is given by:

$$E = C_a \times F \times H \times T \times D \quad (2)$$

Where, C_a is the ²²²Rn concentration in Bq m⁻³, F is indoor an equilibrium factor (0.4) and outdoor one is (0.6), H is the outdoor occupancy factor (0.2), T is hours of working in a year (8766 hr y⁻¹), and D is the dose conversion factor (9.0 * 10⁻⁶ mSv hr⁻¹/Bq m⁻³) (Al-Saleh, 2007; UNSCEAR, 2000). Furthermore, one can calculate the radon dose of lung and soft tissue as reported in ICRP-1993 (Protection, 1993).

III. RESULTS AND DISCUSSIONS

In this work, the radon concentration (C_a) in Tasluja, Mass, and Bazian CPs was recorded by CR-39 detector. It is clear

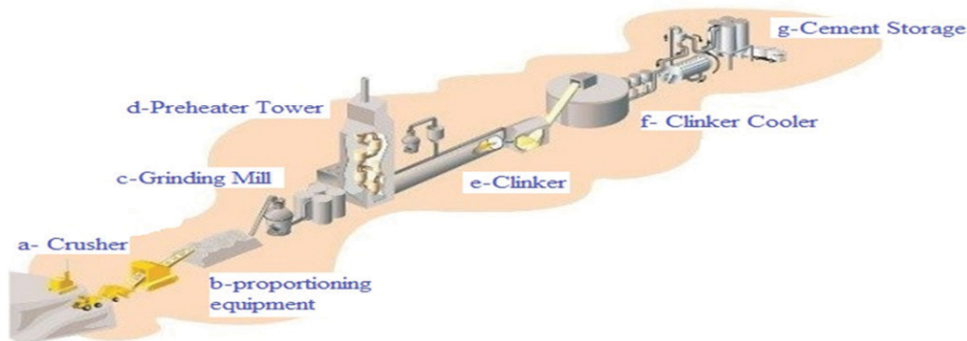


Fig. 1. Diagram of cement plant sectors of Lafarge association that established and reconstructed Bazian and Tasluja cement plants (CPs). The mass CP design is near to the other two plants (Holcim, 2016).

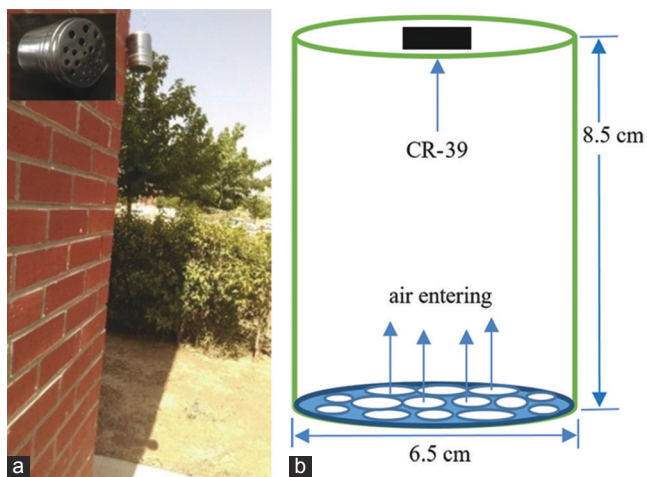


Fig. 2. Pinholes dosimeter containing CR-39 detector; (a) Dosimeter *in situ* (background) location and (b) diagram of the dosimeter.

from Table 1 that the AM values of C_a are 98, 101, and 125 $Bq\ m^{-3}$, for Tasluja, Mass, and Bazian CPs, respectively. Fig. 3 presents the frequency distribution of the radon concentration ($Bq\ m^{-3}$) in all sectors of the three CPs. Almost all the sectors aggregate in the range of the full width half maximum range, except of sector III of Bazian CP which deviates from the other. Most of the radon concentrations presented in Fig. 3 lay between 80 and 130 $Bq\ m^{-3}$. The details of the results are presented in Table 1. The AM value of radon concentration in Bazian CP is 125 $Bq\ m^{-3}$ which is the highest radon concentration values recorded in all Iraqi CPs (Alsaedi, 2013). The high value of track density in cement of the Bazian CP is an evidence for the existence of high radon concentration compared to Mass and Tasluja CPs. The maximum value (222 $Bq\ m^{-3}$) of radon concentration was recorded in sector III of Bazian CP compare to the other sectors as shown in Fig. 4. This is related to the fact that the radon emanated from the soil and limestone slit come from the quarry (the mountain that is surrounding the CPs) to the crusher (first sector) and then transferred from one sector to another.

Many of CPs in Sulaymaniyah city were built near to the mountains; thus, a high radionuclides background is expected. Another main factor is the variation in soil used by CPs.

Bazian and Tasluja CPs depend on the soil quarry located in the western field side of the Bazian plant. The soil is derived from weathered part of Gercus and Pilaspi formations from the adjacent surrounded high elevated area. Whereas, the Mass CP depends on the Fatha “Lower Fars” formation where the depositional environment is totally different and its enriched with sulfate mineral (Lawa, 2004). These results suggest that the CPs need to be established far away from the mountains. Obviously, this will be more cost-effective, but it will provide a healthier environment for the workers. It is clear from Table 1 that only two sectors (II and III) of Tasluja CP have radon concentrations above 100 $Bq\ m^{-3}$. Regarding the Mass CP, the high radon concentration (above 100 $Bq\ m^{-3}$) can be noted in sectors III and V. Unfortunately, five sectors of Bazian CP exhibit the existence of high radon concentration.

Another important radiological parameter is the radon annual effective dose E ($mSv\ y^{-1}$). It was calculated from Eq. 2 and tabulated in Table 1. The AM values of E ($mSv\ y^{-1}$) in all sectors of the CPs were less than the worldwide value 1.15 $mSv\ y^{-1}$ as reported by UNSCEAR-2008 (UNSCEAR, 2008), except the sector III and IV of Bazian CP. The maximum values of E ($mSv\ y^{-1}$) were recorded by the sector III in each mentioned CPs.

Furthermore, the total effective dose was measured directly to enhance the passive radon measuring by CR-39. The direct total effective dose recorded in each sector of the three CPs using the UltraRadiac dosimeter with efficiency 30%. Table 2 summarizes that the total effective dose rate ranged from 0.138 to 0.229 $mSv\ hr^{-1}$ of Tasluja CP, in Mass CP ranged from 0.100 to 0.217 $mSv\ hr^{-1}$, and in Bazian CP ranged from 0.165 to 0.67 $mSv\ hr^{-1}$.

From Table II, it can be seen that the anomalies of total effective dose recorded in sector II of Bazian CP (correction storage for adding sand, iron, and gypsum) were 0.670 $mSv\ hr^{-1}$, which is 4 times larger than the other sectors. This can be attributed to the addition of iron and gypsum to the crushing raw materials.

In Table II and Fig. 5, it can be observed that the correlation between radon and total effective dose is low and it is about 0.085 plus a constant which is about 0.157. These factors are specified by this radon survey. The constant refers to the participation of other gamma

TABLE I
TRACK DENSITY, RADON CONCENTRATIONS (CA), AND ANNUAL EFFECTIVE DOSE (E) FOR DIFFERENT SECTORS OF TASLUJA, MASS, AND BAZIAN CPs

Sectors	Tasluja CP			Mass CP			Bazian CP		
	Track density	C _a (Bq m ⁻³)	E (mSv y ⁻¹)	Track density	C _a (Bq m ⁻³)	E (mSv y ⁻¹)	Track density	C _a (Bq m ⁻³)	E (mSv y ⁻¹)
I	471.6	89±9	0.568	503.04	95±9	0.606	679.10	129±11	0.818
II	538.97	102±10	0.649	503.04	95±9	0.606	729.40	139±12	0.878
III	660.24	125±12	0.795	848.88	161±15	1.022	1164.4	222±20	1.402
IV	503.04	95±9	0.909	519.44	99±9	0.938	723.12	137±12	1.306
V	471.6	89±9	0.852	538.97	102±10	0.973	603.51	115±10	1.090
VI	471.6	89±9	0.852	440.16	83±8	0.795	440.16	83±7	0.795
VII	503.04	95±9	0.606	419.16	79±7	0.505	411.97	78±7	0.496
VIII	503.04	95±9	0.909	465.97	88±6	0.580	503.04	95±8	0.909
AM±ε		98±9	0.767		101±10	0.753		125±10	0.962
Max.		125±12	0.909		161±15	1.022		222±20	1.402
Min.		89±9	0.568		79±7	0.505		78±7	0.496

CP: Cement plant

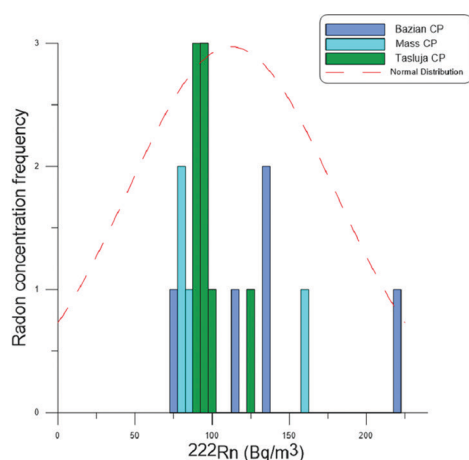


Fig. 3. Frequency distribution of the radon concentration in Bq m⁻³ for all sectors of the three cement plants

sources such as natural radionuclide ⁴⁰K and some isotopes out of natural series (²³⁸U and ²³²Th); Al, Fe, Mn, Cd, Co, Cr, Cu, Ni, Pb, V, and Zn (Al-Dadi, et al., 2014) due to the material mixing in sectors II, III, IV, and V. The unexpected result in this study is that the radon concentration value of the sector VIII (manager office) was close to the mean value in each cement factory, the researcher regarded the sector VIII as background level for all other sectors which recorded in Table II. Moreover, it is far 200 m from the other sectors.

IV. CONCLUSIONS

The concentrations of radon in various sectors of Tasluja, Mass, and Bazian Cps have been measured directly; using a CR-39 detector and the radon annual effective doses E (mSv y⁻¹) have been calculated. In this work, the measured radon concentration and its annual effective dose E in all sectors of Bazian CP were significantly higher than Mass and Tasluja Cps. These high recorded values in some sectors of the Bazian CP can be hazardous and increase the risk of cancer in the future. The finding of this study

indicates that the highest value of radon concentration and annual effective dose E was recorded in grinding mill sectors (III). This can be ascribed to the radon emanation and the natural radionuclides emission ratio as a result of material mixing and resizing process. The data obtained show that the radon concentration is high in the closed sectors such as crusher sector I, proportioning equipment sector II, and the grind mill sector III in all plants compared to open sectors. Our suggestion is that workers in the grinding mill sector must have more permission hours compared to the other sectors. In addition, the ventilation process must be improved in the entire closed sector for all Cps.

A novel finding of the present study was that radon concentration level of manager office was found to be dependent on radon concentration mean value of all other sectors of the CP. Many European and North American countries established the radon reduction program. This program should include radon reduction, especially from the plants that have fly ash and dust such as CP. It is crucial to keep the work environment safe for the workers. Therefore, all sectors in Cps should installed radon monitoring system to detect the limit of radon concentration. Moreover, the anomalies of total effective dose recorded in sector II of Bazian CP make the researchers pay attention to assess the total dose in storage sectors of the Cps in the future work. In general, the researchers suggest that the quality control agency elsewhere should focus on the materials storage. Total effective dose correlates weakly with radon one linearly plus a constant. The constant could be useful in the interpretation of future radon surveys in the Bazian area.

V. ACKNOWLEDGMENT

The researchers gratefully acknowledge the University of Sulaimani - Ministry of Higher Education and Scientific Research, for their financial support. The authors like to thank the management staff's and workers in the Tasluja, Bazian, and Mass plants for their help and response.

TABLE II
TOTAL AND RADON EFFECTIVE DOSE RATE (mSv hr⁻¹) IN THE TASLUJA, MASS, AND BAZIAN CPs SECTORS

Sectors	Tasluja CP		Mass CP		Bazian CP	
	Total effective dose	Radon effective dose	Total effective dose	Radon effective dose	Total effective dose	Radon effective dose
I	0.153	0.324	0.137	0.346	0.210	0.466
II	0.172	0.370	0.162	0.346	0.670	0.501
III	0.143	0.453	0.185	0.583	0.200	0.800
IV	0.172	0.518	0.171	0.535	0.195	0.745
V	0.138	0.486	0.182	0.555	0.181	0.622
VI	0.229	0.486	0.182	0.453	0.165	0.453
VII	0.228	0.346	0.100	0.288	0.210	0.283
VIII	0.150	0.518	0.217	0.331	0.180	0.518
AM	0.173	0.438	0.167	0.430	0.251	0.549
Max	0.229	0.518	0.217	0.583	0.670	0.800
Min	0.138	0.324	0.100	0.288	0.165	0.283

CP: Cement plant

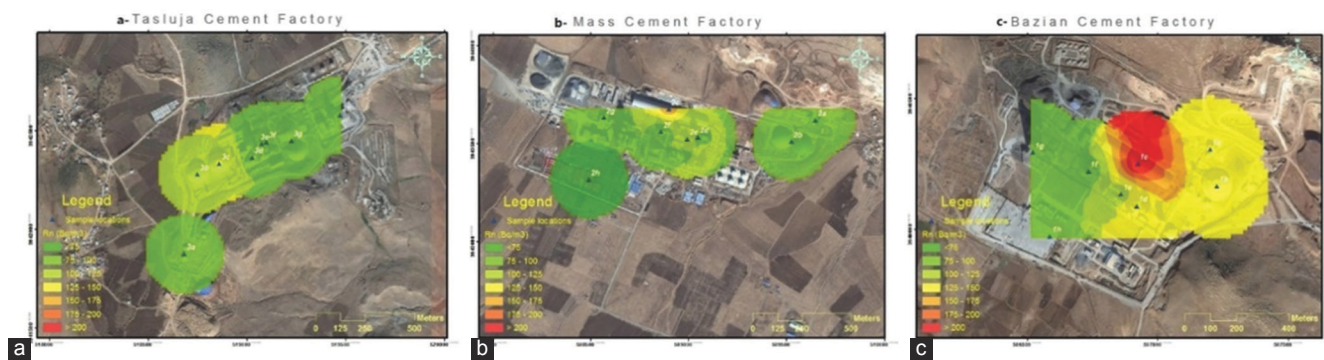


Fig. 4. (a-c) Landscape map of the investigated area to define radon concentration level of the sectors. (a) Tasluja cement plant (CP), (b) Mass CP, (c) Bazian CP.

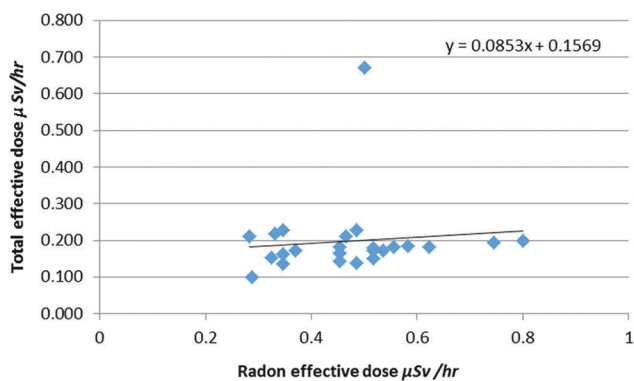


Fig. 5. Total and radon effective dose rate (mSv hr⁻¹) relation in all sectors of the Tasluja, Mass, and Bazian cement plants.

REFERENCES

Abdulla, K.O., 2013. *Natural Radioactivity Measurements of soil and water in Sulaimani Governorate*. PhD. University of Sulaimani, Iraq.

Abu-Jarad, F.A., 1988. Application of nuclear track detectors for radon related measurements. *International Journal of Radiation Applications and Instrumentation. Part, 15*(1-4), pp.525-534.

Al-Dadi, M.M., Hassan, H.E., Sharshar, T., Arida, H.A. and Badran, H.M., 2014. Environmental impact of some cement manufacturing plants in Saudi Arabia. *Journal of Radioanalysis and Nuclear Chemistry, 302*(3), pp.1103-1117.

Alsaedi, A.K., Almayahi, B.A. and Alasadi, A.H., 2013. Cement 222Rn and 226Ra concentration measurements in selected samples from different companies. *Asian Journal of Natural and Applied Sciences, 2*(4), pp.95-100.

Al-Saleh, F.S., 2007. Measurements of indoor total radiation and radon concentrations in dwellings of Riyadh city, Saudi Arabia. *Applied Radiation and Isotopes, 65*(7), pp 843 -848.

Bajwa, B. and Virk, H., 1997. Environmental radon monitoring in dwellings near the radioactive sites. Amritsar-143005, India. *Radiation Measurement, 26*(1), pp 457-460.

Barillon, R., Klein, D., Chambaudet, A. and Devillard, C., 1993. Comparison of the effectiveness of three radon detectors (LR115, CR-39 and Silicon diode pin) placed in cylindrical device-theory and experimental techniques. *Nuclear Tracks and Radiation Measurements, 22*(1-4), pp.281-282.

Bohicchio, F., 2014. Protection from radon exposure at home and at work in the directive 2013/59/Euratom. *Radiation Protection Dosimetry, 160*, pp.1-6.

Ciolini, R. and Mazed, D., 2010. Indoor radon concentration in geothermal areas of central Italy. *Journal of Environmental Radioactivity, 101*(9), pp.712-716.

El-Taher, A., Makhluif, S., Nossair, A. and Halim, A.A., 2010. Assessment of natural radioactivity levels and radiation hazards due to cement industry. *Applied Radiation and Isotopes, 68*(1), pp.169-174.

Gurau, D., Stanga, D. and Dragusin, M., 2014. Review of the principal mechanism of radon in the environment. *Romanian Journal of Physics, 59*(9-10), pp.904-911.

Holcim, L., 2016. *Sulaymaniyah Governorate, Iraq*. Available from: https://www.lafarge-iraq.com/en/4_2_1-BAZIAN_Cement_Plant

- International Atomic Energy Agency (IAEA), 2011. *Radiation Protection and Safety of Radiation Sources: International Basic Safety Standards*. Interim Edition. IAEA, Vienna.
- International Commission on Radiological Protection (ICRP), 2012 *Proceedings of the First ICRP Symposium on the International System of Radiological Protection*. Vol. 41(3-4), Annals of ICRP, Maryland.
- Jain, R.K., Kumar, A., Chakra borty, R.N. and Nayak, B.K., 2013. The response of CR-39 plastic track detector to fission fragments at different environmental (temperature) conditions. *In Proceedings of the DAE-BRNS Symposium on Nuclear Physics*, 58, p.564. Available from: <http://inspirehep.net/record/1506787/files/B128.pdf>
- Kathleen, W., Miller, J., Michael, A.C., 2009. Radon and You: Promoting Public Awareness of Radon in Montana's Air and Ground. Montana Bureau of Mines and Geology. *Handbook on Indoor Radon: A Public Health Perspective*. World Health Organization, Geneva.
- Koh, D.H., Kim, T.W., Jang, S. and Ryu, H.W., 2013. Dust exposure and the risk of cancer in cement industry workers in Korea. *American Journal of Industrial Medicine*, 56, pp.276-281.
- Lawa, F.A., 2004. *Sequence stratigraphic analysis of the Middle Paleocene-Middle Eocene in the Sulaimani district (Kurdistan region)*. PhD Thesis. University of Sulaimani, Iraq.
- Lecomte, J.F., Solomon, S., Takala, J., Jung, T., Strand, P., Murith, C., Kiselev, S., Zhuo, W., Shannoun, F. and Janssens, A., 2014. *ICRP Publication 126: Radiological protection against radon exposure*. Annals of the ICRP.
- Mass Group Holding, 2016. Sulaymaniyah Governorate, Iraq. Available from: http://www.massgroupholding.com/Newsdetail-unit_2.aspx?jimare=19&title=%D9%85%D8%B5%D9%86%D8%B9%20%D8%A7%D8%B3%D9%85%D9%86%D8%AA%20%D9%85%D8%A7%D8%B3-%20%D8%A8%D8%A7%D8%B2%D9%8A%D8%A7%D9%86&cor=3
- Nain, M., Chauhan, R.P. and Chakarvarti, S.K., 2006. Alpha radioactivity in Indian cement samples. *Iranian Journal of Radiation Research*, 3(4), pp.171-176.
- Protection, R., 1993. *International commission on Radiological Protection (ICRP) Publication 65. Protection Against Radon 222 at Home and at Work*. Ann. ICRP, p.23 (2).
- Turhan, S., 2008. Assessment of the natural radioactivity and radiological hazards in Turkish cement and its raw materials. *Journal of Environmental Radioactivity*, 99, pp.404-414.
- United Nations Scientific Committee on the Effects of Atomic Radiation (UNSCEAR), 2000. *Effects of Ionizing Radiation: 2000 Report to the General Assembly*, with Scientific Annexes B, Vol. 2. United Nations, New York.
- United Nations Scientific Committee on the Effects of Atomic Radiation, 2015. *UNSCEAR 2008 report to the general assembly with scientific annexes*. United Nations, New York.
- United Nations Scientific Committee on the Effects of Atomic Radiation (UNSCEAR), 2008. *Effects of Ionizing Radiation: 2010 Report to the General Assembly*, with Scientific Annexes, Vol. 1. United Nations, New York.

The Use of Quadtree Range Domain Partitioning with Fast Double Moment Descriptors to Enhance FIC of Colored Image

Bushra A. Sultan¹, Loay E. George², Nidaa F. Hassan³

¹Department of Computer Science, College of Science, University of Baghdad, Baghdad - Iraq

²Department of Remote Sensing, College of Science, University of Baghdad, Baghdad - Iraq

³Department of Computer Science, University of Technology, Baghdad - Iraq

Abstract—In this paper, an enhanced fractal image compression system (FIC) is proposed; it is based on using both symmetry prediction and blocks indexing to speed up the blocks matching process. The proposed FIC uses quad tree as variable range block partitioning mechanism. two criteria's for guiding the partitioning decision are used: The first one uses sobel-based edge magnitude, whereas the second uses the contrast of block. A new set of moment descriptors are introduced, they differ from the previously used descriptors by their ability to emphasize the weights of different parts of each block. The effectiveness of all possible combinations of double moments descriptors has been investigated. Furthermore, a fast computation mechanism is introduced to compute the moments attended to improve the overall computation cost. the results of applied tests on the system for the cases “variable and fixed range” block partitioning mechanism indicated that the variable partitioning scheme can produce better results than fixed partitioning one (that is, 4×4 block) in term of compression ratio, faster than and PSNR does not significantly decreased.

Index Terms—Fractal image compression, Iterated function system, Moments features, Quadtree.

I. INTRODUCTION

Recently, fractal compression of digital images has attracted much attention. Fractal image compression (FIC) is based on the theory of iterated function system (IFS), and its performance relies on the presence of self-similarity degree (Mahadevaswamy, 2000). FIC process implies finding a set of transformations that produce fractal image which approximates the original image (Xi and Zhang, 2007). One of the most important characteristics of fractal image coding is its unsymmetrical property of encoding and decoding

processing. Coding time is rather long for whole domain-range matching operation, whereas the decoding algorithm is relatively simple and fast. This weak aspect makes the fractal compression method not widely used as standard compression. FIC has the advantages of fast decompression as well as very high compression ratios (CR) (Al-Hilo and George, 2008).

Many attempts have been done for speeding FIC using different speeding-up methods. An adaptive zero-mean method was proposed by (George, 2006), according to this method the average of the range block is used instead of traditional offset parameter. George method's used in combination with moment-based features (George and Al-Hilo, 2008; Al-Hilo and George, 2008) and DCT-based methods (George and Minas, 2011) as IFS transform invariants to be used as block descriptors; which in turn is utilized to classify the domain and range blocks. Furthermore, by adding the symmetry predictor that introduced in the method given in (George and Al-Hilo, 2011) that based on using first-order centralized moments; this predictor is useful to reduce the number of isometric trails from (8, that is, Rotation, reflection...etc..) trials to (1) trail. Mahmoud, 2012 proposed the use of double moment descriptors to speed up FIC.

In the proposed method, introduced in this paper, the loaded RGB color image was transformed to YUV color space, where Y is the luminance component, and U, V are the chromatic components. To get an effective compression, the U, V component are downsampled (Ning, 2007). Then, each component of YUV is coded individually using FIC method. An improved algorithm of FIC based on partition IFS method is applied; the improvement was in: (i) The scheme of range pool partitioning, (ii) IFS matching with low computation redundancy, and (iii) using a new set of centralized moments which are complementary and more informative.

The rest of the paper is structured as follows: Section II is dedicated to give an overview for the concepts and methods used to explain the enhance FIC system. The results of the tests applied the enhanced are discussed in Section III, and finally, the derived conclusions are listed in Section IV.

ARO-The Scientific Journal of Koya University
Volume VI, No.1 (2018), Article ID: ARO.10207, 10 pages
DOI: 10.14500/aro.10207

Received 24 February 2017; Accepted: 24 February 2018
Regular research paper; Published 24 March 2018

Corresponding author's, e-mail: bushraasultan@scbaghdad.edu.iq
Copyright © 2018 Bushra A. Sultan, Loay E. George, Nidaa F. Hassan.
This is an open-access article distributed under the Creative Commons Attribution License.



II. MATERIALS AND METHODS

A. IFS Coding for Zero-mean Blocks

IFS coding based on zero-mean blocks matching implies that the offset values of the block replacement with average brightness values. Hence, the IFS mapping equation was performed according to this change. For a range block with pixel values (r_0, \dots, r_{n-1}) and a domain block with pixels (d_0, \dots, d_{n-1}) the contractive affine approximation is (George, 2006):

$$r_i = s(d_i - \bar{d}) + \bar{r} \quad (1)$$

$$\bar{r} = \frac{1}{n} \sum_{i=0}^{n-1} r_i \quad (2)$$

$$\bar{d} = \frac{1}{n} \sum_{i=0}^{n-1} d_i \quad (3)$$

Where r_i is the optimal approximated value of the i^{th} byte value of the range block; d_i is the corresponding byte value in the best-matched domain block; s is the scaling coefficient; \bar{d}, \bar{r} are the average of domain and range block, respectively.

To determine the scale (s) value, the method of least mean square errors (depicted in equation 1) is applied to get:

$$s = \begin{cases} \frac{\frac{1}{n} \sum_{i=0}^{n-1} d_i r_i - \bar{r} \bar{d}}{\sigma_d^2} & \text{if } \sigma_d^2 > 0 \\ 0 & \text{if } \sigma_d^2 = 0 \end{cases} \quad (4)$$

$$X^2 = \sigma_r^2 + s \left[s \sigma_d^2 + 2\bar{d}\bar{r} - \frac{2}{n} \sum_{i=0}^{n-1} d_i r_i \right] \quad (5)$$

Where,

$$\sigma_d^2 = \frac{1}{n} \sum_{i=0}^{n-1} d_i^2 - \bar{d}^2 \quad (6)$$

$$\sigma_r^2 = \frac{1}{n} \sum_{i=0}^{n-1} r_i^2 - \bar{r}^2 \quad (7)$$

At each range-domain matching instance, and before determination of χ^2 (equation 5), the scale coefficient (s) must be bounded to be in the range $[-s_{\max}, s_{\max}]$. Then, the scale coefficient (s) and \bar{r} should be quantized using the following equations (Mahmoud, 2012):

$$\tilde{s} = Q_s I_s \quad (8)$$

$$I_s = \text{round} \left(\frac{s}{Q_s} \right) \quad (9)$$

$$\tilde{r} = Q_r I_r \quad (10)$$

$$I_r = \text{round} \left(\frac{\tilde{r}}{Q_r} \right) \quad (11)$$

Where

$$Q_s = \frac{s_{\max}}{2^{bs-1} - 1} \quad (12)$$

$$Q_r = \frac{255}{2^{br} - 1} \quad (13)$$

Where s_{\max} is the highest permissible value of the scale coefficient (s); Q_s and Q_r are the quantization steps of the scale and \bar{r} coefficients, respectively; bs is the number of scale bits; br is the number of range mean bits.

B. Isometric Process Predictor

The eight isometric mappings are shown in Table I (George and Al-Hilo, 2009). A full search through the set of 8 isometric states of each block is prohibitive due to the large number of calculation involved. The goal is to exclude isometric states of blocks that have no chance of being selected as the best choice (George and Mahmoud, 2011).

The involved calculation for block indexing and transform prediction should be simpler than the full calculation. This would ease the burden of searching by reducing the set of possible candidates to minimal error. Hence, in this process, the speeding up of FIC is accomplished using the first-order moments descriptor (George and Al-Hilo, 2009). The theoretical basis of this predictor of the isometric processes is described in the following sections.

Centralized moments

For an image block $I(x,y)\{x,y\} \{0,1,\dots,L-1\}$, its first-order centralized moments are defined as (George and Mahmoud, 2011):

$$M_x = \sum_{x=0}^{L-1} \sum_{y=0}^{L-1} I(x,y)(x-c) \quad (14)$$

$$M_y = \sum_{y=0}^{L-1} \sum_{x=0}^{L-1} I(x,y)(y-c) \quad (15)$$

Where $c = (L-1)/2$.

Combining equations (14) and (15) with the equations listed in Table I, the relationship between the new moments values (M'_x, M'_y) of a transformed block with its old moments' values (M_x, M_y), before transformation, could be determined; Table II shows these relationships (George and Al-Hilo, 2009).

Blocks classification

A method for blocks classification based on moment criteria is suggested. The classification is based on the status of its first-order moments values (that is, M_x and M_y). The following three status criteria have been used where:

- Condition-1: Is $|M_x| \geq |M_y|$ or not?
- Condition-2: Is $M_x \geq 0$ or not?
- Condition-3: Is $M_y \geq 0$ or not?

The use of these three Boolean criteria leads to eight block classes as illustrated in Table III (George and Al-Hilo, 2001).

At each range-domain matching instance, the indices of both domain and range blocks are passed through the predictor, as shown in Table IV. Then, the predictor outputs the index of the required isometric transform to get the best possible match between the domain and range blocks (George and Mahmoud, 2011).

C. Moment's Ratio and Index

Moment's ratio can be calculated using the following equation by (Mahmoud, 2012):

$$Ratio_M = \begin{cases} \left\lfloor \frac{M_y}{M_x} \right\rfloor \times Nm & \text{if } M_x \geq M_y \\ \left\lfloor \frac{M_x}{M_y} \right\rfloor \times Nm & \text{if } M_y \geq M_x \end{cases} \quad (16)$$

Where M_x and M_y are the moments around x and y coordinates, respectively. Nm is the maximum moment ratio value. Al-Hilo and George, 2008 concluded that "If the two blocks (range and domain) nearly satisfy the conductive affine transform, then their moment ratio factor ($Ratio_{Mr}$

and $Ratio_{Mg}$) should have similar values, this does not mean that any two blocks have similar ($Ratio_M$) factor should necessarily satisfy the affine transform."

The value of combined moment ratio index is computed as the linear combination of two descriptors ($Ratio_{M1}$) and ($Ratio_{M2}$) using the following equation (Mahmoud, 2012).

$$I_M = [Ratio_{M1} \times (Nm+1) + Ratio_{M2}] \quad (17)$$

The index (I_M) is used to classify the domain and range blocks (that is, each class includes blocks having the same index). This factor is used to improve (that is, speeding up) the range-domain search task by only the domain blocks whose I_M values are similar (or near) to that of tested range block are IFS-matched.

D. The Proposed FIC

The aims of the enhanced FIC are:

- A new set of moment descriptors are introduced, they differ from the previously used ones by their excellent emphasis to reflect the moments' weight of certain part of the block. In this article, the effectiveness of all possible combinations of double moment descriptors had been investigated.
- Quadtree (QT) is used to enhance IFS performance. It is used as variable range blocks partitioning scheme instead of fixed block partitioning scheme. The criteria guiding the decomposition

TABLE I
ISOMETRIC TRANSFORMATION (GEORGE AND AL-HILO, 2009).

ID	Operation	Equation	Results
0	Identity	$x' = x \cos(0) - y \sin(0)$ $y' = -x \sin(0) + y \cos(0)$	$x' = x$ $y' = y$
1	Rotation (+90)	$x' = x \cos(90) - y \sin(90)$ $y' = -x \sin(90) + y \cos(90)$	$x' = y$ $y' = -x$
2	Rotation (+180)	$x' = x \cos(180) - y \sin(180)$ $y' = -x \sin(180) + y \cos(180)$	$x' = -x$ $y' = -y$
3	Rotation (+270)	$x' = x \cos(270) - y \sin(270)$ $y' = -x \sin(270) + y \cos(270)$	$x' = -y$ $y' = x$
4	Reflection around X-axis	$x' = -x \cos(0) - y \sin(0)$ $y' = -x \sin(0) + y \cos(0)$	$x' = -x$ $y' = y$
5	Reflection around X-axis+Rotation(+90)	$x' = -x \cos(90) - y \sin(90)$ $y' = -x \sin(90) + y \cos(90)$	$x' = -y$ $y' = -x$
6	Reflection around X-axis+Rotation(+180)	$x' = -x \cos(180) - y \sin(180)$ $y' = -x \sin(180) + y \cos(180)$	$x' = x$ $y' = -y$
7	Reflection around X-axis+Rotation(+270)	$x' = -x \cos(270) - y \sin(270)$ $y' = -x \sin(270) + y \cos(270)$	$x' = y$ $y' = x$

TABLE II
THE RELATIONSHIP BETWEEN MOMENTS BEFORE AND AFTER APPLYING THE ISOMETRIC TRANSFORMATION (GEORGE AND AL-HILO, 2009)

ID	Operation	Relationship
0	Identity	$M'_x = M_x, M'_y = M_y$
1	Rotation (+90)	$M'_x = M_y, M'_y = -M_x$
2	Rotation (+180)	$M'_x = -M_x, M'_y = -M_y$
3	Rotation (+270)	$M'_x = -M_y, M'_y = M_x$
4	Reflection at X-axis	$M'_x = -M_x, M'_y = M_y$
5	Reflection around X-axis+rotation (+90°)	$M'_x = -M_y, M'_y = -M_x$
6	Reflection around X-axis+rotation (+180°)	$M'_x = M_x, M'_y = -M_y$
7	Reflection around X-axis+rotation (+270°)	$M'_x = M_y, M'_y = M_x$

TABLE III
THE TRUTH TABLE FOR EIGHT BLOCK CLASSES (MAHMOUD, 2012)

Block class ID	Boolean criteria		
	$ M_x \geq M_y $	$M_x \geq 0$	$M_y \geq 0$
0	T	T	T
1	T	T	F
2	T	F	T
3	T	F	F
4	F	T	T
5	F	T	F
6	F	F	T
7	F	F	F

0 - Identity, 1 - Rotation (+90), 2 - Rotation (+180), 3 - Rotation (+270), 4 - Reflection, 5 - Reflection+rotation (+90), 6 - Reflection+Rotation (+180), 7 - Reflection+Rotation (+270).

TABLE IV
THE REQUIRED ISOMETRIC OPERATION TO CONVERT THE BLOCK STATE (GEORGE AND MAHMOUD, 2011)

Range blocks ID	Domain blocks ID							
	0	1	2	3	4	5	6	7
0	0	6	4	2	7	3	1	5
1	6	0	2	4	1	5	7	3
2	4	2	0	6	3	7	5	1
3	2	4	6	0	5	1	3	7
4	7	3	1	5	0	6	4	2
5	1	5	7	3	6	0	2	4
6	3	7	5	1	4	2	0	6
7	5	1	3	7	2	4	6	0

0 - Identity, 1 - Rotation (+90), 2 - Rotation (+180), 3 - Rotation (+270), 4 - Reflection, 5 - Reflection+Rotation (+90), 6 - Reflection+Rotation (+180), 7 - Reflection+Rotation (+270).

process is the information richness of the region; it was used to decide the initial partitioning of the range blocks.

- FIC algorithm is reconfigured including the moment equations to remove any redundancy in the computation.

In the following subsection, the proposed enhanced FIC is explained in more details.

The proposed moments and the speeding up mechanism

A new set of weights is introduced and adopted to produce the new sets of moments, they are as follows:

$$W_1(i) = \begin{cases} \frac{2}{L} \left(i - \frac{L}{2} \right) & \text{for } i = \left[0, \frac{L}{2} \right) \\ -W_1(L-1-i) & \text{for } i = \left[\frac{L}{2} - 1, L \right) \end{cases} \quad (18-a)$$

$$W_1^{int}(i) = W_1(i) \times 100 \quad \text{for } i = [0, L) \quad (18-b)$$

$$W_2(i) = \begin{cases} \frac{2}{L} \left(i - \frac{1}{2} \right) & \text{for } i = \left[0, \frac{L}{2} \right) \\ -W_2(L-1-i) & \text{for } i = \left[\frac{L}{2} - 1, L \right) \end{cases} \quad (19-a)$$

$$W_2^{int}(i) = W_2(i) \times 100 \quad \text{for } i = [0, L) \quad (19-b)$$

$$W_3(i) = \begin{cases} \sin\left(\frac{\pi i}{L-1}\right) & \text{for } i = \left[0, \frac{L}{2} \right) \\ -W_3(L-1-i) & \text{for } i = \left[\frac{L}{2} - 1, L \right) \end{cases} \quad (20-a)$$

$$W_3^{int}(i) = W_3(i) \times 100 \quad \text{for } i = [0, L) \quad (20-b)$$

Fig. 1 presents the proposed three weight functions that assigned to each row or column within the block, when its length is equal to 8.

The new sets of moments around x-axis and around y-axis that using the weights functions given in equations (18-20) are defined as:

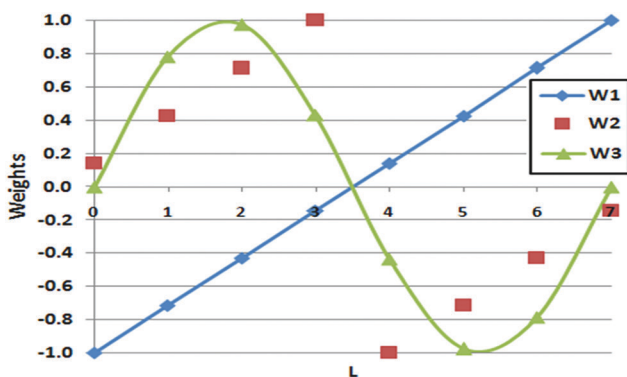


Fig. 1. The proposed weights.

$$Mx_1(x, y) = \sum_{r=x}^{r+L-1} \sum_{c=y}^{c+L-1} f(r, c) W_1^{int}(r-x) \quad (21-a)$$

$$My_1(x, y) = \sum_{c=y}^{c+L-1} \sum_{r=x}^{r+L-1} f(r, c) W_1^{int}(c-y) \quad (21-b)$$

$$Mx_2(x, y) = \sum_{r=x}^{r+L-1} \sum_{c=y}^{c+L-1} f(r, c) W_2^{int}(r-x) \quad (22-a)$$

$$My_2(x, y) = \sum_{c=y}^{c+L-1} \sum_{r=x}^{r+L-1} f(r, c) W_2^{int}(c-y) \quad (22-b)$$

$$Mx_3(x, y) = \sum_{r=x}^{r+L-1} \sum_{c=y}^{c+L-1} f(r, c) W_3^{int}(r-x) \quad (23-a)$$

$$My_3(x, y) = \sum_{c=y}^{c+L-1} \sum_{r=x}^{r+L-1} f(r, c) W_3^{int}(c-y) \quad (23-b)$$

Where L represents the length of the block; (x, y) are coordinates of the block relative to left-top corner; $F()$ is the 2D image array; W^{int} represents the integer index of the weights; Mx represents the low-order moments relative to x-axis; My represents the low-order moments relative to y-axis.

So, for each block, of the overlapped blocks listed in the domain pool, the moments (given by equations 21-23) have been computed. For fast computations of the moment descriptor equations the following scenario adopted to avoid the redundant summation occurs within each one by creating two 2D arrays, named “SumX” and “SumY,” such that:

$$SumX(x, 0) = \sum_{y=0}^{L-1} f(x, y) \quad (24)$$

$$SumX(x, y) = SumX(x, y-1) - f(x, y-1) + f(x, y+L-1) \quad (25)$$

$$SumY(0, y) = \sum_{x=0}^{L-1} f(x, y) \quad (26)$$

$$SumY(x, y) = Sumy(x-1, y) - YB(x-1, y) + YB(x+L-1, y) \quad (27)$$

Fig. 2 shows simple example of how the value of $SumX(0,0)$ and $SumX(0,1)$ had been computed for row sample when block length (L) equal to 8.

Now, the created arrays $SumX$ and $SumY$ can be used in (21-23) to become as:

$$Mx_1(x, y) = \sum_{r=x}^{r+L-1} SumX(r, y) \times W_1^{int}(r-x) \quad (28a)$$

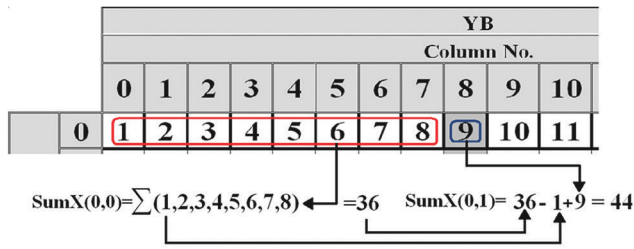


Fig. 2. Shows simple example of how the value of $SumX(0,0)$ and $SumX(0,1)$ had been computed for row sample when block length (L) equal to 8.

$$My_1(x, y) = \sum_{c=y}^{y+L-1} SumY(x, c) \times W_1^{int}(c-y) \quad (28b)$$

$$Mx_2(x, y) = \sum_{r=x}^{r+L-1} SumX(r, y) \times W_2^{int}(r-x) \quad (29a)$$

$$My_2(x, y) = \sum_{c=y}^{y+L-1} SumY(x, c) \times W_2^{int}(c-y) \quad (29b)$$

$$Mx_3(x, y) = \sum_{r=x}^{r+L-1} SumX(r, y) \times W_3^{int}(r-x) \quad (30a)$$

$$My_3(x, y) = \sum_{c=y}^{y+L-1} SumY(x, c) \times W_3^{int}(c-y) \quad (30b)$$

As mentioned above, the effectiveness of using the three possible pairs of moments combinations, to compute the blocks descriptors that used for indexing to speeding up the range-domain search task, {that is, (M_1, M_2) , (M_1, M_3) , and (M_2, M_3) } have been investigated.

The proposed range pool partitioning scheme

The proposed partitioning scheme that applied to generate the range pool blocks is the quadtree; it partitions the range array into nonoverlapped variable length blocks. Two criteria have been used to guide the decomposition process; the first is based on the edge detection using Sobel filter (see equations 31a and b) and the second based on the contrast (see equation 32). The permissible block length (PBL) is 8 and 4:

$$G_x = \begin{bmatrix} -1 & -2 & -1 \\ 0 & 0 & 0 \\ 1 & 2 & 1 \end{bmatrix} \quad (31a)$$

$$G_y = \begin{bmatrix} -1 & 0 & 1 \\ -2 & 0 & 2 \\ -1 & 0 & 1 \end{bmatrix} \quad (31b)$$

For the block addressed as $\begin{bmatrix} (x, y) & (x, y+1) \\ (x+1, y) & (x+1, y+1) \end{bmatrix}$ the maximum variance around the pixel (x,y) is computed as

$$Max_{var} = \text{Max} \left(\begin{array}{l} |pixel(x, y) - pixel(x, y+1)|, \\ |pixel(x, y) - pixel(x+1, y)|, \\ |pixel(x, y) - pixel(x+1, y+1)| \end{array} \right) \quad (32)$$

The regions threshold determined according to the following relation:

$$Thr_Q = \begin{cases} val_{var} & \text{if use } Max_{var} \\ val_{Sobel} & \text{if use } Max_{Sobel} \end{cases} \quad (33)$$

Where $val_{var} \in \{10, 12, 14, \dots, 30\}$, while $val_{sobel} \in \{30, 35, 40, \dots, 90\}$. These threshold values were selected after comprehensive tests.

The partitioning process started by partitioning the range array into nonoverlapped block of size equal to (8). For each block, one of the following steps is done:

- If Sobel filter used as a decision to partition the current block, then the highest value between G_x or G_y over the tested block determined,
- If the maximum variance is used as a decision to partition this block, then the maximum variance over all pixels belong to the block are determined.

If the determined value exceeds the predetermined Thr_Q , then split the block into four quadrants.

Fig. 3a shows the well-known Baboon image after applying the proposed partitioning scheme that used Sobel as partitioning decision (where the threshold value val_{sobel} is set 40). While Fig. 3b shows the well known Lenna image after applying the proposed partitioning scheme that based on maximum variance as partitioning decision (where the threshold value $val_{variance}$ is set to 22).

Enhanced FIC encoding process

The introduced enhanced encoding algorithm of the range blocks are summarized by the following steps:

- a) Load BMP image and put it in (R,G,B) array (three 2D arrays)
- b) Convert (R,G,B) array to (Y,U,V) array
- c) Downsample the components U and V
- d) Determine the moment combinations used
- e) For each color component (that is, the original Y, and the downsampled [U,V]) do the followings:
 1. Construct the domain and range pools. This process is done by partitioning the range array into nonoverlapping variable blocks (using the above-mentioned quadtree method with one of the partitioning decision stated in section 2.4.2) to generate the range $(r_0 \dots r_{n-1})$ blocks.
 2. Set the PBL to 8.
 3. The downsampled range array (that is, the domain array) is partitioned into overlapped fixed blocks of size equal to PBL to generate the domain $(d_0 \dots d_{m-1})$ blocks.
 4. For each domain block listed in domain pool do the following:
 - i. Determine the average (\bar{d}) using equation 3.
 - ii. Determine the $(n\sigma_d^2)$ as:

$$n\sigma_d^2 = \sum_{i=0}^{n-1} d_i^2 - n\bar{d}^2 \quad (34)$$

- iii. Determine the moments using equations (28-30) that corresponding to the selected moments.
 - iv. Determine the moment ratio for each moment using equation 16.
 - v. Determine the moment index value using equation 17.
 - vi. Determine the block isometric index (Sym_indxd) that based on moment order one (that is, equations (14,15) and Table III).
5. Store the position coordinates (x_d, y_d) of the domain blocks and the calculated moment index in temporary array (L) of record.
 6. Sort the array of record (L) in ascending order according to their moment index.
 7. Establish a set (P) of pointers referring to the start and end of records holding the same index value.
 8. For each range, block of size equal to PBL do the following:
 - i. Calculate the average (\bar{r}) using equation 2.
 - ii. Determine the ($n\sigma_d^2$) as:

$$n\sigma_r^2 = \sum_{i=0}^{n-1} r_i^2 - n\bar{r}^2 \quad (35)$$
 - iii. Determine the moments using equations (28-30) that corresponding to the selected moments.
 - iv. Determine the moment ratio for each moment using equation 16.
 - v. Determine the moment index value using equation 17.
 - vi. Determine the block isometric index (Sym_indxr) that based on moment order one (that is, equations (14, 15) and Table III).
 9. With help of pointers set (p) and the temporary list of records (L); match only the domain blocks whose moment index values equal to the range index value.
 10. The parameters Sym_indxr and sym_indxd are passed through the isometric predictor; the predictor will output

the index of the required isometric transform (using Table IV). Then, apply the assigned transform on the tested range block.

11. The proposed enhanced steps for fast computation of s and χ^2 is applied using the following equations:

$$\phi = \sum_{i=0}^{n-1} r_i d_i - n\bar{r}\bar{d} \quad (36)$$

$$s = \frac{\phi}{n\sigma_d^2} \quad (37)$$

$$\chi^2 = n\sigma_r^2 + s^2 n\sigma_d^2 - 2s\phi \quad (38)$$

Then, calculate the scale coefficient (s) and (χ^2) of first class of the domain blocks with range block and apply the following steps:

- i. Compare the result (χ^2) of each matching instance with the (χ^2_{\min}) that registered during the previous matching instances. If the compared (χ^2) is smaller than (χ^2_{\min}), then put its value in (χ^2_{\min}) and register (s) beside to the average mean value of range block and the position and symmetry state (sym) of the domain block.
 - ii. If the (χ^2_{\min}) < *minimum blockerror*, then the search across the domain blocks is stopped and the registered domain blocks are considered as the best match, output the set values (position, symmetry state, s , \bar{r}) and go to 4.
 - iii. Otherwise, start test the domain blocks that closest higher class.
12. Divide PBL by 2, if the result equal to 2 then, stop the search, else go to 3.

III. TEST RESULTS

The proposed system was implemented using Embarcadero RAD Studio 2010 Visual Pascal Programming Language programming language. The tests were conducted under the environment: Windows-8 operating system, laptop computer - Lenovo (processor: Intel (R) Core(TM) i5-3337U, CPU 1.8 GHz, and 4GB RAM). The tests were applied on the well-known Lena and Baboon image samples (whose specifications are: Size = 256 × 256 pixel, color depth = 24 bit). To assess the difference between the reconstructed image and the original images, the error measures (that is, mean square error MSE and peak signal

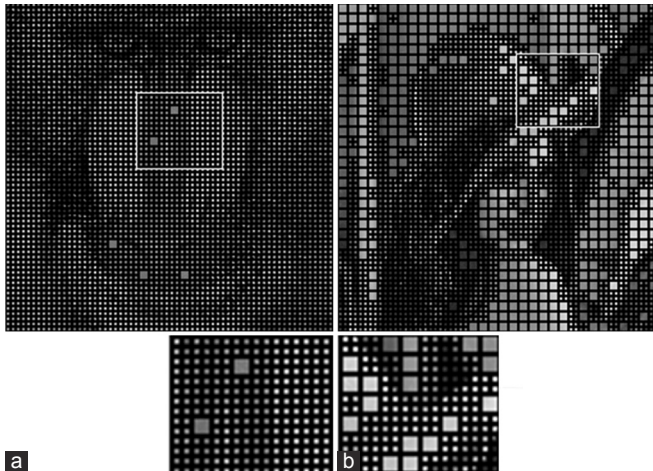


Fig. 3. (a and b) The proposed variable partitioning scheme applied on some test images.

TABLE V
THE VALUES OF THE CONTROL PARAMETERS

Parameter	Range or value
S_{\max}	3
bs	6
br	8
Minimum Block Error	1
Val _{variance}	{10,12,14,..,30}
Val _{Sobel}	{30,35,40,..,90}
Nm	{25,30,35,..,50}

to noise ratio PSNR measured in dB) were used. Beside these fidelity measures, some complementary measures were used to describe the performance of the system; both the CR and bit rate parameters (BR) were used to describe the compression gain.

Table V lists the considered control parameters (including their names and default values); these values were selected after making comprehensive tests.

Table VI lists the notations with their descriptions that are used in the figures and tables presented in this section.

A. Moment Combination Test

In this set of tests, the effects of using the different combinations of proposed moments are illustrated, when the blocks have been partitioned fixedly to (4×4). (that is, PFIC4) as listed in Tables VII and VIII.

The parameters values listed the shaded rows in Tables VII and VIII were adopted to study the effect of the proposed moment combinations' on (CR, ET, and PSNR) with the test samples explained in Fig. 4.

From the listed results, it is obvious that T1 is the best-balanced combination. Since if the combinations sorted

TABLE VI
THE NOTATIONS USED IN THE TEST RESULTS

Notation	Description
T0	The moment index ratio computed from the combination of M1 and M2
T1	The moment index ratio computed from the combination of M1 and M3
T2	The moment index ratio computed from the combination of M2 and M3
PFIC4	The proposed FIC applied with fixed block partitioning of size equal to 4
PFIC8	The proposed FIC applied with fixed block partitioning of size equal to 4
PFICS	The proposed FIC applied with quadtree partitioning scheme that used Sobel as partitioning decision
PFICV	The proposed FIC applied with quadtree partitioning scheme that used variance as partitioning decision

TABLE VII
TEST RESULTS OF PFIC4 WHEN APPLIED ON LENA IMAGE

Moments combination	Nm	CR	MSE	PSNR	BR	ET (s)
T0	25	8.021	94.062	28.397	2.992	0.313
	30	8.027	8.021	28.262	2.990	0.235
	35	7.963	94.106	28.395	3.014	0.252
	40	7.964	97.966	28.220	3.013	0.244
	45	7.967	100.526	28.108	3.012	0.231
T1	50	7.980	106.446	27.860	3.008	0.235
	25	8.027	95.281	28.341	2.990	0.250
	30	8.014	100.351	28.116	2.995	0.192
	35	7.964	95.647	28.324	3.014	0.212
	40	7.965	99.035	28.173	3.013	0.218
T2	45	7.974	102.785	28.012	3.010	0.208
	50	7.977	107.596	27.813	3.009	0.209
	25	8.026	90.288	28.575	2.990	0.324
	30	8.032	96.783	28.273	2.988	0.247
	35	7.964	92.078	28.489	3.013	0.268
	40	7.969	98.046	28.217	3.012	0.259
	45	7.981	100.263	28.119	3.007	0.256
	50	7.983	103.335	27.988	3.006	0.254

according to the maximum CR, the result is (T2, T0, and then T1), and the lowest attained ET result is (T1, T0, and then T2). It is difficult to arrange (T0, T1, and T2) according to the PSNR because there is no significant difference with test images.

B. PFIC4 and PFIC8 Versus PFICS Test

In this section, the proposed FIC was applied with quadtree partitioning scheme that using Sobel filter as partitioning decision (PFICS). The tests were conducted to investigate the effect of the proposed quadtree partitioning with moment combination versus fixed block partitioning (PFICL); the value of L is set equal to (4 and 8) with same moment combinations listed in Table IX. Fig. 5 illustrates

TABLE VIII
TEST RESULTS OF PFIC4 WHEN APPLIED ON BABOON IMAGE

Moments combination	Nm	CR	MSE	PSNR	BR	ET (s)
T0	25	8.017	489.506	21.233	2.994	0.221
	30	7.984	499.533	21.145	3.006	0.199
	35	7.948	516.252	21.002	3.020	0.183
	40	7.952	519.355	20.976	3.018	0.194
	45	7.952	529.911	20.889	3.018	0.183
T1	50	7.952	549.678	20.730	3.018	0.182
	25	8.016	493.163	21.201	2.994	0.204
	30	7.985	503.922	21.107	3.006	0.187
	35	7.947	518.631	20.982	3.020	0.176
	40	7.950	521.902	20.955	3.019	0.188
T2	45	7.952	535.173	20.846	3.018	0.176
	50	7.951	549.090	20.734	3.019	0.179
	25	8.025	484.939	21.274	2.991	0.259
	30	7.990	497.737	21.161	3.004	0.228
	35	7.952	506.847	21.082	3.018	0.215
	40	7.951	513.062	21.029	3.018	0.219
	45	7.951	523.084	20.945	3.019	0.211
	50	7.952	539.883	20.808	3.018	0.207

TABLE IX
TEST RESULTS FOR PFICS AND PFICS WHEN THE MOMENT COMBINATION IS T1, NM=50, AND THE TESTED SAMPLE IS BABOON IMAGE

A. PFICS results						
Val _{Sobel}	CR	MSE	PSNR	BR	ET (sec)	
30	8.160	568.479	20.584	2.941	0.116	
35	8.401	571.162	20.563	2.857	0.110	
40	8.603	573.228	20.548	2.790	0.105	
45	8.774	574.969	20.534	2.735	0.105	
50	9.033	578.903	20.505	2.657	0.101	
55	9.247	580.188	20.495	2.595	0.098	
60	9.432	584.204	20.465	2.544	0.096	
65	9.608	585.074	20.459	2.498	0.095	
70	9.752	587.470	20.441	2.461	0.095	
75	9.930	590.511	20.419	2.417	0.096	
80	10.060	593.388	20.397	2.386	0.093	
85	10.292	599.283	20.355	2.332	0.093	
90	10.477	604.115	20.320	2.291	0.090	
B. PFIC4 and 8 results						
L	CR	MSE	PSNR	BR	ET (s)	
4	7.951	549.090	20.734	3.019	0.179	
8	31.829	844.843	18.863	0.754	0.053	

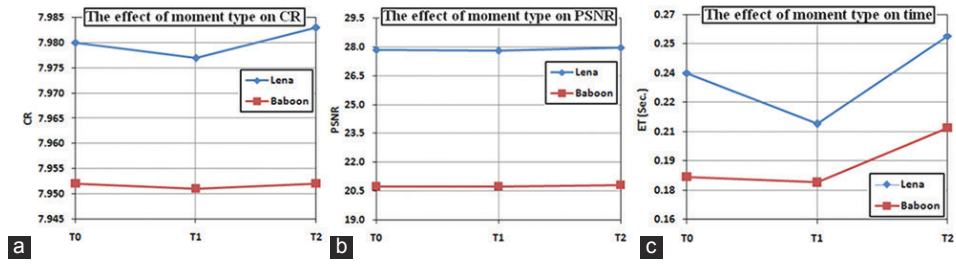


Fig. 4. (a-c) The effect of moment type with test images.

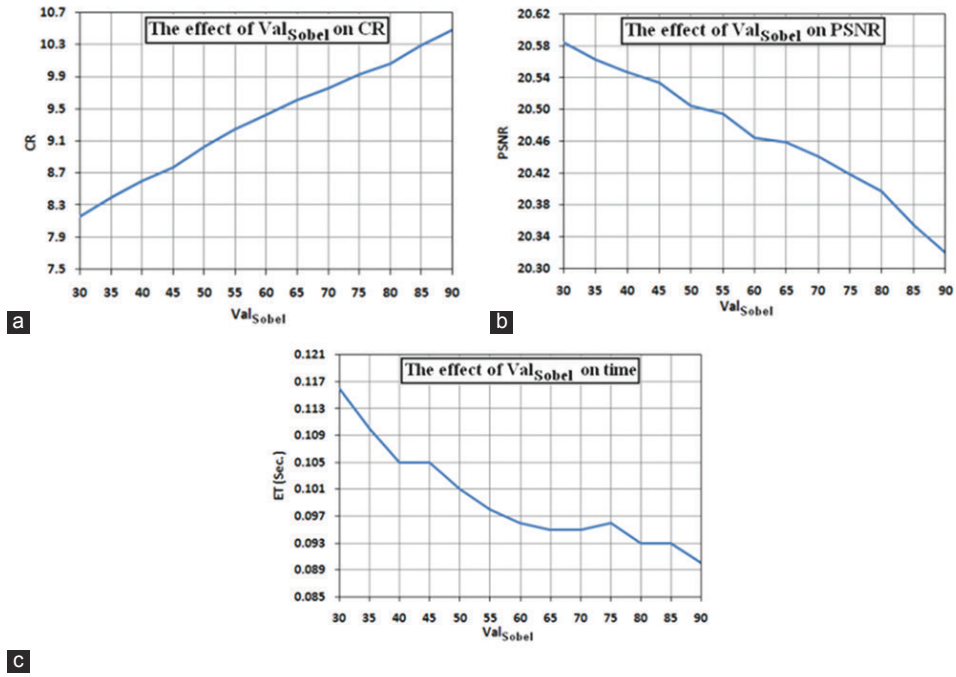


Fig. 5. (a-c) The effect Val_{Sobel}

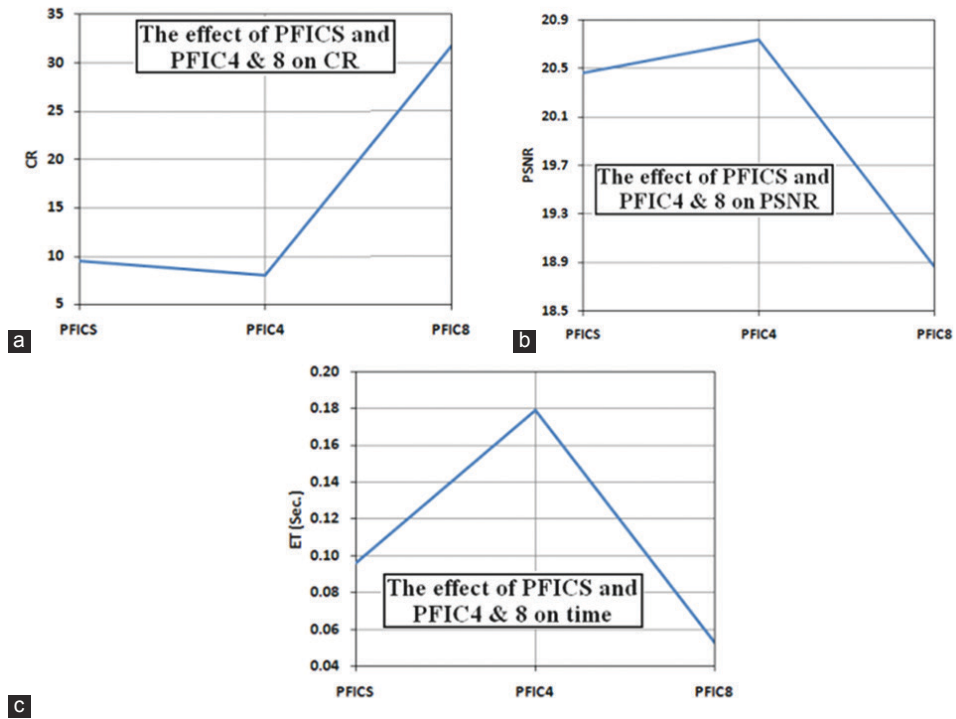


Fig. 6. (a-c) The effect of proposed variable partitioning scheme using Sobel with fixed one.

the effect of Val_{Sobel} on CR, ET, and PSNR when PFICS had been applied.

The parameters values in the listed shaded rows of Table IX have been used to compare the performance of variable and fixed partitioning scheme; the attained results are presented in Fig. 6.

C. PFIC4 and PFIC8 Versus PFICV Test

In this section, the proposed FIC was applied with quadtree partitioning scheme that using max variance as

partitioning decision (PFICV). The tests were conducted to investigate the effect of the proposed quadtree partitioning with moment combination versus (PFICL) fixed block partitioning; the value of L is set to (4 and 8) with the same moment combinations listed in Table X. Fig. 7 illustrates the effect of $Val_{variance}$ on CR, ET and PSNR when PFICV was applied.

The parametric values of the shaded rows listed in Table X have been used to extract the results shown in Fig. 8 to compare the performance of variable and fixed partitioning scheme.

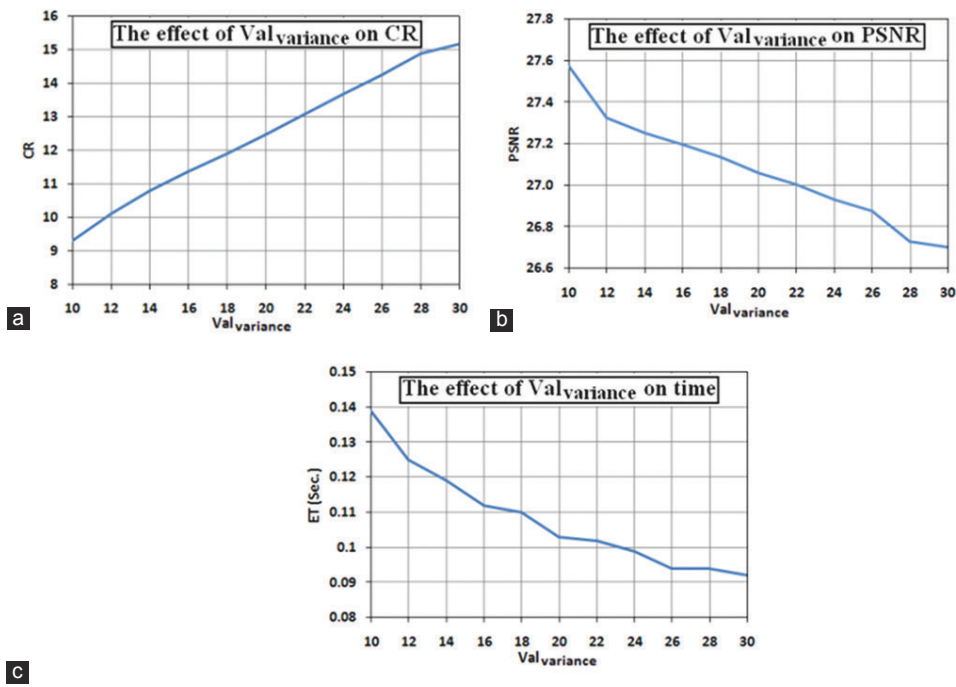


Fig. 7. (a-c) The effect $Val_{variance}$.

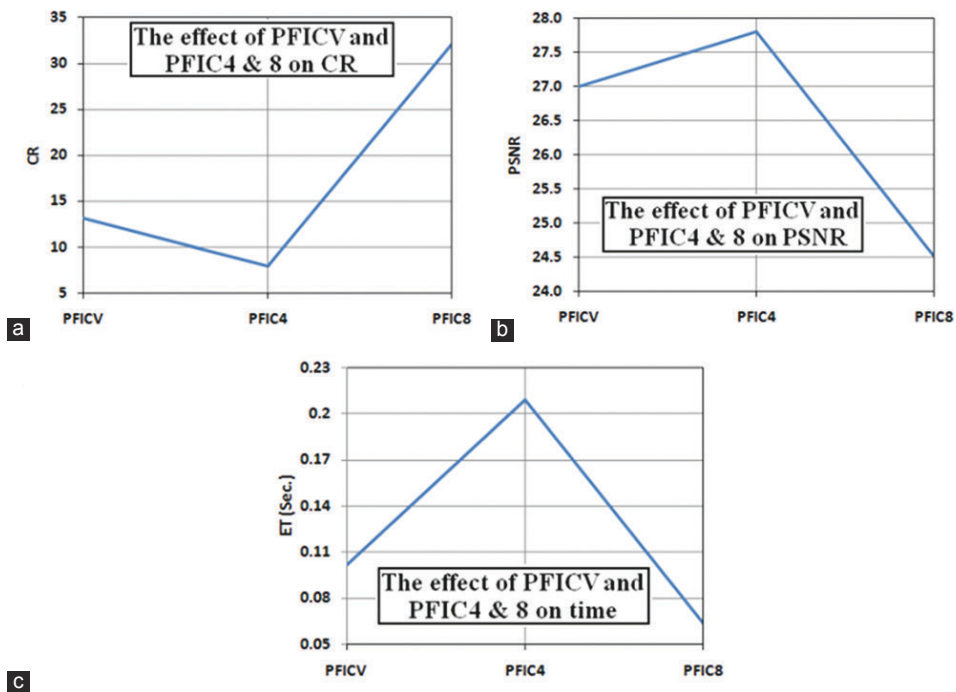


Fig. 8. (a-c) The effect of the proposed variable partitioning scheme using max variance with fixed one.

TABLE X.

PFICS TEST WHEN MOMENT COMBINATION IS T1, NM=50 AND THE TEST IMAGE IS LENA

A. PFICV results					
Val _{variance}	CR	MSE	PSNR	BR	ET (sec)
10	9.321	113.734	27.572	2.575	0.139
12	10.108	120.344	27.327	2.374	0.125
14	10.803	122.395	27.253	2.222	0.119
16	11.377	123.949	27.198	2.110	0.112
18	11.919	125.725	27.137	2.014	0.110
20	12.497	128.012	27.058	1.921	0.103
22	13.095	129.634	27.004	1.833	0.102
24	13.705	131.865	26.930	1.751	0.099
26	14.280	133.470	26.877	1.681	0.094
28	14.886	138.039	26.731	1.612	0.094
30	15.184	138.930	26.703	1.581	0.092
B. PFIC4 and 8 results					
L	CR	MSE	PSNR	BR	ET (s)
4	7.977	107.596	27.813	3.009	0.209
8	32.115	229.912	24.515	0.747	0.064

IV. CONCLUSIONS

From the results of tests conducted on the proposed system, the following remarks were stimulated:

1. The quadtree partitioning that guided by Sobel or variance can be considered as useful partitioning mechanism.
2. The proposed FIC that uses double moment with variable partitioning schemes produces better results than that of fixed partitioning as shown in Figs. 6 and 8.
3. The proposed moments are suitable to perform double block description which in turn can significantly speed up the IFS encoding process.
4. For future work:
 - a. A new criteria could be adopted for quadtree partitioning.
 - b. Investigate the combination of triple moments.

REFERENCES

- Al-Hilo, E.A. and George, L.E., 2008. Speeding-up fractal colored image compression using moments features. *IEEE, Digital Image Computing: Techniques and Applications, DICTA*, 2008, pp.486-490.
- George, L.E and Minas, N.A., 2011. Speeding up fractal image compression using DCT descriptors. *Journal of Information and Computing Science*, 6, pp.287-294.
- George, L.E. and Al-Hilo, E.A, 2011. Speeding-up Fractal Color Image Compression Using Moments Feature Based on Symmetry Predictor, *IEEE, Computer Society, Eighth International Conference on Information Technology: New Generations*, Las Vegas, NV, pp. 508-513.
- George, L.E. and Al-Hilo, E.A., 2008. Speeding-up Fractal Colored Image Compression Using Moments Features, *International Conference on Computer and Communication Engineering*, pp. 1303-1307.
- George, L.E. and Al-Hilo, E.A., 2009. Fractal Color Image Compression by Adaptive Zero-Mean Method, *IEEE Computer Society, International Conference on Computer Technology and Development*, pp.525-529.
- George, L.E. and Al-Hilo, E.A., 2009. Speeding-Up Color FIC Using Isometric Process Based on Moment Predictor, *International Conference on Future Computer and Communication, IEEE Computer Society*, pp.607-611.
- George, L.E. and Mahmoud, S.L., 2011. Image steganography using an accelerated affine Block matching scheme. *International Journal of Computer Information Systems*, 2, pp.1-7.
- George, L.E., 2006. IFS coding for zero-mean image blocks, university of Baghdad, college of science, Iraqi. *Journal of Science*, 47, pp. 190-194.
- Mahadevaswamy, H.R., 2000. *New Approaches to Image Compression, Ph.D. Thesis, Regional Engineering College*, University of Calicut.
- Mahmoud, S.L., 2012. The use of double moment based descriptors to speed up FIC. *Journal of Al-Nahrain University, Science*, 15, pp. 200-202.
- Ning, L., 2007. *Fractal Imaging, a Book*. Academic Press, New York.
- Xi, L. and Zhang, L., 2007. A study of fractal image compression based on an improved genetic algorithm. *International Journal of Nonlinear Science*, 3, pp.116-124.

Facial Expression Recognition Using Uniform Local Binary Pattern with Improved Firefly Feature Selection

Abdulla M. K. Elmadhoun, and Md. Jan Nordin

Department of Computer Science, Faculty of Information Science and Technology, Universiti Kebangsaan Malaysia, Bangi, Malaysia

Abstract—Facial expressions are essential communication tools in our daily life. In this paper, the uniform local binary pattern is employed to extract features from the face. However, this feature representation is very high in dimensionality. The high dimensionality would not only affect the recognition accuracy but also can impose computational constraints. Hence, to reduce the dimensionality of the feature vector, the firefly algorithm is used to select the optimal subset that leads to better classification accuracy. However, the standard firefly algorithm suffers from the risk of being trapped in local optima after a certain number of generations. Hence, this limitation has been addressed by proposing an improved version of the firefly where the great deluge algorithm (GDA) has been integrated. The great deluge is a local search algorithm that helps to enhance the exploitation ability of the firefly algorithm, thus preventing being trapped in local optima. The improved firefly algorithm has been employed in a facial expression system. Experimental results using the Japanese female facial expression database show that the proposed approach yielded good classification accuracy compared to state-of-the-art methods. The best classification accuracy obtained by the proposed method is 96.7% with 1230 selected features, whereas, Gabor-SRC method achieved 97.6% with 2560 features.

Index Terms—Facial expression recognition, feature selection, firefly algorithm, optimization.

I. INTRODUCTION

Automated analysis of facial expressions has been gaining momentum in the field of computer vision over the past few years. Interestingly, facial expressions contribute a significant part of the nonverbal communication between human beings (Khatri, et al., 2014). Developing automated systems to recognize human emotions with good accuracy and speed under different imaging variations such as illumination and scale have been gaining considerable attention (Khatri,

et al., 2014; Jamshidnezhad and Nordin, 2013). The successful application of the texture descriptors motivated the use of local binary pattern (LBP) for face representation (Ojala, et al., 2002; Hamid and Nordin, 2016). However, the essential problem of using local descriptors is the high dimensionality of the data. High dimensional data can decrease the speed and accuracy of the classifier (Bereta, et al., 2013; Alsalibi, et al., 2015). High dimensionality not only effects recognition accuracy but also imposes computational constraints (Alsalibi, et al., 2017). Hence, employing an optimization feature selector is essential for eliminating redundant and irrelevant features so as to provide highly discriminating feature representation.

Firefly algorithm is a metaheuristic algorithm inspired by the social behavior of a group of fireflies. It was introduced by Yang in 2010 (Yang, 2010). During the optimization process, the algorithm attempts to move the fireflies as inspired by the interaction of real fireflies. As each firefly produces light based on the phenomenon of bioluminescence, certain suggestions are made in the algorithm. In principle, each firefly will be exploring and searching for other fireflies and preys randomly. However, the main limitation of the classical firefly algorithm is the risk of being trapped in local optima due to the loss of population diversity during the optimization process (He and Huang, 2017).

Hence, the aim of this paper is to propose an automatic facial expression recognition system using uniform LBP descriptor and a modified firefly optimization algorithm. Approximately, the improved version of the firefly algorithm has been used to select the optimal set of discriminating features so as to alleviate the cause of dimensionality associated with the use of uniform LBP descriptor.

The rest of this paper is organized as follows: Section 2 provides a brief description of the classical firefly algorithm and the modified firefly algorithm. The application of the improved firefly algorithm in facial expression recognition is presented in Section 3. Experimental results and discussions are presented in Section 4. Finally, Section 5 concludes the paper and gives some suggestions for the future work.

II. FIREFLY ALGORITHM

A brief description of the classical firefly algorithm and the modified firefly algorithm is presented in the following subsections.

ARO-The Scientific Journal of Koya University
Volume VI, No.1 (2018), Article ID: ARO.10378, 10 pages
DOI: 10.14500/aro.10378

Received 04 February 2018; Accepted: 24 March 2018

Regular research paper: Published 09 April 2018

Corresponding author's, e-mail: p74470@siswa.ukm.edu.my

Copyright © 2018 Elmadhoun AMK, Nordin MJ. This is an open-access article distributed under the Creative Commons Attribution License.



A. The classical FA algorithm

Firefly Algorithm is a metaheuristic algorithm which simulates the social behavior of a group of fireflies. The search pattern of FA is determined by the attractions among fireflies, whereby a less bright firefly moves toward a brighter firefly. However, the flashing lights depend on some physics factors. One of these factors is the light intensity I which decreases when the distance r increases. The mapping of firefly algorithm to the optimization context can be represented as follows. Randomly generated feasible solutions are called fireflies which will be assigned with a light intensity based on their performance in the objective function. This intensity will be used to compute the brightness of the firefly, which is directly proportional to its light intensity. For minimization problem, a solution x with smallest functional value will be assigned with highest light intensity. Once the intensity or brightness of the solutions is assigned, each firefly will follow fireflies with better light intensity. For the brightest firefly, since there is no other brighter firefly to follow, it will perform a local search by randomly moving in its neighborhood.

In FA algorithm, the light intensity I of a firefly at a location x is associated with the value of objective function. In addition, it decreases as the distance r increases, so the expression of light intensity is as presented in equation 1:

$$I(r) = I_0 e^{-Yr^2} \quad (1)$$

Where, I_0 is the light intensity of the source and Y is the fixed light absorption coefficient. The attractiveness β is proportional to the light intensity $I(r)$. Thus, it can be defined by (2) as follows:

$$\beta = \beta_0 e^{-Yr^2} \quad (2)$$

Where, the parameter β_0 denotes the attractiveness at the distance $r=0$. Each firefly X_i is compared with all other fireflies X_j , where $J \neq i$. If X_j is brighter (better) than X_i , X_i will be attracted to and move toward X_j . The movement of X_i can be defined by equation 3.

$$r_{ij} = \|X_i - X_j\| = \sqrt{\sum_{d=1}^D (X_{id} - X_{jd})^2} \quad (3)$$

Note that r_{ij} is the distance between X_i and X_j , D is the dimension of the problem. When firefly X_i is attracted to another firefly X_j , the movement from firefly X_i to firefly X_j is defined as follow:

$$X_{id}(t-1) = X_{id}(t) + \beta_0 e^{-Yr_{ij}^2} (X_{jd}(t) - X_{id}(t)) + \alpha \epsilon_i \quad (4)$$

Where ϵ_i is a random number uniformly distributed in the range $[-0.5, 0.5]$ and $\alpha \in [0, 1]$ is the step factor.

B. Improved FA algorithm

In this section, the improved version of the FA algorithm is presented. The classical FA algorithm still encounters serious problems in large-scale databases. In such cases, the key shortcomings of the FA are the risk of being trapped in local minima (premature convergence) and the slow convergence rate. In this context, striking a balance between exploration and exploitation (intensification) is essential to cope with such limitations. The classical FA algorithm mimics the social behavior of fireflies based on the flashing and attraction that

typically involves interaction between different fireflies in the swarm. To enhance the performance of such interactions and to improve the trajectories of fireflies, the great deluge local search algorithm has been hybridized with FA.

In the past few years, FA algorithm has been modified in many ways to improve the search capabilities of the algorithm (Tilahun, et al., 2017; Tilahun and Ngnotchouye, 2017; Mistry, et al., 2017). Mainly modifications have focused on the light intensity and attractiveness factors. For example, (Tilahun and Ong, 2012) have modified the FA algorithm by modifying the random part in the movement formula. If there is a firefly in the current best position and there is no improvement, this may reduce the brightness. Hence, they modified it by moving the firefly to other directions to achieve the best performance by improving the brightness of firefly using m uniform random vector. However, if there is no direction that the firefly can move to, the firefly stays in the same position. This modification has been tested using seven benchmark functions, and the modified FA algorithm obtained better results than the classical FA algorithm.

In (Palit, et al., 2011), Palit introduced the binary firefly algorithm to find the plain text from cipher text, using Merkle-Hellman knapsack cipher algorithm. In their work, a new representation of the problem was considered using the firefly algorithm. The result of the FA algorithm was compared with GA, and they found that the binary firefly is better than the genetic algorithm for solving this problem.

Recently, Wang et al. (2017b) presented a new adaptation mechanism for FAs' parameter called adaptive control parameters (ApFA). Comparative assessment in simulations of ApFA with standard FA and other variants of FA on benchmark functions have shown that ApFA outperformed those algorithms. In addition, Wang et al. (2017b) also proposed NSRaFA in which three neighborhood searches and a new randomization model are employed to improve the exploration and exploitation abilities. The algorithm proposed is also capable of adjusting the control parameters automatically during the search process.

C. The GDA

GDA is a variant of simulated annealing local search algorithm (Yang, 2010) known for its ability to maintain the diversity of the population and avoid the trap in local minima. The distinguishing characteristic of GDA is its deterministic level-based acceptance criterion (He and Huang, 2017). Besides the acceptance criterion, GDA requires only one parameter (called decay rate) to be determined to control the acceptance of the nonimproving solutions, which is the reason behind the selection of GDA in this work. In addition to accepting improving solutions, keeping a maximization problem in mind, GDA can accept a nonimproving solution given that its fitness is greater than or equal to a dynamically updated value (called the level).

D. GD-FA procedure

Hybridizing GD algorithm with firefly algorithm can prevent the later from being stuck in local optima, especially

after the longtime of generations. Furthermore, it can help the firefly algorithm to obtain the best accuracy in less number of function evaluations. This improvement can be done by applying the GD algorithm for each candidate solution (firefly) in the current generation. Each firefly performs a local search, and the generated solution will replace the old solution based on the acceptance criteria. This can be performed by sending the firefly values to the GDA algorithm as initial solutions. Basically, the GDA algorithm starts by generating new neighbors by changing random number of bits from binary 0 to 1 or vice versa. Then, it calculates the accuracy (Fitness) of the new generated solution. After that, GDA compares the fitness of the new solution with the local best, if the new solution is better than the local best, the algorithm will replace the local best and current solution with the new solution. Besides that, the value of the water level will be linearly increased using $\Delta\beta$. The GDA process will be iterated until the termination condition is encountered which is set to be reaching the maximum number of iterations. However, if the local best is better than the new solution, the algorithm will decide whether to accept the new solution as a current solution or not according to the water level value. If the fitness of the new solution is greater than the water level, then it will accept the new solution, otherwise, the algorithm will start generating a new solution and continue the evolution process. After applying the local search for all fireflies in the generation, the firefly will continue processing the fireflies by applying the movement equation. Fig. 1 shows a step by step summary of the GD-FA algorithm.

The procedure of GD-FA algorithm can be summarized as follows:

1. Initialize the first generation of fireflies randomly.
2. Send each firefly values to GDA in the generation.
 - a. The current solution and local best will be equal to the solution sent from FA.
 - b. Calculate the accuracy (fitness) of the current solution.
 - c. Generate new solution from current solution by changing a random number of bits.
 - d. Calculate the accuracy (fitness) of the new solution.
 - e. If new solution is better than local best, replace local best and current solution with new solution.
 - f. If local best is better than the new solution and a new solution is greater than the water level, then replace current solution with new solution.
 - g. If neither e nor f, then start again from c.
 - h. Update water level.
 - i. If stop criteria have been met send back the local best to FA.
3. Find the local best in the generation.

If the local best is better than the global best, update the global best. Note that, initially, the value of the Global best is equal to zero.
4. Apply movement to all fireflies, and create a new generation.
5. Fix invalid values in each firefly to be binary 0 or binary 1 in the new generation.
6. Redo 2–6 until it reaches to a maximum number of generations.

III. APPLICATION OF IMPROVED FIREFLY ALGORITHM FOR FACIAL EXPRESSION RECOGNITION SYSTEM

Typically, the facial expression recognition process consists of three main phases which are (face detection, feature extraction, and classification) for static images. In the face detection phase, the input image is processed to extract the face region from the original image. Thereafter, some preprocessing steps are applied such as converting the image to grayscale image, resizing the cropped face and preparing it for feature extraction. The output of the feature extraction process is a representation of the face image in a feature vector with length equals to the number of features extracted from the image. After applying the face detection and feature extraction to all images in the dataset, a dataset containing all features of all faces in the dataset has been generated, which will be ready to be trained using one of the training algorithms such as support vector machine, k-nearest neighbor, neural networks, and other training algorithms which also called the classification process.

Interestingly, it is possible to add other phases to the recognition process pipeline to improve the accuracy and performance of the overall model. In this paper, the feature selection process is added after feature extraction process to select the most important features from the extracted feature space and exclude the redundant and noisy features that could negatively affect the classification accuracy, where those excluded features will be considered as noise. The feature selection process can be performed by many techniques, mostly by artificial intelligence methods which search for the best combination of features to achieve the best accuracy.

A. Face detection stage

The detection of faces in images is the first step in any typical facial recognition system. The main purpose of face detection is to detect the presence of faces in the image and their corresponding location. For this purpose, the well-known Viola–Jones face detector algorithm has been used to detect the face region due to its accuracy, speed, and straightforward implementation in MATLAB using the computer vision toolbox. First, the face and eyes will be detected by Viola–Jones face detector; each eye will be framed by square where the center of the square will be the center of the eyes. Then, by detecting the center of the eyes the face will be normalized by making the distance between the eyes equals 55 pixels. Based on that, the face will be cropped and resized to 110×150 pixels. Fig. 2 shows an illustrative example of the face detection process.

B. Feature extraction stage

In this stage, informative features are extracted from face images. Bearing in mind that not all pixels in an image contain reliable features, extracting meaningful features sufficient to represent the face is an essential step. The extracted features should minimize intraclass variations caused by different illumination conditions while maximizing interclass variations.

LBP has been first proposed by Ojala, et al. and since then it has become one of the most widely used local descriptors

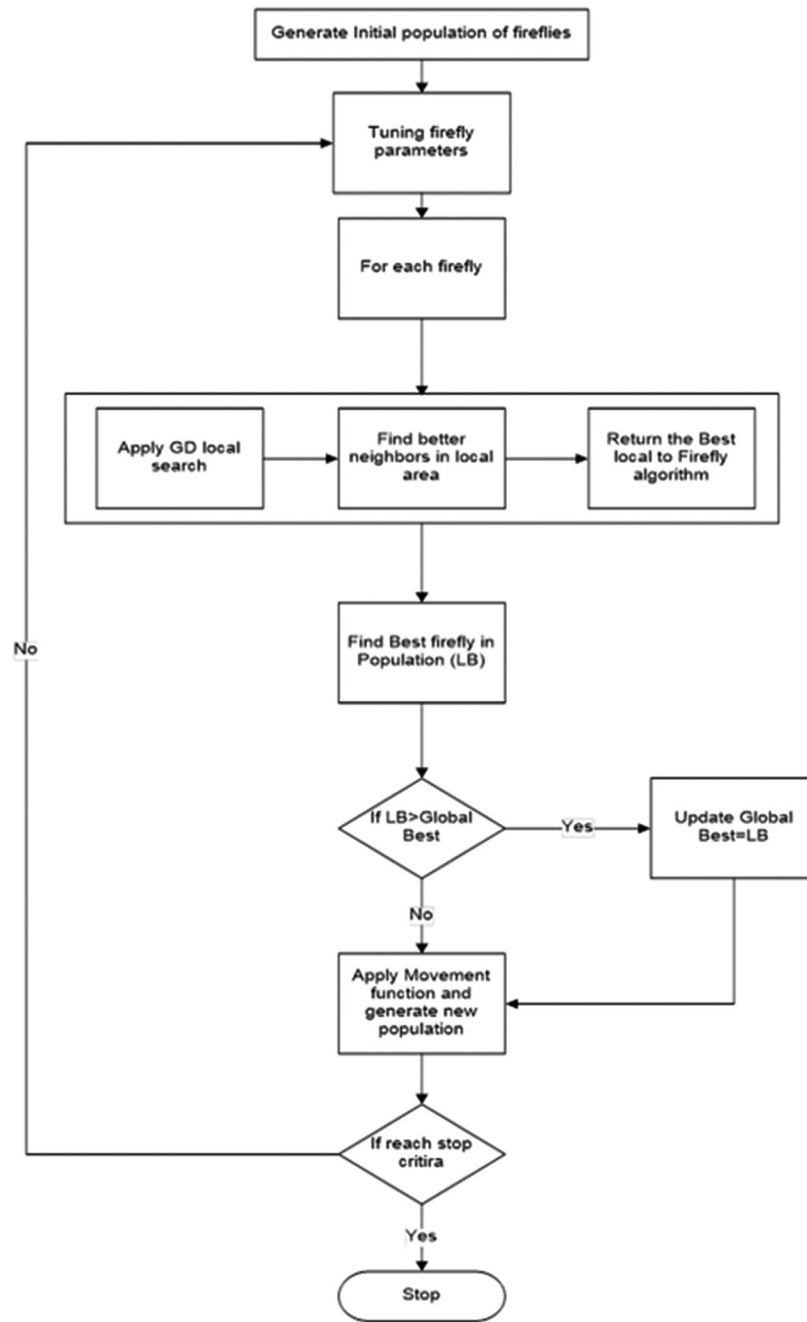


Fig. 1. GD-FA process

due to its computational simplicity and invariance to different lighting conditions (Ojala, et al., 2002). Although the standard LBP is relatively insensitive to monotonic gray level changes, its main limitation is the sensitivity toward noisy pixels wherein the value of the pixels can be easily affected by the erroneous surrounding pixels (Bereta, et al., 2013). In this phase, after detecting the face region and cropping it, the system will extract the features from the face image using uniform LBP (uLBP) as illustrated in 5–8. Following the literature, for extracting the uLBP features from the face, the face will be divided into 42 regions, each region with a size of 18x21 pixels, and then feature extraction will be applied in each region to generate 59 features by applying uLBP (5-8). In the end, all regions will

be combined and concatenated together in one feature vector. Note that, this combined feature vector includes 2478 features for representing one face image. By applying the same process to all Japanese Female Facial Expression (JAFPE) dataset, a features matrix with a size of 213×2478 will be created and prepared for feature selection process.

$$LBP_{p,r}(Z_c) = \sum_{p=0}^{p-1} \delta(g_p - g_c) 2^p \quad (5)$$

$$U(P) = P(P-1) + 2 \quad (6)$$

$$h_1 = \sum B(L(Z_c) = 1), 1 = 0, \dots, ((U(P) + 1) - 1) \quad (7)$$

$$B(x) \begin{cases} 1 & \text{if } x \text{ is true} \\ 0 & \text{Otherwise} \end{cases} \quad (8)$$

Fig. 3 shows a sample of feature extraction process applied to a face image.

C. Feature selection stage

In pattern recognition context, the term of facial feature selection refers to the mining mechanism that looks for a subset of features from the feature pool that is sufficient to maximize the interclass and minimize the intraclass discrimination between different classes. Feature selection not only reduces the feature vector dimensionality but also reduces the computational cost and improves the classification accuracy (Alslibi, et al., 2015; Alslibi, et al., 2017). Therefore, feature selection became a fundamental step in facial expression recognition systems for a better feature representation. In this stage, to further select the optimal set of discriminative facial features through the extracted feature space, firefly algorithm has been used. Here, the problem of feature selection is formulated as an optimization problem where the aim is to maximize the classification accuracy while minimizing the cardinality of the feature subset.

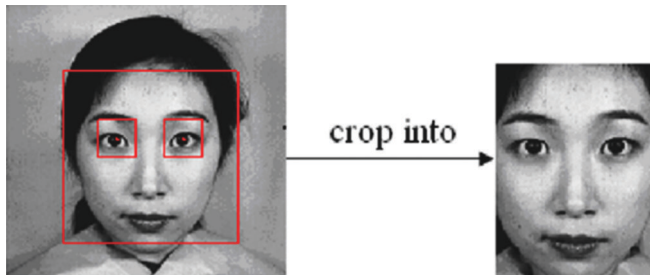


Fig. 2. (a and b) Face detection example

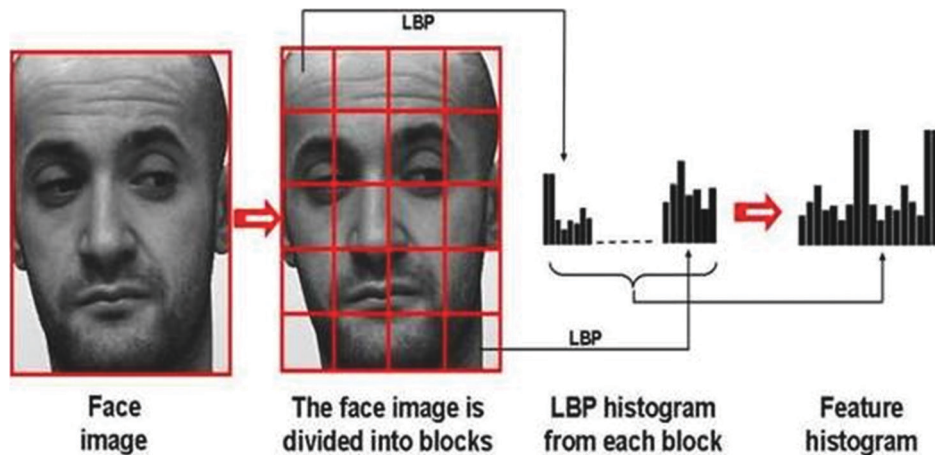


Fig. 3. Feature extraction example

f1	f2	f3	f4	f5	f6	f7	f8	f9	f10	...	fn
1	0	1	1	1	0	0	1	1	0	...	0

Fig. 4. FA-GD solution structure

Feature selection in this research is a process in which the system will try to minimize the number of features extracted by uLBP by finding the most relevant and important features from the faces as well as eliminating redundant features that could reduce the recognition accuracy which is like noisy features in the dataset to achieve better recognition accuracy. In this research, a bioinspired binary search algorithm called FA-GD is used to select features of all images which were extracted by uLBP to reach better accuracy.

FA-GD feature selection process

The first step in the feature selection process is to prepare the FA-GD algorithm by initializing the required parameters, those parameters can be initialized by defining:

1. Number of generations that the firefly algorithm will generate after applying the movement function.
2. Number of fireflies in each generation.
3. The initial value of attractiveness, light intensity, and randomization parameters.

Next, the FA-GD algorithm starts to randomly generate the initial generation of fireflies by creating a sequence of binary codes with length 2478 for each firefly as a vector. In this vector, the bits with value one represent that the particular features are being selected for training and testing, whereas, the bits with value (0) represent that those features will be dropped and not included in the training and testing process. Fig. 4 shows an illustrative example of the binary encoding structure of the firefly. Each firefly in the initial population will be evaluated by applying a 10-k cross-validation using k-nearest neighbors algorithm (k-NN) to obtain the accuracy of each firefly, where the accuracy of each firefly typically represents the fitness value of each firefly individually.

However, this process can be done by rebuilding the dataset which was generated from the feature extraction

process by removing all the features from the dataset in which the firefly have the binary value of 0, and keeping all the features in the dataset in which the firefly have the binary value of 1. For example, if the firefly has the binary value of 0 at index 50, this means that all the features in index 50 in the whole dataset will be removed. Thus, the new generated dataset will have the same number of instances as the original dataset, but it will have a different number of features depending on the number of binary 1 and binary 0 in the firefly chromosome. For instance, if the firefly chromosome has 1000 binary (1) values, then the new rebuilt dataset will have the dimensions of 213×1000 , where 213 is the number of instances and 1000 is the number of features which represent the firefly. This process will be applied for all fireflies individually before evaluation, so each firefly will have a different dataset structure depending on number and position of binary 0 and binary 1 in each firefly. Fig. 5 shows an illustrative example of rebuilding a new dataset for each firefly in the initial generation.

After evaluating all fireflies in the initial generation, the algorithm will find the best firefly that achieved the best accuracy and stores it as the global best, and then the algorithm will apply the movement as in 4 for all fireflies in the generation to create a new generation. As a result of applying the movement equation to each firefly, the new firefly may contain invalid values as a real number with decimal point, to fix this problem, a logistic sigmoid transformation function (Rathipriya, et al., 2011) is applied to all values in the firefly to fix the values and set it to be binary 0 or binary 1. By applying this transfer process to all fireflies after their movement, the new generation of fireflies is ready to be evaluated and continue with the typical evolution process of firefly algorithm.

D. Classification stage

The fourth phase of the proposed expression recognition model is the classification phase. As mentioned previously, in feature extraction, one feature vector is extracted from each face image. Next, relevant and important features are selected. Then, all the feature vectors are fed to the classifier. In this paper, K-nearest neighbor (k-NN) has been used to

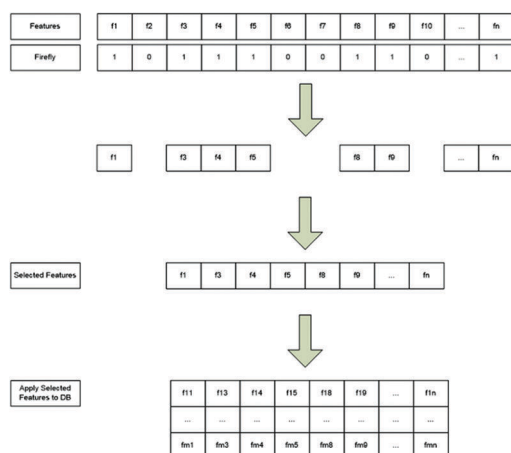


Fig. 5. Sample of building a new dataset based on selected features

classify the emotions for recognition. K-NN is a simple, fast method and it shows a good recognition results in other face and expression recognition systems as documented in the literature. The method will be used as a fitness function in the feature selection process, where the accuracy result will be the fitness value in training. Furthermore, it will be used as a classification for testing. The Euclidean distance as shown in 9 has been used as measure function in k-NN classification to calculate the distance between the features. K-NN algorithm works by calculating the minimum distance from the query instance to the training samples to determine the K-nearest neighbors. After gathering the K-nearest neighbors, a simple majority of these K-nearest neighbors are taking to be the prediction of the query instance.

$$(p,q)=\sqrt{(p_1-q_1)^2+(p_2-q_2)^2+\dots+(p_n-q_n)^2} \quad (9)$$

IV. EXPERIMENTAL RESULTS AND DISCUSSION

This section demonstrates the experimental evaluation of the proposed approach and its impact on improving the overall performance of the proposed recognition model. Basically, one of the databases that researchers often use for facial expression recognition is the JAFFE database (Lanitis, et al., 1995). This database contains 213 frontal facials images corresponding to 10 Japanese females with 7 different expressions (Happy, sad, angry, disgust, surprised, natural, and fear). The size of each image in the database is 256×256 pixels, all available in grayscale. Fig. 6 shows a sample of four female subjects from the JAFFE database. The proposed facial expression recognition system is coded in MATLAB 2015 under Windows OS platform on an Intel Core i7 2.4GHz processor with 8GB of RAM.

In all the experiments, the proposed firefly algorithm has an adaptive parameter control strategy based on Chaos maps. To demonstrate the effect of the number of fireflies on the performance of the system, the maximum number of generations is fixed, and the number of fireflies is varied from 10 to 50. Along similar lines, to investigate the effect of varying the number of generations on the performance of the system, the number of fireflies is fixed, and the maximum number of generations is varied from 25 to 100 as will be shown in the following experiments. Note that in all experiments, 10-k fold cross validation has been performed for classification. In the first set of experiments, the effect of the number of fireflies, number of generations, and number of GD iterations has been investigated. In the next experiment, the classical firefly algorithm will be compared with the improved firefly (GD-FA) in a statistical sense to prove that the proposed firefly algorithm significantly outperforms the conventional firefly in the feature selection task. Thereafter, the convergence behavior trends and computational time of both algorithms have been shown. Finally, the proposed facial expression system will be compared with other state-of-the-art approaches using the JAFFE dataset.

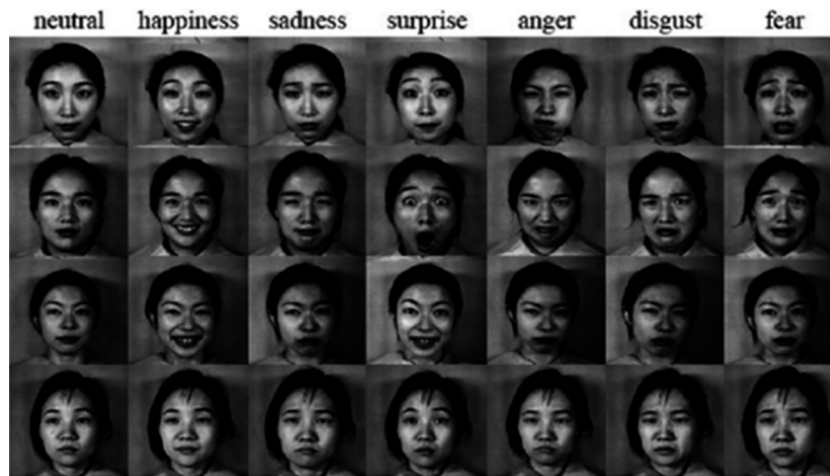


Fig. 6. Sample images from Japanese Female Facial Expression database

A. A. EFFECT OF THE NUMBER OF FIREFLIES

Basically, varying the number of fireflies in the initial population plays a significant impact on the performance of the firefly algorithm. Hence, in this experiment, to demonstrate the effect of the number of fireflies on the classification accuracy of the facial expression recognition system, the number of generations will be fixed. For each generation number from 25 to 150, the number of fireflies will be varied from 10 to 50 fireflies. The mean accuracy, best accuracy, standard deviation, and number of selected features will be reported for each combination of those parameters.

The results of this experiment are tabulated in Table I, where best results are shown in bold font. From the results shown in Table I, it can be seen that the best result has been obtained when using 50 fireflies and 150 generations where classification accuracy of 94.923% has been yielded. Furthermore, the number of selected features was 1254, which is sufficient to get good classification accuracy. Note that the original number of features was 2478 and reduced to about 50% when using the feature selection phase.

B. B. Effect of the number of GD iterations

In this experiment, to figure out the optimal value of the GD iteration, it will be varied from 10 to 50 iterations while fixing the number of fireflies and the number of firefly generations. The standard deviation, mean, and best accuracy, as well as the number of selected features, are reported. Note that, the number of selected features indicates the subset of features that have been selected by FA-GD at the end of iterations. From Table II, it can be seen that the maximum mean accuracy (96.2%) has been obtained when using 50 generations, 50 fireflies, and 20 GD iterations. Furthermore, when the number of fireflies is small (Dueck, 1993), the accuracy cannot be improved due to the lack of exploration.

C. C. Performance and convergence analysis

Convergence is an important metric for meta-heuristic optimization algorithms to indicate how fast the algorithm can reach to the optimum solution. The convergence metric

TABLE I

MEAN, BEST ACCURACY, SD, AND NUMBER OF THE SELECTED FEATURES FOR THE FA-GD ALGORITHM ON JAPANESE FEMALE FACIAL EXPRESSION

Gen. No.	No. Firefly	Mean	Best	SD	Selected feature
25	10	92.394	93.427	0.577	1262
	20	93.239	94.366	0.63	1233
	30	93.568	94.366	0.544	1218
	40	93.944	94.836	0.562	1235
	50	94.131	95.305	0.507	1266
50	10	93.380	94.366	0.643	1275
	20	93.615	93.897	0.328	1237
	30	94.131	94.836	0.456	1244
	40	94.366	95.305	0.495	1251
	50	94.319	94.836	0.604	1225
100	10	93.568	94.366	0.445	1206
	20	93.850	94.836	0.562	1217
	30	94.695	95.305	0.317	1260
	40	94.923	95.775	0.604	1266
	50	94.789	95.305	0.267	1246
150	10	94.923	94.366	0.411	1239
	20	94.319	94.836	0.267	1234
	30	94.695	95.305	0.387	1275
	40	94.742	95.305	0.431	1235
	50	94.923	95.775	0.373	1254

SD=standard deviations

is usually used to investigate whether the optimization algorithm can achieve and maintain a proper balance between exploration and exploitation during the search process so that it can avoid being stuck in local optima. As can be depicted from Fig. 7, the firefly algorithm suffers from the premature convergence problem as it gets stuck in local optima at generation 40. From generation 40 to 150, the algorithm cannot get out from the local optimum value. In this experiment, the average accuracy reported was 93.4%, where the accuracy of each facial expression is shown in Table III.

As can be deduced from Table III, the facial expression model shows good performance in detecting the natural, anger, disgust, and surprise expressions. However, lower performance has been reported for the fear and sad expressions where classification accuracy of 90.6% and 77.4% has been reported, respectively.

TABLE II
MEAN, BEST ACCURACY, SD, AND NUMBER OF THE SELECTED FEATURES FOR THE FA-GD

No. FA generations	No. firefly	No. GD iterations	Mean	Best	SD	Selected features
25	10	10	94.178	94.836	0.396	1246
		20	94.225	94.836	0.387	1229
		30	94.225	95.305	0.736	1251
		40	94.648	95.305	0.594	1208
		50	94.085	94.836	0.505	1254
	20	10	94.554	95.305	0.396	1242
		20	94.883	96.244	0.643	1255
		30	94.836	95.775	0.495	1297
		40	95.164	95.775	0.445	1205
		50	94.883	95.775	0.467	1204
	30	10	94.742	95.775	0.431	1229
		20	95.305	95.775	0.383	1247
		30	95.070	95.775	0.332	1242
		40	95.258	96.244	0.467	1266
		50	95.681	96.714	0.577	1253
40	10	94.930	95.775	0.533	1270	
	20	95.540	95.775	0.247	1254	
	30	95.305	95.775	0.221	1235	
	40	95.493	96.244	0.454	1265	
	50	95.587	96.244	0.396	1262	
50	10	95.211	95.775	0.431	1268	
	20	95.446	95.775	0.544	1239	
	30	95.258	95.775	0.346	1247	
	40	95.587	96.244	0.396	1227	
	50	95.681	96.714	0.533	1232	
50	10	10	94.131	94.366	0.332	1260
		20	94.507	95.305	0.588	1277
		30	94.554	95.305	0.396	1243
		40	94.836	95.305	0.313	1245
		50	94.883	95.305	0.346	1245
	20	10	94.883	95.775	0.517	1226
		20	95.493	96.224	0.551	1249
		30	95.352	96.244	0.517	1203
		40	95.493	96.244	0.454	1276
		50	95.352	96.244	0.467	1217
	30	10	95.857	95.775	0.328	1261
		20	95.493	95.775	0.328	1255
		30	95.399	96.244	0.370	1231
		40	95.775	95.775	0.242	1236
		50	95.493	95.775	0.242	1232
40	10	95.455	96.242	0.387	1233	
	20	95.631	96.712	0.497	1245	
	30	95.871	96.712	0.370	1236	
	40	95.771	96.242	0.383	1233	
	50	95.921	96.712	0.445	1244	
50	10	95.777	96.712	0.495	1239	
	20	96.200	96.71	0.411	1231	
	30	95.966	96.711	0.454	1239	
	40	95.922	96.711	0.445	1232	
	50	95.963	96.711	0.396	1234	

SD=standard deviations

In what follows, the same experimental procedure has been applied to the improved firefly algorithm to evaluate its performance and convergence trend. The convergence behavior and the confusion matrix of the improved firefly algorithm when using 20 fireflies and 50 generations are shown in Fig. 8 and Table IV, respectively. An average classification accuracy of 95.4% has been reported.

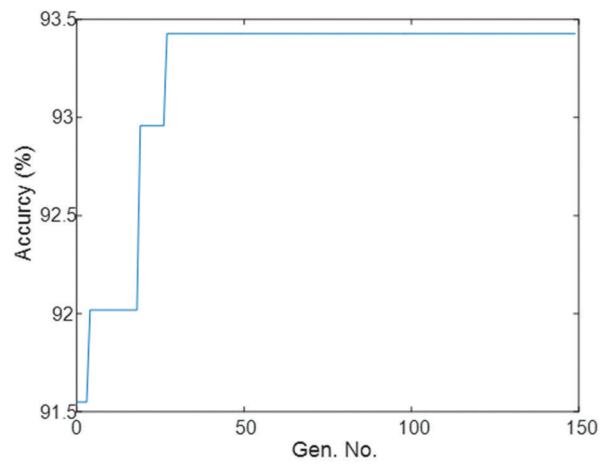


Fig. 7. Convergence behavior of the firefly algorithm during the first 150 generations and using 20 fireflies algorithm on Japanese female facial expression

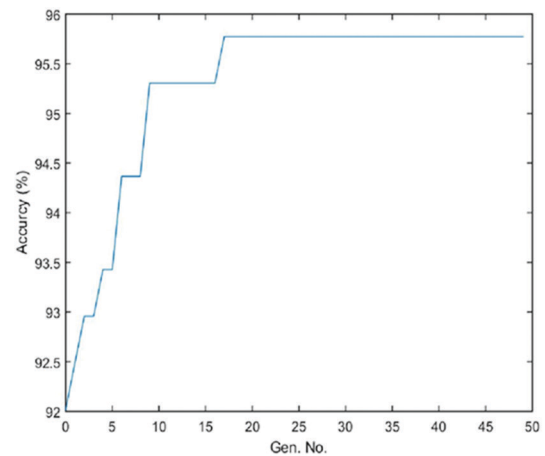


Fig. 8. Convergence behavior of FA-GD algorithm using 20 fireflies

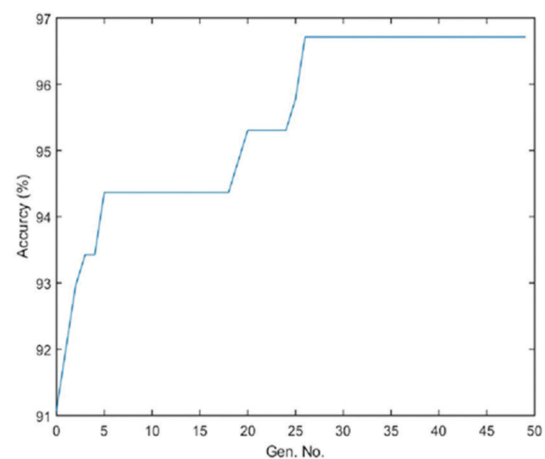


Fig. 9. Convergence behavior of the FA-GD algorithm using 50 fireflies

The convergence behavior trend and the confusion matrix of the improved firefly algorithm when using 50 fireflies and 50 generations are shown in Fig. 9 and Table V, respectively.

An average classification accuracy of 96.7% has been reported. The obtained results show that the performance and

convergence behavior of the improved firefly algorithm is better than the classical firefly algorithm. The incorporation of the Great Deluge algorithm helps in enhancing the exploitation ability of the firefly algorithm and achieving a better balance between exploration and exploitation and hence preventing the premature convergence problem.

TABLE III
CONFUSION MATRIX USING THE K-NN CLASSIFIER (150 GENERATIONS AND 10 FIREFLIES)

	Anger	Disgust	Fear	Happy	Natural	Sad	Surprise
Anger	96.67	0	0	0	0	0	0
Disgust	0	96.55	3.13	0	0	3.23	0
Fear	0	3.45	90.63	0	0	6.45	0
Happy	0	0	0	96.77	0	3.23	0
Neutral	0	0	3.13	3.23	100	9.68	0
Sad	3.33	0	3.13	0	0	77.42	0
Surprise	0	0	0	0	0	0	96.67s

TABLE IV
CONFUSION MATRIX OF THE FA-GD ALGORITHM (50 GENERATIONS AND 20 FIREFLIES)

	Anger	Disgust	Fear	Happy	Natural	Sad	Surprise
Anger	96.67	0	0	0	0	0	0
Disgust	0	96.55	3.13	0	0	3.23	3.33
Fear	0	0	93.75	0	0	3.23	0
Happy	0	0	0	93.55	0	3.23	0
Natural	3.33	0	0	0	100	9.68	0
Sad	0	3.45	3.13	6.45	0	80.65	0
Surprise	0	0	0	0	0	0	100

TABLE V
CONFUSION MATRIX USING THE IMPROVED FIREFLY ALGORITHM, (50 GENERATIONS AND 50 FIREFLIES)

	Anger	Disgust	Fear	Happy	Natural	Sad	Surprise
Anger	100	0	0	0	0	0	0
Disgust	0	96.55	3.13	0	0	3.23	0
Fear	0	0	93.75	0	0	3.23	3.33
Happy	0	0	0	90.32	0	3.23	0
Natural	0	0	0	3.23	100	3.23	0
Sad	0	3.45	3.13	6.45	0	87.10	0
Surprise	0	0	0	0	0	0	96.67

TABLE VI
KEYS TO COMPARATIVE APPROACHES ON THE JAPANESE FEMALE FACIAL EXPRESSION DATABASE

Key	Method	Evaluation procedure	Reference
DKLLE	Discriminant kernel locally linear embedding	10-fold cross-validation	(Zhao and Zhang, 2012)
LLE	Locally linear embedding		(Zhao and Zhang, 2012)
LDA	Linear discriminant analysis		(Belhumeur, et al., 1996)
PCA	Principle component analysis		(Turk and Pentland, 1991)
P-LBP	Patch-based LBP		(Happy and Routray, 2015)
Gabor-SRC	Gabor feature and SRC Classifier		(Lu, et al., 2015)
SVM-FA	SVM based improved FA		(Mistry, et al., 2017)

TABLE VII
THE BEST ACCURACY (STD) OF DIFFERENT STATE-OF-THE-ART METHODS ON THE JAPANESE FEMALE FACIAL EXPRESSION

Method	LDA	PCA	LLE	SLLE	DKLLE	P-LBP	Gabor-SRC	SVM-FA	Proposed (firefly)	Proposed (FA-GD)
Dimension	6	20	80	30	40	2478	2560	50-65	1242	1230
Accuracy (%)	80.81±3.6	78.09±4.2	75.57±3.8	78.57±4.0	84.06±3.8	91.8	97.68	87.75	94.8±0.75	96.7±0.54

D. Comparative evaluation with the state-of-the-art studies

In this section, the proposed facial expression recognition system will be compared with state-of-the-art methods that adopted similar protocols using the JAFFE database. To establish a fair comparison with the previous studies, the same experimental procedure has been used where a 10-fold cross validation has been considered. The performance of the proposed approach is compared with recent state-of-the-art benchmark methods as listed in Table VI. The best results and the standard deviations (SD) for different methods with the corresponding reduced dimension are listed in Table VII. From the results in Table VII, it can be seen that the proposed approaches outperformed most of the compared methods, except for the Gabor-SRC method. However, the number of features used in Gabor-SRC approach is approximately twice the number of features in our proposed approach.

V. CONCLUSION

This paper proposed an efficient mechanism to improve the recognition accuracy of facial expression recognition systems. First, uLBP features were extracted from face images. Second, to further enhance the feature descriptor, an enhanced version of firefly algorithm, called FA-GD was proposed to select the most discriminative and robust facial features. As the dimensionality of the extracted features is relatively high, FA-GD has been used to select the optimal set of facial features and eliminate redundant and noisy features to boost the recognition performance and speed up the computations. Several experimental evaluations have been carried out using the JAFFE database. Results show that the proposed approach yielded good classification accuracy compared to other state-of-the-art methods. The best classification accuracy obtained by the proposed method is 96.7% with 1230 selected features, whereas, Gabor-SRC method achieved 97.6% with 2560 features.

VI. ACKNOWLEDGMENT

The researchers wish to thank Universiti Kebangsaan Malaysia, for supporting this work by research grant DIP-2016-018.

REFERENCES

- Alslibi, B., Venkat, I., Subramanian, K., Lutfi, S.L. and Wilde, P.D., 2015. The impact of bio-inspired approaches toward the advancement of face recognition. *ACM Computing Surveys (CSUR)*, 48(1), p. 5.
- Alslibi, B., Venkat, I. and Al-Betar, M.A., 2017. A membrane-inspired bat algorithm to recognize faces in unconstrained scenarios. *Engineering Applications of Artificial Intelligence*, 64, pp.242-260.
- Bereta, M., Pedrycz, W. and Reformat, M., 2013. Local descriptors and similarity measures for frontal face recognition: A comparative analysis. *Journal of Visual Communication and Image Representation*, 24(8), pp.1213-1231.
- Belhumeur, P.N., Hespanha, J.P. and Kriegman, D.J., 1996. Eigenfaces vs. Fisherfaces: Recognition using Class Specific Linear Projection. *In: European Conference on Computer Vision*. Springer, Berlin, Heidelberg, pp.43-58.
- Dueck, G., 1993. New optimization heuristics: The great deluge algorithm and the record-to-record travel. *Journal of Computational Physics*, 104(1), pp.86-92.
- Happy, S.L. and Routray, A., 2015. Robust Facial Expression Classification using Shape and Appearance Features. *In Advances in Pattern Recognition (ICAPR), 2015 Eighth International Conference on*. IEEE, pp.1-5.
- Hamid, A.A.K.A. and Nordin, M.J., 2016. Radius based block LBP for facial expression recognition. *international information institute (Tokyo). Information*, 19(9B), p. 4197.
- He, L. and Huang, S., 2017. Modified firefly algorithm based multilevel thresholding for color image segmentation. *Neurocomputing*, 240, pp.152-174.
- Jamshidnezhad, A. and Nordin, M.J., 2013. Bee royalty offspring algorithm for improvement of facial expressions classification model. *International Journal of Bio-Inspired Computation*, 5(3), pp.175-191.
- Khatri, N.N., Shah, Z.H. and Patel, S.A., 2014. Facial expression recognition: A survey. *International Journal of Computer Science and Information Technologies (IJCSIT)*, 5(1), pp.149-152.
- Lanitis, A., Taylor, C.J. and Cootes, T.F., 1995. Automatic face identification system using flexible appearance models. *Image and Vision Computing*, 13(5), pp.393-401.
- Lu, X., Kong, L., Liu, M. and Zhang, X., 2015. Facial expression recognition based on gabor feature and SRC. *In: Chinese Conference on Biometric Recognition*. Springer, Cham, pp.416-422.
- Mistry, K., Zhang, L., Sexton, G., Zeng, Y. and He, M., 2017. Facial expression recognition using firefly-based feature optimization, *2017 IEEE Congress on Evolutionary Computation (CEC)*, San Sebastian, pp.1652-1658.
- Ojala, T., Pietikainen, M. and Maenpaa, T., 2002. Multiresolution gray-scale and rotation invariant texture classification with local binary patterns. *IEEE Transactions on Pattern Analysis and Machine Intelligence*, 24(7), pp.971-987.
- Palit, S., Sinha, S.N., Molla, M.A., Khanra, A. and Kule, M. 2011. *A Cryptanalytic Attack on the Knapsack Cryptosystem using Binary Firefly Algorithm*. Vol. 2. International Conference on Computer and Communication Technology (ICCCCT), pp.428-432.
- Rathipriya, R., Thangavel, K. and Bagyamani, J., 2011. Binary particle swarm optimization based biclustering of web usage data. *arXiv preprint arXiv:1108.0748*. *International Journal of Computer Applications*, 25, pp. 975-8887.
- Tilahun, S.L. and Ngnotchouye, J.M.T., 2017. Firefly algorithm for discrete optimization problems: A survey. *KSCE Journal of Civil Engineering*, 21(2), pp.535-545.
- Tilahun, S.L., Ngnotchouye, J.M.T. and Hamadneh, N.N., 2017. Continuous versions of firefly algorithm: A review. *Artificial Intelligence Review*, 2017, pp.1-48.
- Tilahun, S.L. and Ong, H.C., 2012. Modified firefly algorithm. *Journal of Applied Mathematics*, 2012, pp.12.
- Turk, M. and Pentland, A., 1991. Eigenfaces for recognition. *Journal of Cognitive Neuroscience*, 3(1), pp.71-86.
- Wang, H., Zhou, X., Sun, H., Yu, X., Zhao, J., Zhang, H. and Cui, L., 2017b. Firefly algorithm with adaptive control parameters. *Soft Computing*, 21(17), pp.5091-5102.
- Yang, X.S., 2010, Firefly algorithms for multimodal optimization. *In: International Symposium on Stochastic Algorithms*. Springer, Berlin, Heidelberg, pp.169-178.
- Zhao, X. and Zhang, S., 2012. Facial expression recognition using local binary patterns and discriminant kernel locally linear embedding. *EURASIP Journal on Advances in Signal Processing*, 2012(1), p. 20.

Synthesis and Characterization of Iron^{II}, Cobalt^{II}, Nickel^{II}, Copper^{II}, and Zinc^{II} Complexes Using Diphenylmethyl Xanthate Ligand

Aeed S. Al-Fahdawi¹ and Eman I. Alsalihi²

¹Department of Chemistry, College of Education for Women, University of Anbar, Ramadi, Anbar - F.R. Iraq

²Department of Chemistry, Faculty of Science and Health, Koya University, Kurdistan Region - F.R. Iraq

Abstract—Potassium diphenylmethyl xanthate and its monomeric complexes were synthesized at room temperature under inert gas and stirring condition. The ligand and its complexes of the general formula [M(L)₂] (where, M = Fe^{II}, Co^{II}, Ni^{II}, Cu^{II}, Zn^{II}, and Cd^{II}) were characterized by spectroscopic methods (IR, UV-Vis, ¹H-, ¹³C-, DEPT-, HMQC-, and COSY-NMR), elemental analysis, metal content, magnetic susceptibility measurement, and molar conductance. These studies revealed the formation of four-coordinate complexes.

Index Terms—Four-coordinate complexes, Potassium diphenylmethyl xanthate ligand, Structural study, Xanthate complexes.

I. INTRODUCTION

Xanthates are an important class of organic species that have shown a range of applications have attracted chemists. This based on their industry applications, analytical, and coordination chemistry. They have been used in industry as flotation agents for nonferrous metal sulfide ore (Coucouvani, 1979; Rao, 1971). Further, their role as additives lubricating oils is well documented (Rao, 1971). Based on their coordination behavior, xanthates as reagents have been used in analytical determination and separation of a large numbers of metal ions (Exarchos, et al., 2001; Cox, et al., 1996; and Vastag, et al., 1990). Some of xanthates species and their metal complexes are used as pharmaceuticals for HIV infections. Furthermore, xanthate-based gold^(I) complexes have played a key role in the design and fabrication of electronic and sensor devices. Recently, the preparation of monomeric five-coordinate Cu-xanthates adducts with pyridine derivatives have been

reported (Gurpreet, et al., 2013). The introduction of pyridyl moiety was to overcome the instability of the four-coordinate Cu-xanthates complexes (Kour, et al., 2013). In this paper, we describe the synthesis and physical characterization of potassium diphenylmethyl xanthate ligand and its monomeric metal complexes with some of divalent transition metal ions (Fe^{II}, Co^{II}, Ni^{II}, Cu^{II}, Zn^{II}, and Cd^{II}).

II. EXPERIMENTAL

A. Materials

Chemical reagents were commercially available and used without purification (Diphenyl Benzophenone - Sigma-Aldrich 99%, Sodium Borohydrate - Merck 99%, Potassium hydroxide - Sigma-Aldrich 85%, Carbon Disulfide - Aldrich 99%, Metal chloride salt - Fluka 98%, and Methanol - Sigma-Aldrich 99%).

B. Physical measurements

Elemental analyses (C, H, N, and S) were carried out on a Heraeus instrument (vario EL). Melting points were obtained by a Buchi SMP-20 capillary melting point apparatus. IR spectra were recorded as ATR uses a smart diamond ATR attachment on a Thermo-Nicolet Fourier transform-infrared (FTIR) spectrometer (AVATAR 320) in the range of 4000–500/cm, and as CsI discs using a Shimadzu 8300 FTIR spectrophotometer in the range of 600–300/cm. Electronic spectra were measured between 200 and 1000 nm with 10⁻³ M solutions in dimethylsulfoxide (DMSO) spectroscopic grade solvent at 25°C using a Perkin-Elmer spectrophotometer Lambda. NMR spectra (¹H, ¹³C, DEPT, ¹H-¹H COSY, and ¹³C-¹H HMQC NMR) were acquired in DMSO-d₆ solutions using a Jeol Lambda 400 MHz spectrometer with tetramethylsilane for ¹H NMR. Metals were determined using a Shimadzu (A.A) 680 G atomic absorption spectrophotometer. Conductivity measurements were made with DMSO solutions using a Jenway 4071 digital conductivity meter, and room temperature magnetic moments were measured with a magnetic susceptibility balance (Johnson Matthey Catalytic System Division).

ARO-The Scientific Journal of Koya University
Volume VI, No 1(2018), Article ID: ARO.10243, 5 pages
DOI: 10.14500/aro.10243

Received 11 May 2017; Accepted: 03 May 2018

Regular research paper: Published 25 May 2018

Corresponding author's e-mail: eman.ibraheem@koyauniversity.org
Copyright © 2018 Aeed S. Al-Fahdawi, Eman I. Alsalihi. This is an open-access article distributed under the Creative Commons Attribution License.



III. SYNTHESIS

A. Preparation of diphenylmethanol (Al-Fahdawi and Al-Salihi, 2015)

The ligand has prepared by dissolving (1 g, 5.51 mmol) of diphenyl benzophenone (1.0417 g, 27.55 mmol) of sodium borohydride with continues stirring in 50 ml of methanol for 1 h and then the mixture was treated with microwave for 3 min. The solvent was removed under reduced pressure and the residue was purified using unplat silica gel chromatography with eluent (9.5:0.5 dichloromethane/methanol) at $R_f=0.8$. Yield: 1.28 g, (98.1%), m.p. 63–64°C. IR (ATR cm^{-1}) characterization was as follows: 3270 $\nu(\text{O-H-O})$, 3084 $\nu_{\text{ar}}(\text{C-H})$, 1493 and 1454 $\nu_{\text{ar}}(\text{C=C})$. NMR data (ppm), δ_{H} (400 MHz, chloroform-D): 7.39–7.25 (m, 10H), 5.83 (s, 1H, OH), 2.35 (s, 1H, C-H); δ_{C} (100.63 MHz, CDCl_3): 76.07, 126.36, 127.47, 128.46, 144.25. X-ray crystallography shows H-atoms were placed in calculated positions [O1-C1=1.4348(16), O1-H1=0.91(2), 1.4348(16), O1B-C1B=1.4352(15), and O1B-H1B=0.923(19)] and were included in the refinement in the riding model approximation. The yield was 1.28 g (98.1%) of m.p. 63–64°C.

B. Preparation of xanthate salt

Xanthate salt was prepared by a conventional method (Seleem, et al., 2011) as in the following: To a suspension of finely powdered (1.1 g, 20 mmol), potassium hydroxide was dissolved in 20 ml of dioxane and a solution (10 mmol) of diphenylmethanol and (1.8 g, 24 mmol) of carbon disulfide in 10 ml of dioxane was add. The mixture was stirred overnight at room temperature, then 7 ml from diethyl ether was added, and the mixture was stirred for an additional 1 h. A pale-yellow solid was collected by filtration, washed with ether, and dried under vacuum. Yield: 1.28 g, (98.1%) of m.p.= 93–94°C, IR (ATR cm^{-1}) characterization was as follows: 3049 $\nu_{\text{ar}}(\text{C-H})$, 1618–1488 $\nu_{\text{ar}}(\text{C=C})$. NMR data (ppm), δ_{H} (400 MHz, Chloroform-Dme): 7.79–7.47 (m, 10H), 1.62 (s, 1H, C-H); δ_{C} (100.63 MHz, CDCl_3): 116.33, 128.29, 129.97, 132.40, 137.65, 196.40.

C. General synthesis of the complexes

A general method was used to obtain the required metallic xanthate complexes as follows:

Metal chloride salt (1 mmole) was dissolved in 10 ml of ethanol and mixed with methanolic solution of the potassium xanthate ligand (2 mmol) in methanol (15 mL). The mixture was allowed to stir overnight at room temperature, then distilled water was added for precipitating the product. The resulted solid was filtered off, washed by methanol, and dried at room temperature to give the required xanthate complex. Elemental analysis data, colors, and yields for the complexes are given in Table I.

IV. RESULTS AND DISCUSSION

Free xanthate ligand was obtained from the reaction of diphenyl methanol with carbon disulfide in alkaline medium (KOH). The general synthetic method involves the reaction

of some transition metals with alkali metal salt of the corresponding thioacid (exothermic behavior) as shown in Fig. 1.

Xanthate ligand complexes with Fe^{II} , Co^{II} , Ni^{II} , Cu^{II} , Zn^{II} , and Cd^{II} ions were obtained in a moderate yields. The compounds were characterized by ^1H - and ^{13}C -NMR, elemental analysis, IR, UV-Vis, magnetic susceptibility, and conductivity measurements. Diphenylmethanol compound was characterized by IR, thin-layer chromatography (TLC), X-RD powder, ^1H - and ^{13}C -NMR spectra, elemental analysis, and X-ray single crystal diffraction analysis (Al-Fahdawi and Al-Salihi, 2015) (see experimental section).

IR (ATR) spectrum of the ligand shows characteristic bands due to the $\nu(\text{O-H})$ and $\nu(\text{C=C})$ at 3270 cm^{-1} and (1493, 1454) cm^{-1} , respectively, as functional groups (Seleem, et al., 2011). ^1H -NMR spectrum for the ligand shows characteristic single peak at $\delta = 5.83$ ppm, which attributed to O-H protons. The spectrum displays single resonances at $\delta = 2.35$ ppm assigned to methanolic group (C-H). These signals in diphenylmethanol compound are appeared at down filed when they are attached withdrawing groups CS_2 to the xanthate salt (Srinivasan, et al., 2012). Whereas IR (ATR) spectrum bands of the xanthate salt ligand show bands at 1618–1488 cm^{-1} due to $\nu(\text{C=C})$ assigned to the aromatic groups, also the spectrum shows band at 1073 cm^{-1} due to $\nu(\text{C=S})$. The disappearance of $\nu(\text{O-H})$ band due to the replacement of the hydrogen atom by CS_2 . The ^1H -NMR spectrum for xanthate salt appears as expected downfield at $\delta = 1.62$ ppm due to (C-H) methanolic group and 7.79–7.49, which assigned to aromatic protons (Al-Fahdawi, et al., 2013). The absence of O-H group signal assigned that the CS_2 is in attach with oxygen atom. ^{13}C -NMR shows important peaks at CS_2 which detected at 196.40 ppm, which is disappeared in DEPT ^{13}C -NMR, because it is quaternary carbon (Al-Fahdawi, et al., 2014; Beer, et al., 2003). That is the metal directed to the desired xanthate complexes. These new complexes were characterized by many techniques such as ATR. The infrared spectra ATR show characteristic bands of ligand and its complexes as shown in Table II.

The important bands of these complexes are ranged about 1230 ± 15 cm^{-1} and 1050 ± 10 cm^{-1} which are due to the $\nu(\text{C-O-C})$ and $\nu(\text{C=S})$ for Fe^{II} , Co^{II} , Ni^{II} , Cu^{II} , Zn^{II} , and Cd^{II} metal ion complexes, respectively (Al-Fahdawi and Al-Salihi, 2015). After complexation, the frequency of $\nu(\text{C-}$

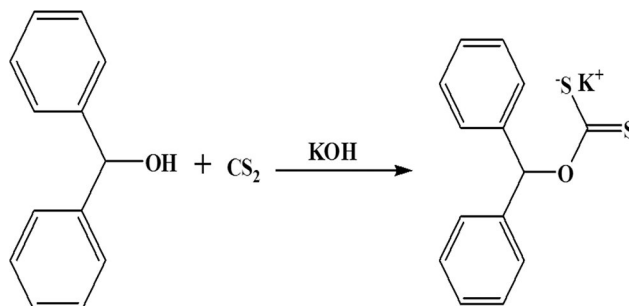


Fig. 1. The synthetic route for ligand and general structure for suggested complexes

TABLE I
 COLORS, YIELDS, MELTING POINTS, (M, C, H, S) ANALYSIS, AND MOLAR CONDUCTANCE VALUES COMPLEXES

Molecular formula	M.Wt	Weight of yield g	Yield%	Color	m.pc°	Found (calc%)				$\Sigma M(\Omega^{-1} \text{ cm}^2 \text{ mol}^{-1})$
						M	C	H	S	
$C_{24}H_{22}O_2S_4Fe$	526.37	0.107	54	Red	169–171	10.56 –10.54	63.8 –63.83	4.2 –4.17	24.35 –24.31	11.3
$C_{24}H_{22}O_2S_4Co$	528.99	0,086	43	Dark blue	232–234	11.14 –11.05	63.53 –63.51	4.19 –4.15	24.17 –24.19	18.8
$C_{24}H_{22}O_2S_4Ni$	529.21	0,126	63	Green	160–161	11.17 –11.09	63.52 –63.49	4.17 –4.15	24.21 –24.18	10.9
$C_{24}H_{22}O_2S_4Cu$	533.72	0.114	59	Dark green	135–137	12.38 –12.36	62.99 –62.95	4.13 –4.12	23.95 –23.98	16.2
$C_{24}H_{22}O_2S_4Zn$	535.91	0.083	41	White	151–152	12.27 –12.2	62.65 –62.69	4.16 –4.1	23.91 –23.88	13.5
$C_{24}H_{22}O_2S_4Cd$	582.93	0,114	52	White	193–195	19.25 –19.23	57.68 –57.63	3.8 –3.77	21.99 –21.95	17.8

 TABLE II
 FTIR BANDS FOR XANTHATE COMPLEXES

Compound	$\nu(X-O-X)$	$\nu(X-O)$	$\nu(X=\Sigma)$	$\nu(M-\Sigma)$
Xanthate	1235	1156	1073	
[Fe-Xanthate]	1223	1192	1032	370
[Co-Xanthate]	1237	1185	1038	360
[Ni-Xanthate]	1220	1191	1050	365
[Cu-Xanthate]	1233	1176	1068	350
[Zn-Xanthate]	1231	1181	1059	355
[Cd-Xanthate]	1240	1201	1061	360

FTIR=Fourier transform-infrared

O-C) and $\nu(C=S)$ bands was shifted to higher and lower frequencies, respectively, for Fe^{II} , Co^{II} , Ni^{II} , Cu^{II} , Zn^{II} , and Cd^{II} metal ion complexes indicating that the complexation was carried out through sulfur, which has been confirmed by the frequency of $\nu(M-S)$ $360 \pm 10 \text{ cm}^{-1}$ (Al-Fahdawi, et al., 2014; Beer, et al., 2003). The analytical data as shown in Table I agree with the suggested formulae $C_{14}H_{11}KOS_2$ (Fig. 1). Molar conductance of the complexes in DMSO solutions is indicative of their nonelectrolytic nature (Yu, et al., 2009). UV-Vis spectra of the Fe^{II} , Co^{II} , Ni^{II} , Cu^{II} , Zn^{II} , and Cd^{II} complexes exhibited different extents of red shift of bands related to the ligand field $\pi \rightarrow \pi^*$ and $n \rightarrow \pi^*$ transitions, bands in the range of 321–450 nm are related to the charge transfer transition (C.T) (Griffith, et al., 2011; Ma et al., 2011) (Table III).

Magnetic moment value of the Fe^{II} complex is in accordance of tetrahedral geometry (Aly, et al., 1985). This has been confirmed by its UV-Vis in DMSO, which displays band in the $d-d$ region at 626 nm, due to ${}^5T_2 \rightarrow {}^5E$, indicating a tetrahedral structure (Batten and Robson, 1998). The cocomplex displays additional bands in the $d-d$ region at 474 and 670 nm, related to ${}^4A_2^{(F)} \rightarrow {}^4T_2^{(F)}$ and ${}^4T_1^{(F)} \rightarrow {}^4T_2^{(F)}$, characteristic for tetrahedral geometry around Co^{II} atom (Aly, et al., 1985). Magnetic moment of this complex is typical for tetrahedral structure (Carlucci, et al., 2003). The spectrum of the Ni^{II} complex displays band in the $d-d$ region, which is characteristic of square planar complexes. The magnetic moment value of the Ni^{II} complex, as well as the other analytical data, is in agreement with its square planar

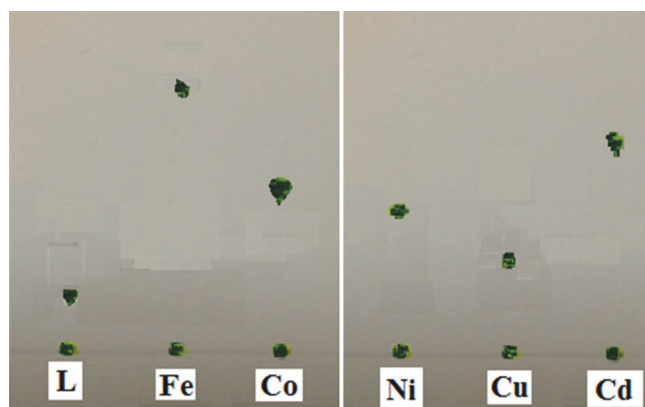


Fig. 2. The thin-layer chromatography measurements for the [L] Ligand and its Fe^{II} , Co^{II} , Ni^{II} , Cu^{II} , and Cd^{II} metal ion

structures (Batten, 2001; Zelenak and Gyoryov, 2002). The Cu^{II} complex exhibited electronic spectrum and magnetic moment confirming tetrahedral structure. The electronic spectra of the Zn^{II} and Cd^{II} complexes exhibited bands related to ligand field and ($L \rightarrow M$) charge transfer (Lever, 1984). These complexes are diamagnetic as expected (d^{10} system) and normally prefer tetrahedral coordination. TLC measurement for the derivative ligands [L] and its complexes were performed with Fe^{II} , Co^{II} , Ni^{II} , Cu^{II} , and Cd^{II} are showed in Fig. 2.

The appearance of new spots with different R_f of Fe^{II} , Co^{II} , Ni^{II} , Cu^{II} , and Cd^{II} indicated the formation of the complexes by comparison with the R_f of the ligand (Table IV).

X-ray powder diffraction (XRD) pattern of Co^{II} complex shows well-defined crystalline peaks indicating that the sample is 20% crystalline in nature (Dokken, et al., 2009), and the XRD powder diffraction pattern of copper complex has been given in Fig. 3.

In Fig. 3, The XRD of Co^{II} metal complex of different scale particles is well coincident with each other, and it means that different forms of complexes have the same structure (Guillemet-Fritsch, et al., 2006). The sample has been dried and then scanned in the 2θ range of 10–80° confirming four coordination around Co ion complex (Kavitha and Lakshm, 2017; Zheng, et al., 2017).

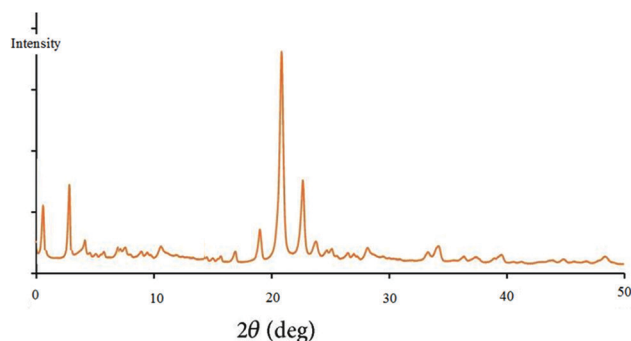
TABLE III
 UV-VIS MEASUREMENTS AND MAGNETIC MOMENT FOR XANTHATE COMPLEXES

Compound	Band	Wave number	ϵ_{\max}	Assignment	Magnetic moment (B.M)
	Position λ_{nm}	(cm^{-1})	($\text{dm}^{-1} \cdot \text{mol}^{-1} \cdot \text{cm}^{-1}$)		
[Xanthate]	261	38314	1680	$\pi \rightarrow \pi^*$	
	365	27395	36		
[Fe-Xanthate]	270	37037	983	Intra ligand	4.5
	315	31746	381	C.T	
	436	22936	283	C.T	
	626	15974	21	$^5T_2 \rightarrow ^5E$	
[Co-Xanthate]	257	38911	1339	$\pi \rightarrow \pi^*$	4.2
	474	21097	57	$^4A_2^{(F)} \rightarrow ^4T_1^{(P)}$	
	670	14925	18	$^4T_1^{(F)} \rightarrow ^4T_2^{(F)}$	
[Ni-Xanthate]	266	37594	880	$\pi \rightarrow \pi^*$	Diemagnetic
	450	22222	165	$^3A_2g \rightarrow ^1T_1g^{(P)}$	
	632	15823	47	$^3A_2g \rightarrow ^3T_1g^{(F)}$	
[Cu-Xanthate]	259	38616	1739	$\pi \rightarrow \pi^*$	1.6
	505	19802	300	$^2T_2 \rightarrow ^2E$	
[Zn-Xanthate]	263	38023	1127	$\pi \rightarrow \pi^*$	Diemagnetic
[Cd-Xanthate]	259	38616	1659	$\pi \rightarrow \pi^*$	Diemagnetic

TABLE IV

 THE TLC MEASUREMENTS FOR THE [L] LIGAND AND ITS Fe^{II} , Co^{II} , Ni^{II} , Cu^{II} , AND Cd^{II} COMPLEXES

Compound	Range of Rf (mm)
Xanthate	1.2
[Fe-Xanthate]	4.5
[Co-Xanthate]	3.1
[Ni-Xanthate]	2.4
[Cu-Xanthate]	1.7
[Cd-Xanthate]	4.0

Fig. 3. The X-ray powder diffraction of Co^{II} metal complex

V. CONCLUSION

In recent years, considerable attention has been devoted to the formation of stable four-coordinate xanthate complexes that consist with CS_2 group which have numerous important applications. The reaction of diphenyl methanol with CS_2 in alkaline solution gives the required xanthate ligand. It is observed from research data in this study existence of four-coordinated complexes with Fe^{II} , Co^{II} , Ni^{II} , Cu^{II} , Zn^{II} , and Cd^{II} metal ions.

REFERENCES

Al-Fahdawi, A.S. and Al-Salihi, I.I., 2015. Preparation of Tris (diphenyl methanol) binding by hydrogen bonds through the application of microwave.

techniques. *International Journal of Current Research in Biosciences and Plant Biology*, 2(7), pp.1-9.

Al-Fahdawi, A.S., Al-Kafajy, H.A., Al-Jeboori, M.J. and Potgieter, H., 2014. New bimetallic bisdithiocarbamate-based macrocyclic complex; Preparation and spectral characterization. *ChemXpress*, 4(3), pp.262-267.

Al-Fahdawi, A.S., Al-Kafajy, H.A., Al-Jeboori, M.J. and Potgieter, H., 2013. Synthesis, spectral and structural studies of neutral co(II), Ni(II) and Cu(II) macrocyclic dithiocarbamate- based complexes formed via one pot reaction. *Iraq National Journal of Chemistry*, 52, pp.414-429.

Aly, M.M., Baghlaif, A.O. and Ganji, N.S., 1985. Linkage isomerism of the oximate group: The characterization of some mono- and binuclear square planar nickel(II) complexes of vicinal oxime-imine ligands. *Polyhedron*, 4, pp.1301.

Batten, S.R. and Robson, R., 1998. Interpenetrating nets: Ordered, periodic entanglement. *Angewandte Chemie International Edition*, 37, pp.1460-1494.

Batten, S.R., 2001. Topology of interpenetration. *Cryst Eng Comm*, 22, pp.67-72.

Beer, P.D., Cowley, A.R., Jeffery, J.C., Paul, R.L. and Wong, W.W. H., 2003. Self-assembled xanthate-transition metal polyether macrocycles and cryptands. *Polyhedron*, 22(5), pp.795-801.

Carlucci, L., Ciani, G. and Proserpio, D.M., 2003. Polycatenation, polythreading and polyknitting in coordination network chemistry. *Coordination Chemistry Reviews*, 246, pp.246-247.

Coucouvanis, D., 1979. *Progress in Inorganic Chemistry*. Vol. 26. John Wiley, New York. pp.302.

Cox, M.J. and Tiekink, E.R.T. 1996. Syntheses and characterization of aryl xanthates of group 12th elements. *Kristallog*, 211, 111-113.

Dokken, K.M., Parsons, J.G., McClure, J. and Gardea-Torresdey, J.L., 2009. Synthesis and structural analysis of copper(II) cysteine complexes. *Inorganica Chimica Acta*, 362, pp.395-401.

Exarchos, G., Robinson, S. and Steed, J., 2001. Should solid-state molecular packing have to obey the rules of crystallographic symmetry. *Polyhedron*, 20, pp.2951.

Griffith, D.M., Szocs, B., Keogh, T., Suponitsky, K.Y., Farkas, E., Buglyo, P. and Marmion, C.J., 2011. Suberoylanilide hydroxamic acid, a potent histone deacetylase inhibitor: Its X-ray crystal structure and solid state and solution studies of its Zn(II), Ni(II), Cu(II) and Fe(III) complexes. *Journal of Inorganic Biochemistry*, 105, pp.763-769.

- Guillemet-Fritsch, S., Lebey, T., Boulos, M. and Durand, B., 2006. Dielectric properties of CaCu₃Ti₄O₁₂ based multiphased ceramics. *Journal of the European Ceramic Society*, 26, pp.1245-1257.
- Gurpreet, K., Inderjeet, K. and Renu, S., 2013. Synthesis and characterization of the adducts of bis(O-ethylthiocarbonato)copper(II) with substituted pyridines. *International Journal of Inorganic Chemistry*, 2013, pp.502856.
- Kavitha, N. and Lakshmi, P.V.A., 2017. Synthesis, characterization and thermogravimetric analysis of Co(II), Ni(II), Cu(II) and Zn(II) complexes supported by ONNO tetradentate Schiff base ligand derived from hydrazine benzoxazine. *Journal of Saudi Chemical Society*, 21, pp.S457-S466.
- Kour, G. Kour, I. and Sachar, R. 2013. Synthesis and characterization of the adducts of bis(O-ethylthiocarbonato)copper(II) with substituted pyridines. *International Journal of Inorganic Chemistry*, 2013, pp.502856.
- Lever, A.B.P., 1984. *Inorganic Electronic Spectroscopy*. Elsevier Publishing, New York.
- Ma, Q., Zhu, M., Lu, L., Feng, S. and Ya, J., 2011. Preparation of molecularly imprinted polymer and its recognition property for salvianolic acid A. *Chimica Acta*, 370, pp.102-107.
- Rao, S.R., 1971. *Xanthates and related compounds*. Marcel Dekker, New York.
- Seleem, H.S., El-Inany, G.A., El-Shetary, B.A. and Mousa, M.A., 2011. The ligational behavior of a phenolic quinolyl hydrazone towards copper (II)-ions. *Chemistry Central Journal*, 5, pp.2.
- Srinivasan, S., Ramalingam, K. and Rizzoli, C., 2012. Synthesis, NMR and single crystal X-ray structural studies on planar NiS₄ and NiS₂PN chromophores: Steric and electronic effects. *Polyhedron*, 33, pp.60-66.
- Vastag, S., Marko, L., Rheingold, A.L.J. 1990. Pentacoordinate cobalt(III) thiolate and nitrosyl tropocoronand compounds. *Organometallic Chemistry*, 397, pp.231.
- Yu, K., Gu, Z., Ji, R. and Lou, L.S., 2009. Mild oxidation of alkanes and toluene by tert-butylhydroperoxide catalyzed by an homogeneous and immobilized Mn(salen) complex. *Tetrahedron*, 65, pp.305-311.
- Zelenak, V. and Gyoryov, K.D., 2002. Correlation of infrared spectra of zinc (II) carboxylates with their structures. *Spectrochim Acta*, 8, pp.269.
- Zheng, Z., Junwei, X., Sisi, Y., Yangli, C., Yan, W., Zhuo, C. and Chunlin, N., 2017. Two organic cation salts containing tetra(isothiocyanate)cobaltate(II): Synthesis, crystal structures, spectroscopic, optical and magnetic properties. *Crystals*, 7, pp.92.

Synthesis and Antibacterial Activity of Isatin Schiff Base Derivative with 3-Aminoacetophenone and its Ni^{II}, Co^{II} Transition Metals Complexes

Eman I. Alsalihi¹ and Aeed S. Al-Fahdawi²

¹Department of Chemistry, Faculty of Science and Health, Koya University, Kurdistan Region – F.R. Iraq

²Department of Chemistry, College of Education for Women, University of Anbar, Ramadi, Anbar – F.R. Iraq

Abstract—The (E)-3-(3-acetylphenylimino) indolin-2-one (Bidentate) ligand type [HL] has been prepared from Isatin and 3-aminoacetophenone in the presence of KOH. In general, the ligand contains oxygen (O) and nitrogen (N) donor atoms. The reaction of Isatin and 3-aminoacetophenone was carried out in ethanol by condensation reaction at 80°C with reflux for 4 h, to form [HL] ligand type. This ligand has been used to prepare Ni^{II} and Co^{II} complexes in the ratio of 1:1 metal-ligand. All compounds have been characterized by spectroscopic methods (Fourier transform infrared and ultraviolet-visible), C.H.N, thin-layer chromatography, mass spectrum, X-ray diffraction, magnetic moment, conductivity measurements and melting point, the synthesized ligand and its metal complexes have been tested for their antibacterial activity against *Staphylococcus aureus* and *Bacillus subtilis* using agar disc diffusion method. The ligand and its complexes showed significant activities against *S. aureus* and *B. subtilis*. Our study revealed the formation of four coordinate square planar complexes around Ni^{II} and Co^{II} metal ions.

Index Terms—3-aminoacetophenone, Bidentate ligand and (N) donor atoms, Isatin, Schiff base.

I. INTRODUCTION

Schiff bases have played an important role in the development of coordination chemistry as they readily form stable complexes with most of the transition metals. The chemistry of Schiff base ligands species has been gaining considerable interest primarily because of their fascinating structural diversities (Asadi, et al., 2011; Monfared, et al., 2011; Chamayou, et al., 2011). The electrophilic carbon atoms of aldehydes and ketones can be targets of nucleophilic attack by amines. The end result of this reaction is a compound in which the C=O double bond is replaced by a C=N double bond. This type of compound is known as an imines, or Schiff base with the general formula R₁R₂C=NR₃,

where R is an organic side chain. In this definition, Schiff base is synonymous with azomethine. Many Schiff base complexes show excellent catalytic activity in various reactions and in the presence of moisture (Abu-Dief Ahmed and Mohamed Ibrahim, 2015). The Schiff bases are widely used for industrial purposes and also exhibit a broad range of biological activities. This short review compiles examples of the most promising antimalarial, antibacterial, antifungal, and antiviral Schiff bases. An overview of synthetic methodologies used for the preparation of Schiff bases is also described (Da Silva Cleiton, et al., 2011). Isatin is a yellowish red crystalline compound soluble in hot water, used for the preparation of vat dyes. Formula: C₈H₅NO₂. Is found in many plants and Schiff bases of Isatin are investigated for their pharmaceutical properties (Jarrahpour and Khalili, 2005). This was prepared according to the literature method, Isatins can be made from the corresponding indole in good yield by a mixing of InCl₃ and IBX in an acetonitrile-water solution at 80°C (Yadav, et al., 2007). The electrophilic carbon atoms of Isatin carbonyl group can be targets of nucleophilic attack by amines (Jarrahpour and Khalili, 2005). 3-Aminoacetophenone is one of the most typical aromatic carbonyls which show photochemical properties 3-aminoacetophenone with molecular formula C₈H₉NO, having melting point 96–98°C. Another additional interest that 3-aminoacetophenone derivatives possess some degree of local anesthetic activities (Nomenclature of Organic Chemistry, 2014). Acetophenone is used for the synthesis of many pharmaceuticals (Braish and Gadamasetti, 2007). Acetophenone is recovered as a by-product of the oxidation of ethylbenzene to ethylbenzene hydroperoxide (Siegel H., Eggersdorfer M., 2005). In this work, we report the synthesis characterization of Isatin compound with 3-aminoacetophenone and its complexes with selected transition elements such as Ni^{II} and Co^{II}, the antibacterial activity of the prepared complexes has been tested against Gram-positive *Staphylococcus aureus* and *Bacillus subtilis* (Shaker, et al., 2013) (Fig. 1).

II. EXPERIMENTAL

Reagents were purchased from Fluka and Redial - Dehenge Chemical Co. and used without further putrefaction. Fourier transform infrared (FT-I.R) spectra were recorded in the range 4000–400/cm. Electronic spectra of the prepared compounds

ARO-The Scientific Journal of Koya University
Volume VI, No 1(2018), Article ID: ARO.10245, 8 pages
DOI: 10.14500/aro.10245

Received 11 May 2017; Accepted 03 May 2018

Regular research paper: Published 25 May 2018

Corresponding author's e-mail: eman.ibraheem@koyauniversity.org

Copyright © 2018 Eman I. Alsalihi, Aeed S. Al-Fahdawi. This is

an open-access article distributed under the Creative Commons Attribution License.



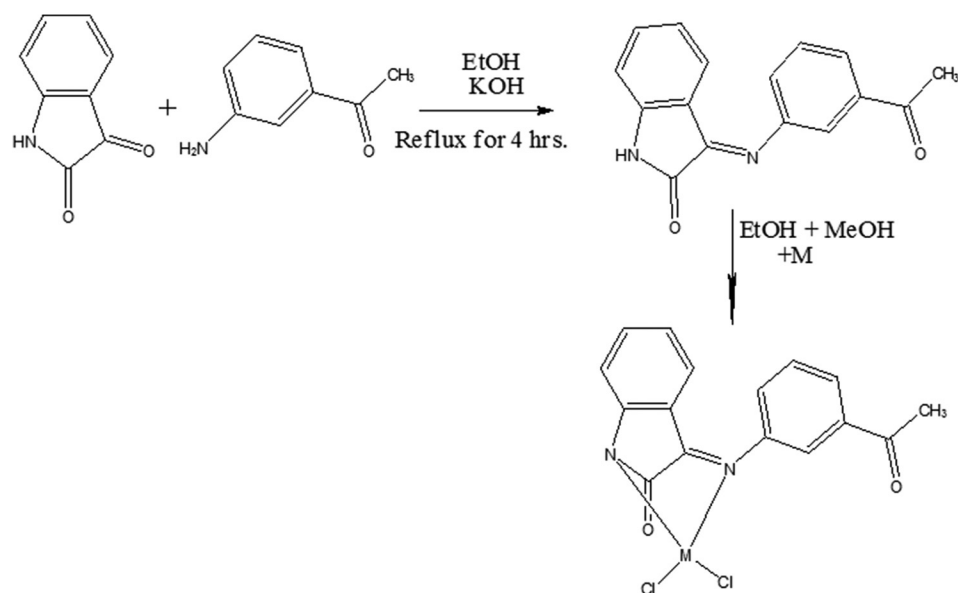


Fig.1. The synthesis route of the complexes (Where M = Ni^{II} and Co^{II})

were measured in the region 200–900 nm for 10⁻³ M solutions in methanol for the ligand and in distilled water for the complexes at 25°C using a Shimadzu 160 spectrophotometer with 1.000–0.001 cm matched quartz cell. Elemental microanalyses were performed on a (C.H.N) analyzer.

A. Syntheses of the ligand (E)-3-(3-acetylphenylimino)indolin-2-one [HL]

The ligand (E)-3-(3-acetylphenylimino)indolin-2-one type [HL] has been prepared from dissolving (0.3 g and 2.039 mmole) of Isatin in 25 ml ethanol, and mixed with a solution of 3-aminoacetophenone (0.275 g and 2.034 mmole) under refluxed for 4 h to gain (0.2 g) of a pale brown precipitate after filtration and drying at room temperature, to yield 66.6%, mp (63°C).

B. Syntheses of [Ni(L)Cl₂] complex

[Ni(L)Cl₂] complex has been prepared from 0.15 g, 0.567 mmole of [HL] dissolved in 25 mL methanol with a solution of 0.134 g, 0.663 mmole of NiCl₂·6H₂O. Moreover, refluxed for 2 h to obtain (0.11 g) pale yellow precipitate. Yield 73%, mp 134°C.

C. Syntheses of [Co(L)Cl₂] complex

The same method used to prepare [Ni(L)Cl₂] complex was used to prepare [Co(L)Cl₂] complex but with a solution of 0.13 g, 0.546 mmole of CoCl₂·6H₂O to form (0.13 g) deep brown precipitate. Yield 86.6%, 118°C. Table I shows the microanalysis results and some physical properties for the ligand and its complexes.

III. RESULTS AND DISCUSSION

A. Synthesis of the ligand [HL]

The (FT-I.R) spectra for the starting materials of the ligand [HL], the essential infrared data are summarized in Table II.

In the spectrum of 3-aminoacetophenone, there are two sharp absorption bands at 3470 and 3450/cm that assigned to the stretching vibration of $\nu_{\text{sy}}(\text{N-H})$ and $\nu_{\text{asy}}(\text{N-H})$ of the primary amine (R-NH₂) group (Nakamoto, 1997) (Fig. 2). These bands have been disappeared in the spectrum of the ligand [HL], because of its condensation reaction with Isatin.

In the spectrum of Isatin Fig. 3., there is a band at 3450.6/cm due to the $\nu(\text{N-H})$ of the secondary amine (R₂-NH) group (Rostkowska, et al., 1993), is shifted to lower frequency about (50/cm) as shown in the spectrum of the ligand [HL] as a consequence of the coordination between both of Isatin and 3-aminoacetophenone.

The appearance of a new band at 1550/cm range in the spectrum of [HL] ligand was assigned to the $\nu(\text{C=N})$ stretching, indicating formation a new compound and Schiff base reactions (Ali, et al., 1981; Ivanov and Nikolova, 2008) 3-aminoacetophenone and Isatin. Figs. 2 and 3 displayed strong bands at 1728/cm and 1695/cm range, assigned to the stretching vibration of $\nu(\text{C=O})$ group, respectively, which are shifted to lower frequency at 1650/cm compared with the spectra of the ligand [HL] (Anuradha and Rajarel, 2011; Colchoubian, et al., 1999) (Fig. 4).

U.V-Vis spectrum for [HL], Fig.5. exhibits a high intense absorption peak at 240 nm (41666/cm) ($\epsilon_{\text{max}} = 450/\text{molar}/\text{cm}$), assigned for $n \rightarrow \pi^*$. A shoulder peaks at 290 nm (34482/cm) ($\epsilon_{\text{max}} = 366/\text{molar}/\text{cm}$) and (339 nm) (29498/cm) ($\epsilon_{\text{max}} = 120/\text{molar}/\text{cm}$) were assigned to $\pi \rightarrow \pi^*$ transitions (Colchoubian, et al., 1999; Kindeel, et al., 2013) (Table III).

B. Synthesis of the complexes

The reaction of the ligand [HL] with Co^{II} and Ni^{II} was carried out in methanol under reflux. All complexes are stable in the solid state. The analytical and physical data, Table I and spectral data Table III are compatible with the suggested structures. FT-I.R spectra of the complexes are shown in Figs. 6 and 7 and the predominant bands are summarized in Table II.

TABLE I
THE MICROANALYSIS RESULTS AND SOME PHYSICAL PROPERTIES OF [HL] AND ITS COMPLEXES

compound	M.W	Yield%	M p. °C	Color	Formed (cal. %)-(theo. %)				
					C	H	N	Cl	Metal
[HL]	264.28	66.6	63	Pale-Brown	71.55 72.72	4.01 4.58	9.16 10.60	-	-
[Ni (L) Cl ₂]	463.78	73	134	Pale-Yellow	45.65 48.91	2.122.82	6.01 7.13	16.89 18.05	13.22 14.94
[Co (L) Cl ₂]	464.02	86.6	118°	Deep-Brown	44.01 48.88	2.31 2.82	6.11 7.13	17.00 18.04	13.06 14.99

TABLE II
FT-IR SPECTRAL DATA (WAVE NUMBER ν)/CM OF THE DERIVATIVE LIGAND [HL] AND ITS PRECURSORS WITH THE COMPLEX

Compound	ν (N-H)	ν (N-H) Secondary R ₂ -NH	ν (C=O)	ν (C=N)-Imine	M-O
	Primary-R-NH ₂				M-N
3-aminoacetophenone	3470 3450	-	1695	-	-
Istian	-	3450.6(sh)	1728(sh)	-	-
[HL]	-	3400	1650	1550	-
[Ni (L) Cl ₂]	-	-	1670	1592	530
[Co (L) Cl ₂]	-	-	1665	1595	526
	-	-	-	-	580

TABLE III
ELECTRONIC SPECTRAL DATA AND CONDUCTANCE MEASUREMENTS OF THE LIGAND AND ITS COMPLEXES

Compound	λ nm	cm ⁻¹ ν wave number	ϵ_{Max} /molar/cm	Assignments	conductance	B.M
[HL]	240	41666	450	n \rightarrow π^*		
	290	34482	366	$\pi\rightarrow\pi^*$		
	339	29498	120	$\pi\rightarrow\pi^*$		
[Ni (L) Cl ₂]	240	41666	1141	Ligand field	20	2.9
	285	35087	440	C.T		
	410	24390	200	¹ A ₁ \rightarrow ¹ E'		
	425	23529	180	¹ A ₁ \rightarrow ¹ E		
[Co (L) Cl ₂]	255	39215	904	Ligand field	16	1.6
	291	34364	1122	C.T		
	394	25380	309	⁴ A _{2g} \rightarrow ⁴ T _{1g} (F)		
	447	22371	103	⁴ A _{2g} \rightarrow ⁴ T _{2g}		

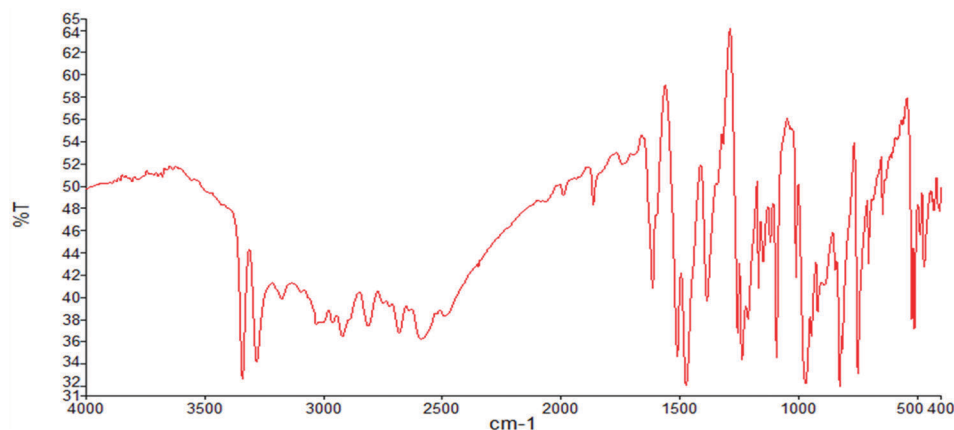


Fig. 2. The Fourier transform infrared spectrum of 3-aminoacetophenone

The band at 1650/cm⁻¹ of the ν (C=O) stretching vibration (Ali, et al., 1981; Ivanov and Nikolova, 2008) of the ligand is shifted

to higher frequencies at 1670–1665 range for Ni^{II} and Co^{II} complexes because of the coordination with the metal ions.

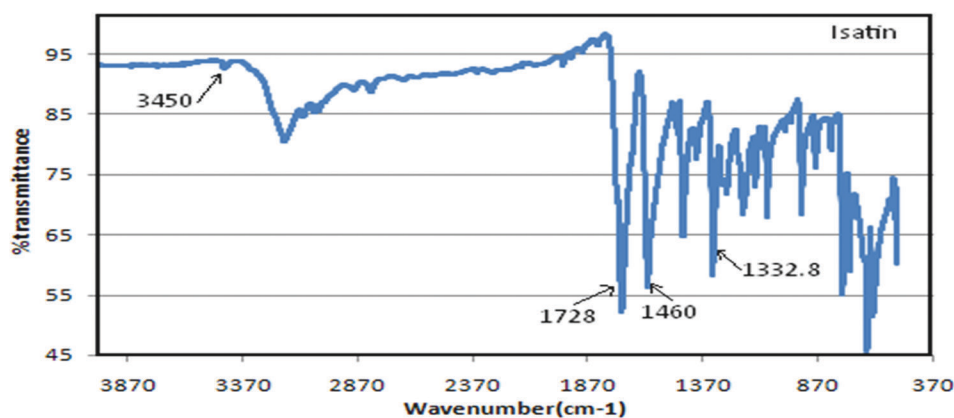


Fig. 3. The Fourier transform infrared spectrum of Isatin

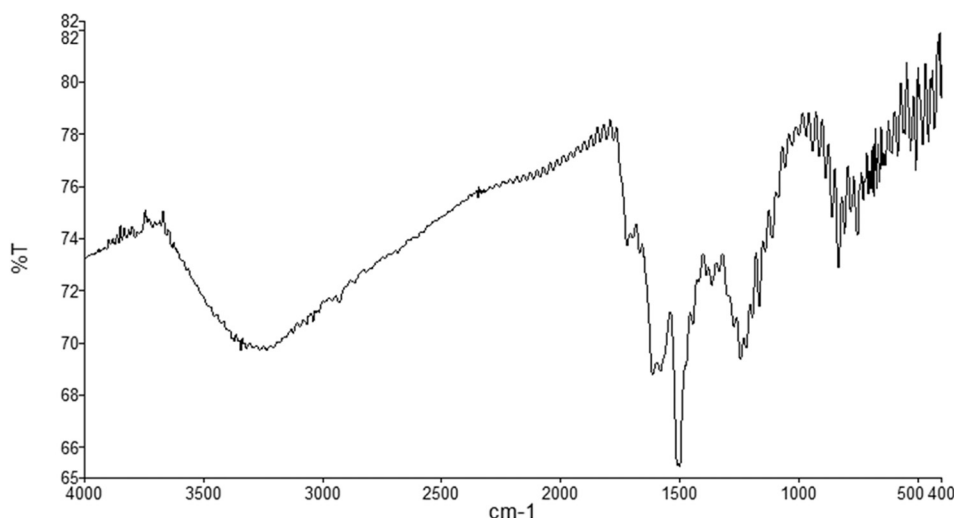


Fig.4. The Fourier transform infrared spectrum of [HL] ligand

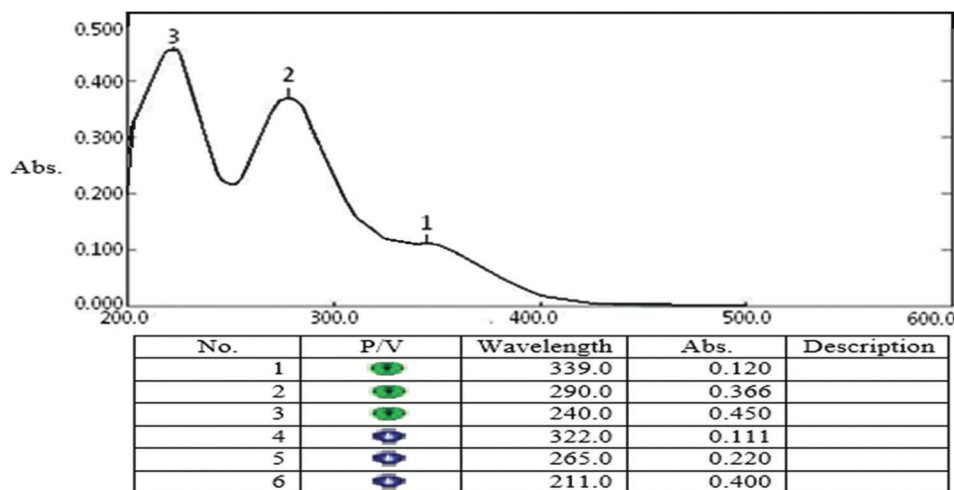
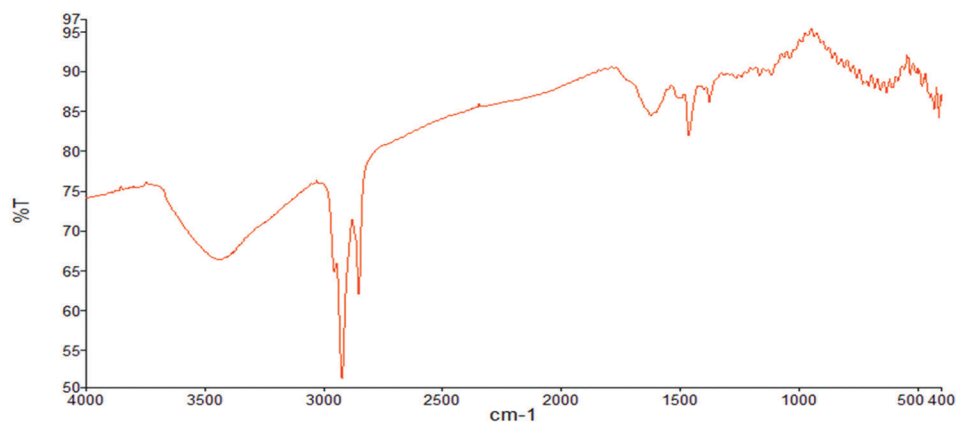
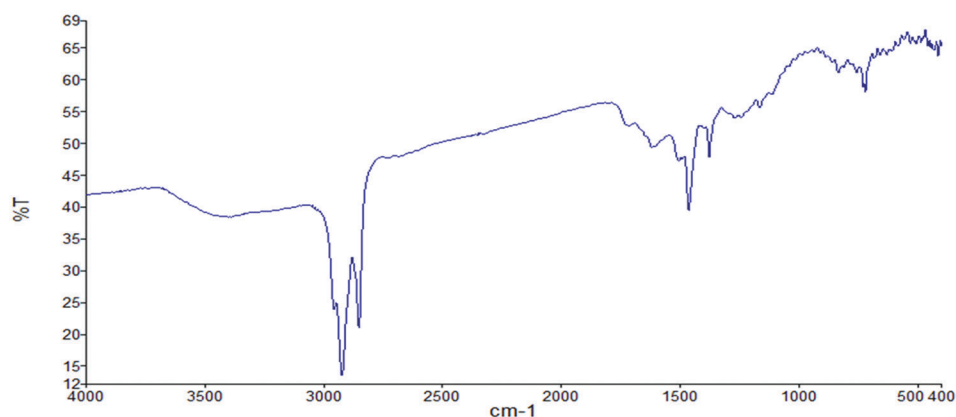
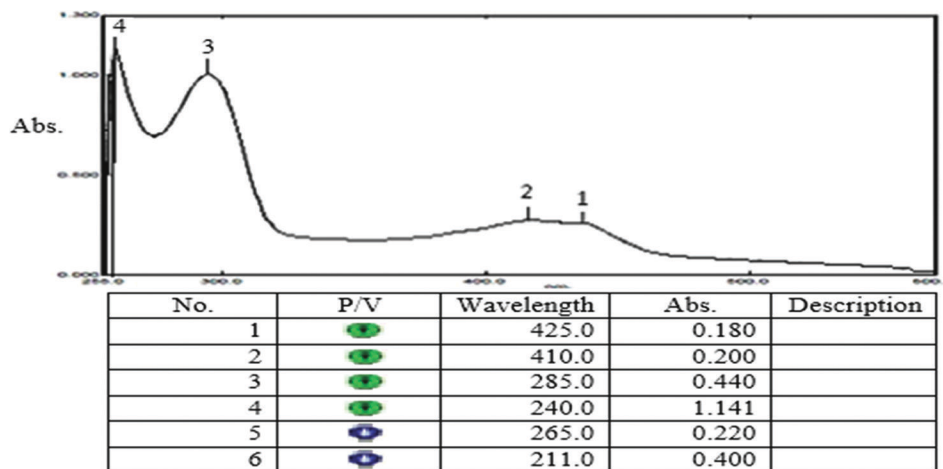


Fig. 5. The ultraviolet-visible spectrum of [HL] ligand

Moreover, the band at 1550/cm¹ of $\nu(\text{C}=\text{N})$ imine (Anuradha and Rajarel, 2011; Colchoubian, et al., 1999) is shifted to higher frequencies about (40/cm) range for the complexes due to the forming ring system with the metal ions. Metal oxygen and metal nitrogen band further confirmed by the presence of

peaks at 530–590/cm and 526–580/cm range were assigned to $\nu(\text{M}-\text{O})$ and $\nu(\text{M}-\text{N})$ (Halli, et al., 2012; Jakels, et al., 1983) stretches for the Ni^{II} and Co^{II} complexes, respectively.

UV-Vis spectra of Ni^{II} and Co^{II} complexes Figs. 8 and 9, respectively, showed two intense peaks in the range 240 nm,

Fig. 6. The Fourier transform infrared spectrum of [Ni(L)Cl₂] complexFig. 7. The Fourier transform infrared spectrum of [Co(L)Cl₂] complexFig. 8. The ultraviolet-visible spectrum of [Ni(L)Cl₂] complex

(41666/cm), ($\epsilon_{\max} = 1141/\text{molar/cm}$) and 255 nm, ($39215/\text{cm}^{-1}$), ($\epsilon_{\max} = 904/\text{molar/cm}$) range assigned to the ligand field for Ni^{II} and Co^{II}, respectively (Lever, 1984). Another two peaks at 285 nm, ($35087/\text{cm}$), ($\epsilon_{\max} = 440/\text{molar/cm}$) and (291 nm), ($34364/\text{cm}$), ($\epsilon_{\max} = 1122/\text{molar/cm}$) range assigned to the charge transfer transition for Ni^{II} and Co^{II}, respectively (Al-Shihri, 2004). Another two peaks are detected in the visible region for Ni^{II} complex at 410 nm, ($24390/\text{cm}$), ($\epsilon_{\max} = 200/$

molar/cm) and (425 nm), ($23529/\text{cm}$), ($\epsilon_{\max} = 180/\text{molar/cm}$) are due to (${}^1A_1 \rightarrow {}^1E'$) and (${}^1A_1 \rightarrow {}^1E''$) transitions indicating a tetrahedral structure (Lever, 1984) around Ni^{II}. So that for the two peaks of Co^{II} complex at 394 nm, ($25380/\text{cm}$), ($\epsilon_{\max} = 309/\text{molar/cm}$) and (447 nm), ($22371/\text{cm}$), ($\epsilon_{\max} = 103/\text{molar/cm}$) are assigned to (${}^4A_g \rightarrow {}^4T_{1g(F)}$) and (${}^4A_g \rightarrow {}^4T_{2g}$) transitions (Al-Shihri, 2004), suggesting a tetrahedral structure around Co^{II} ion. is assigned to d-d transitions (AL-Shihri, 2004).

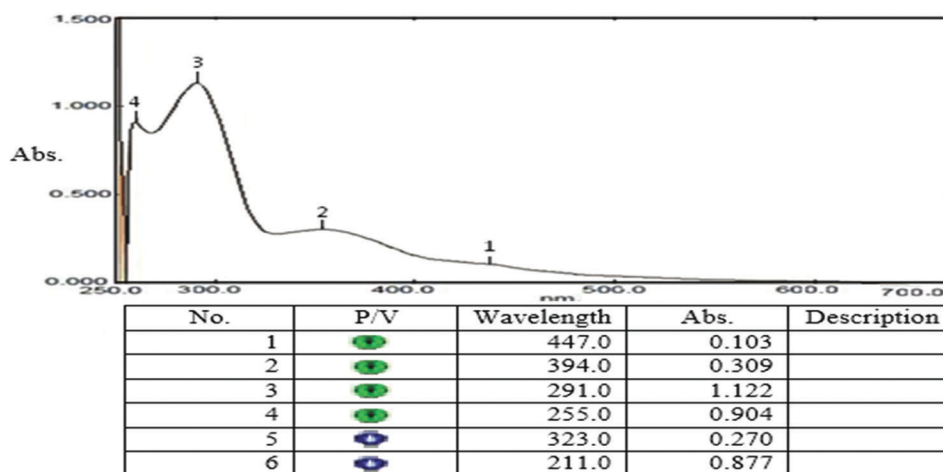


Fig. 9. The ultraviolet-visible spectrum of [Co(L)Cl₂] complex

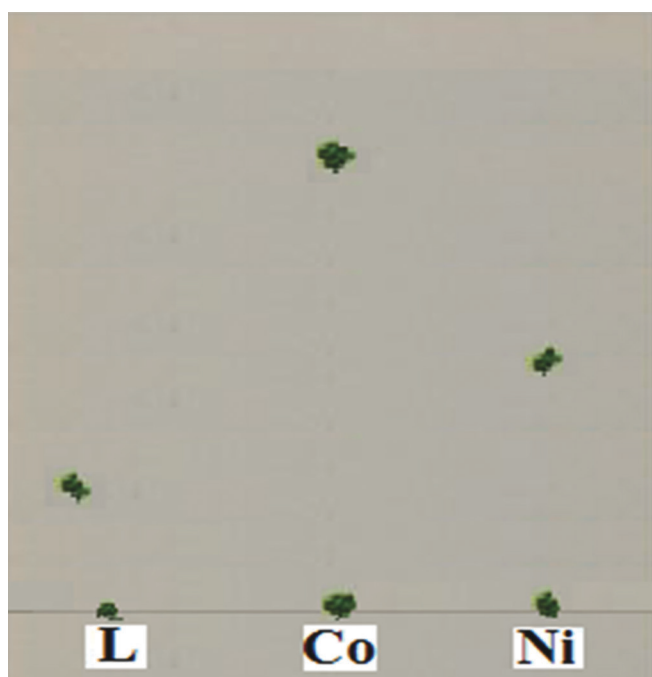


Fig. 10. The thin-layer chromatography for the ligand and its Ni^{II}, Co^{II} complexes

Thin-layer chromatography (TLC) measurement for the derivative ligands [HL] and its complexes were performed with Co^{II} and Ni^{II} is showed in Fig. 10. and Table IV. The appearance of new spots with different R_f compared with the R_f of the ligands, for Co^{II} and Ni^{II} indicated the formation of the complexes. The spots positions belong to Co^{II}, and Ni^{II} ion complexes are differ from the positions of the ligands spot.

Biological activity of the [HL] ligand and its two complexes was tested on two types of pathogenic bacteria using inhibition method (Anacona, 2006; Sultana and Arayne,2007). The two types of bacteria were Gram-positive *S. aureus* and *B. subtilis*. The ligand [HL] showed inhibition diameter against the two types of bacterial after 24 h and this inhibition diameter was increased after 48 h (Fig. 11). Furthermore, experimental results indicated that

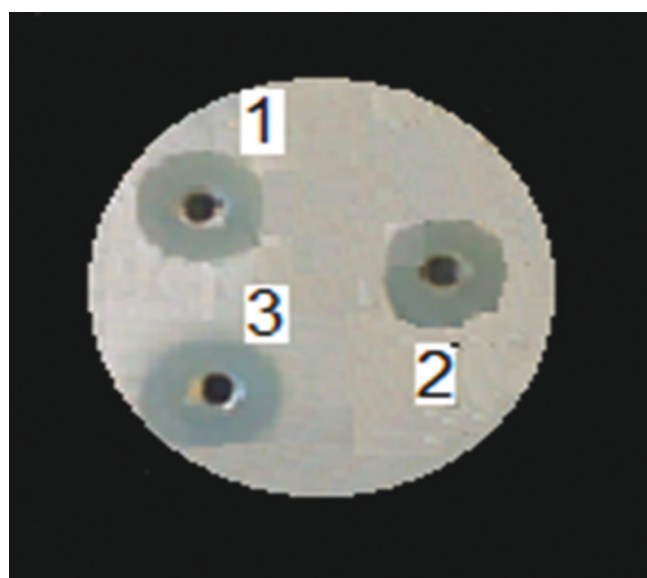


Fig. 11. The biological activity of [HL] and its Ni^{II}, Co^{II} complexes

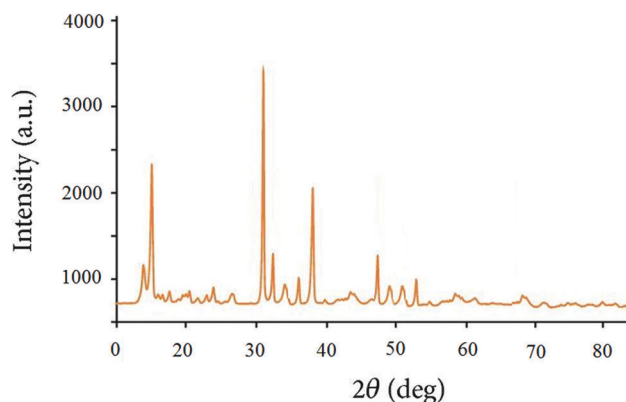


Fig. 12. The X-ray powder diffraction of [Co(L)Cl₂] complex

the complexes show more activity than the ligand under similar experimental conditions with the same kinds of bacteria.

Molar conductance in DMSO solutions lie in the (16 and 20/cm/mole) range indicating its electrolytic nature with (1:1)

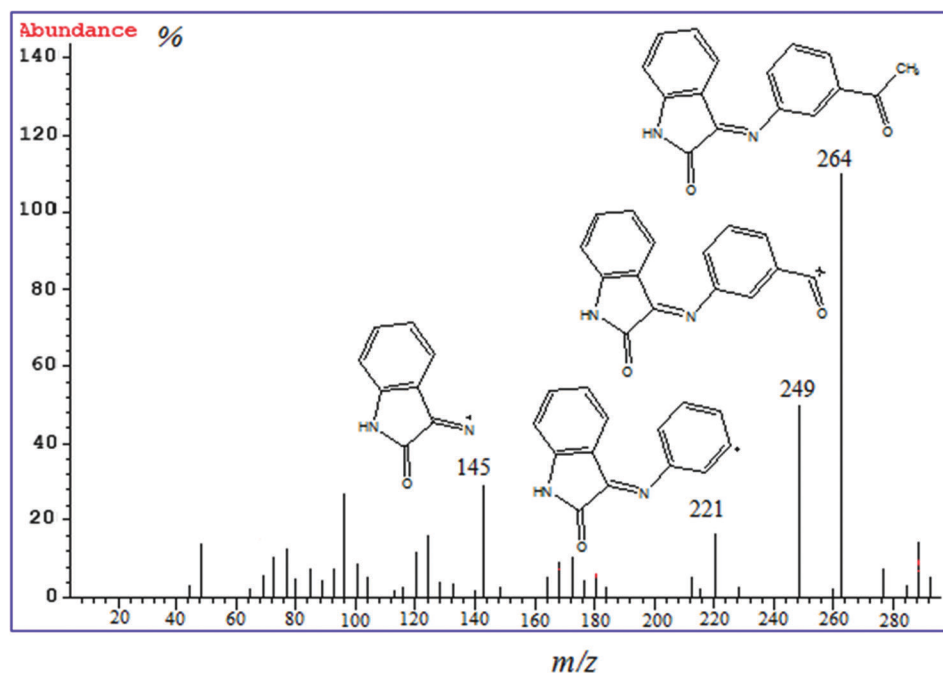


Fig. 13. The mass spectrum of [HL]

TABLE IV
THE TLC MEASUREMENTS FOR THE [HL] LIGAND AND ITS Co^{II} AND Ni^{II}
COMPLEXES

Compound	Range of R_f (mm)
[HL]	0.7
[Co (L) Cl_2]	3.3
[Ni (L) Cl_2]	2.2

TLC: Thin-layer chromatography

of the Co^{II} and Ni^{II} , metal ion complexes (Kai, et al., 2009; Refat and Struct, 2007) (Table I).

Magnetic moment (1.6 and 2.9 B.M) value of the Co^{II} and Ni^{II} ion complexes, respectively, as well as the other analytical data Table III is in agreement with the suggested structure of square planar geometry for the two complexes in the solid state (Uppadin, et al., 2001; Al-Jeboori, et al., 2010).

X-ray powder diffraction (XRD) pattern of Co^{II} complex shows well-defined crystalline peaks indicating that the sample is 37% crystalline in nature (Dokken, et al., 2009). An XRD powder diffraction pattern of the copper complex has been given in Fig. 12 of different scale particles are well coincident with each other, and it means that different forms of complexes have the same structure (Guillemet-Fritsch, et al., 2006). The sample has been dried and then scanned in the 2θ range of $10\text{--}80^\circ$ confirming square planar geometry around Co^{II} ion complex (Kavitha and Lakshmi, 2017; Zheng, et al., 2017).

Mass spectrum shows the base peak at 264 related to the molecular weight of the ligand. Moreover, all the other fragmentations are compatible with the value of the fragments of the ligand as shown in Fig. 13.

REFERENCES

- Abu-Dief Ahmed, A.M. and Mohamed, I.M.A., 2015. A review on versatile applications of transition metal complexes incorporating Schiff bases. Beni-Suef University Journal of Basic and Applied Sciences, 4, pp.119-133.
- Ali, H., Al-Azawi, S., Silverschtein, R.M., Bassler, G.C. and Morril, T.C., 1981. *Spectrophotometers Identification of Organic Compounds*. John Wiley and Sons, New York.
- Al-Jeboori, M.J., Al-Tawel, H.H. and Mahmood, R., 2010. New metal complexes of N2S2 tetradentate ligands: Synthesis and spectral studies. *Inorganica Chimica Acta*, 363, pp.1301-1305.
- Al-Shihri, A.S., 2004. *Spectrochimica Acta*. Part A, 60, pp.1189-1192.
- Anacona, J.R. 2006. Synthesis and antibacterial activity of some metal complexes of β -Lactams antibiotics. *Journal of Coordination Chemistry*, 54, pp.355-365.
- Anuradha, K. and Rajareel, R., 2011. Synthesis, spectral characterization and biological activity of new symmetrical macrocyclic binuclear Schiff base complexes. *Internatiol Journal of Pharmacy and Technology*, 2, pp.2217.
- Asadi M., Sepehrpour, H. and Mohammadi, K.H., 2011. "Tetradentate schiff base ligands of 3,4-diaminobenzophenone: Synthesis, characterization and thermodynamics of complex formation with Ni(II), Cu(II) and Zn(II) metal ions. *Journal of the Serbian Chemical Society*, 76, pp.63-74.
- Siegel, H., Eggersdorfer, M., 2005. Ketones, *Ullmann's encyclopedia of industrial chemistry*, weinheim: wiley VCH. doi:10.1002/14356007.a15_077. (<https://en.wikipedia.org/wiki/Acetophenone>).
- Braish, T. and Gadamasetti, K., 2007. *Process Chemistry in the Pharmaceutical Industry*, Vol. 2. CRC Press, Boca Raton, pp.142-145.
- Chamayou, A.C., Lüdeke, S., Brecht, V., Freedman, T.B., Nafie, L.A. and Janiak, C., 2011. Chirality and diastereoselection of Δ/∇ -configured tetrahedral zinc complexes through enantiopure Schiff base complexes: Combined vibrational circular dichroism, density functional theory, ^1H NMR, and X-ray structural studies. *Inorganic Chemistry*, 50, pp.11363-11374.
- Colchoubian, H., Waltz, W.L. and Quail, J.W., 1999. Synthesis and characterization of Schiff base folic acid based ligand and its complexes. *Canadian Journal of Chemistry*, pp.37-77.

- Da Silva Cleiton, M., da Silva Daniel, L., Modolo, L.V., Alves, R.B., de Resende, M.A., Martins, C.V.B. and Ângelode, F., 2011. Schiff bases: A short review of their antimicrobial activities. *Journal of Advanced Research*, 2, pp.1-8.
- Dokken, K.M., Parsons, J.G., McClure, J. and Gardea-Torresdey, J.L., 2009. Synthesis and structural analysis of copper(II) cysteine complexes. *Inorganica Chimica Acta*, 362, pp.395-401.
- Guillemet-Fritsch, S., Lebey, T., Boulos, M. and Durand, B. 2006. Dielectric properties of CaCu₃Ti₄O₁₂ based multiphased ceramics. *Journal of the European Ceramic Society*, 26, pp.1245-1257.
- Halli, M.B., Patil, V.B., Sumathi, R.B. and Mallikarjun, K., 2012. Synthesis, characterization and biological activity of mixed ligand metal (II) complexes derived from benzofuran-2-carbohydrazide schiff base and malonyldihydrazide. *Der Pharma Chemica*, 4, pp.2360-2323.
- Ivanov, I. and Nikolova, S., 2008. *Synthesis of New β-enaminones of Isoquinolines with 5, 5-Dimethyl-cyclohexanedione*. Molbank, Plovdiv. pp.565.
- Jakels, S.C., Ciavola, J., Carter, R.C., Cheek, P.L. and Pascarlhi, T.D., 1983. *Inorganic Chemistry*, 22, pp.3956.
- Jarrahpour, A.A. and Khalili, D., 2005. Synthesis of some new bis-Schiff Bases of Isatin and 5-fluoroisatin in a water suspension medium. *Molecules*, 11, pp.59-63.
- Kai, Y., Gu, Z., Ji, R. and Lou, L.S., 2009. Heterogeneous chiral Mn(II) salen catalysts for the epoxidation of unfunctionalized olefins immobilized on mesoporous materials with different pore sizes. *Tetrahedron*, 65, pp.305-311.
- Kavitha, N. and Lakshmi, P.V.A., 2017. Synthesis, characterization and thermogravimetric analysis of Co(II), Ni(II), Cu(II) and Zn(II) complexes supported by ONNO tetradentate Schiff base ligand derived from hydrazine benzoxazine. *Journal of Saudi Chemical Society*, 21 Suppl 1, pp.S457-S466.
- Kindeel, A.S., Dawood, I.J. and Aziz, M.R., 2013. Synthesis and characterization of some mixed ligand complexes containing (8-hydroxyquinoline) and (2-picoline) with some metal ions. *Baghdad Science Journal*, 10, pp.396.
- Lever, A.B.P., 1984. *Inorganic Electronic Spectroscopy*. 2nd ed., Elsevier, New York.
- Monfared, H.H., Vahedpour, M., Yeganeh, M.M., Ghorbanloo, M., Mayer, P. and Janiak, C. 2011. Concentration dependent tautomerism in green [Cu(HL1)(L2)] and brown [Cu(L1)(HL2)] with H₂L1=(E)-N'-(2-hydroxy-3-methoxybenzylidene) benzoylhydrazone and HL2=pyridine-4-carboxylic (isonicotinic) acid. *Dalton Transactions*, 40, pp.1286-1294.
- Nakamoto, K., 1997. *Infrared and Raman Spectra of Inorganic and Coordination Compounds*, Parts A and B. 5th ed. John Wiley Sons, New York.
- Nomenclature of Organic Chemistry: IUPAC Recommendations and Preferred Names. 2013. *Blue Book*. The Royal Society of Chemistry, Cambridge. pp.723.
- Refat, M.S., and Struct, J.M., 2007. Complexes of uranyl (II), vanadyl (II) and zirconyl (II) with orotic acid "vitamin B13": Synthesis, spectroscopic, thermal studies and antibacterial activity. Article in *Journal of Molecular Structure*, 842, pp.24.
- Rostkowska, N.M.J., Lapinski, L., Bertner, M., Kulikowski, T., Les, A. and Adamowicz, L., 1993. *Spectrochim. Acta A*, 49, pp.551.
- Shaker, A.M., Nassr, L.A.E. and Adam, M.M.S.S., 2013. Synthesis, characterization and spectrophotometric studies of seven novel antibacterial hydrophilic iron (II) Schiff base amino acid complexes. *Journal of the Korean Chemical Society*, 5, pp.560.
- Sultana, N. and Arayne, M.S., 2007. *In vitro* activity of cefadroxil, cephalexin, cefatrizine and cefpirome in presence of essential and trace elements. *Pakistan Journal of Pharmaceutical Sciences*, 20, pp.305-10.
- Uppadin, L.H., Weeks, J.M. and Beer, P.D., 2001. Metal-directed self-assembly of terphenyl based dithiocarbamate ligands. *Journal of the Chemical Society Dalton Transactions*, 22, pp.3367-3372.
- Yadav, J.S., Reddy, B.V.S., Reddy, C.S. and Krishna, A., 2007. Indium(III) chloride/2-iodoxybenzoic acid: A novel reagent system for the conversion of indoles to isatins. *Synthesis*, 5, pp.693-696.
- Zheng, Z., Junwei, X., Sisi, Y., Yangli, C., Yan, W., Zhuo, C. and Chunlin, N., 2017. Two organic cation salts containing tetra (isothiocyanate)cobaltate(II): Synthesis, crystal structures, spectroscopic, optical and magnetic properties. *Crystals*, 7, pp.92.

Evaluating the Wear of Polycrystalline Diamond Compact Drill Bit Cutters using Indentation and Scratch Tests

Rafid K. Abbas¹ and Ali Hassanpour²

¹Department of Chemical Engineering, Faculty of Engineering, University of Al-Qadisiyah, Al-Diwaniya, 58002, F.R. Iraq

²Institute of Particle Science and Engineering, School of Chemical and Process Engineering, University of Leeds, LS2 9JT, United Kingdom, England

Abstract—Polycrystalline diamond compact (PDC) drill bits are widely used in oil and gas drilling. The wear of PDC cutters is a major problem during drilling. It leads to severe time losses which affect the overall drilling operation cost. Therefore, it is essential to evaluate the wear tendency for these cutters using predictive approaches. The present research is focused on studying the wear mechanisms of PDC cutters and the effect of their mechanical properties on the extent of wear. The volume of wear for the PDC cutters was determined experimentally using micro- and nano-scratch tests by implementing an approach based on the geometry of the removed material after micro- and nano-scratch tests. The experimental wear results were compared to the predictions from current models in the literature. Various wear models are evaluated for micro- and nano-scratch tests on both layers of the PDC samples. The study shows that the wear of the PDC cutters can be predicted from the material mechanical properties, applied load, sliding distance, and hardness of the PDC cutters. The study could be extended for the evaluation of wear intensity of PDC cutters from various manufactures without using the previous techniques of abrasion testing.

Index Terms—Bit wear, Indentation, Micro-scratch test, Nano-scratch test, Polycrystalline diamond compact.

I. INTRODUCTION

Drilling for oil and gas is still very demanding in many areas around the world. The use of polycrystalline diamond compact (PDC) bits is widely spread nowadays due to their high performance and durability in harsh environments. Synthetic diamond cutters or inserts that are placed on the PDC bit represent the most significant part of these bits. PDC cutters have significantly increased drill bit efficiency and drilling performance to a point where PDC bits have overtaken tricone bits in many oil and gas drilling

applications. Since the first commercial introduction of PDC bits in 1976, many challenges appeared that sometimes halted their applicability, especially in hard geological formations, where abrasive wear and impact damage prevail. Wear of drilling bits is due to macroscopic or microscopic removal or fracture of material, especially at the cutter surface.

Mouritz and Hutchings (1991) investigated the wear rates of the materials used in the teeth of the rotary drilling bits and the abrasive wear mechanisms of these materials. Richardson (1968) showed that abrasive wear rate of any ductile material depended on the ratio of its hardness (Hm) to that of the abrasive (Ha). When $H_a/H_m < 1$, this means that the abrasive cannot scratch the material and the wear rate is extremely low. However, when $H_a/H_m > 1.2$, the abrasive can scratch the material and cause high wear rate (Mouritz and Hutchings, 1991). Geoffroy (1999) showed that more than 50% of the energy of the drilling by PDC bits is dissipated by the wear of cutters under normal drilling conditions, assuming a steady motion and avoiding excessive heating. Fang, et al. (2001) described that the main failure modes of PDC cutters are due to frictional heat and abrasiveness of the rock as shown in Fig. 1.

Tze-Pin, et al. (1992) and Zacny (2012) postulated four primary failure modes of PDC cutters according to the type of wear mechanism: 1 - smooth wear, 2 - microchipping, 3 - gross fracturing or spalling, and 4 - delamination.

Various tests have been carried out on PDC bits and, especially, their cutters to assess their performance and applicability in diverse drilling conditions including harsh environment and high-temperature conditions. Bellin, et al. (2010a) mentioned that the majority of the previous tests are broadly destructive. Abrasion test is the well-known one, where the abrasion resistance of the cutter against abrasive rocks is evaluated. It depends mainly on the hardness of the minerals in the rock. Highly abrasive rocks like granite or hard sandstone are normally used in the abrasion test. The wear of the PDC inserts has been evaluated and reported in the literature (Bellin, et al., 2010a); nevertheless, the precise assessment of the material loss remains a challenge. Therefore, the current study is focused on this topic, that is, determining the wear volume of the diamond layer as well

ARO-The Scientific Journal of Koya University
Volume VI, No.1(2018), Article ID: ARO.10278, 9 pages
DOI: 10.14500/aro.10278

Received 22 July 2017; Accepted 12 April 2018

Regular research paper; Published 31 May 2018

Corresponding author's, e-mail: Rafid.Abbas@qu.edu.iq

Copyright © 2018 Abbas RK, Hassanpour A. This is an open-access article distributed under the Creative Commons Attribution License.



as the substrate of the PDC cutters after applying micro- and nano-mechanical testing.

II. METHODOLOGY

A series of micro- and nano-indentation tests were carried out to determine the mechanical properties of the materials forming the PDC samples. The samples are in the form of cylindrical disks with different dimensions. The images of four PDC cutters that have been used in the experiments are shown in Fig. 2. The specifications of the PDC cutters supplied from two different manufacturers are given in Table I. The upper part of the PDC cutters is made of diamond layer in the form of PDC with cobalt as a binder, whereas the lowest layer (substrate) consists of tungsten carbide embedded in cobalt as a binder. PDC specimens were finely polished to reduce the effect of surface asperities and consequently to reduce the measurement error of hardness and Young's modulus. Furthermore, well-polished surfaces will produce clearer imprints from micro- and nano-indentations and enable better measurements of the diagonals

TABLE I
SPECIFICATIONS OF THE PDC SPECIMENS

Commercial order	Cutter diameter (mm)	Cutter height (mm)	Diamond thickness (mm)
M1308	13.44 (±0.03)	8.0 (±0.1)	2.2 (±0.2)
M1313	13.44 (±0.03)	13.2 (±0.1)	2.2 (±0.2)
K1608	16.00 (±0.05)	8.0 (±0.1)	2.0-2.5
K1908	19.05 (±0.05)	8.0 (±0.1)	2.0-2.5

PDC: Polycrystalline diamond compact

of the obtained indents. Following the above characterization work, micro- and nano-scratch tests were carried out, and the results were compared with the predictions from the wear models in the literature.

III. EXPERIMENTAL WORK

A. Micro- and nano-indentation tests

Micro- and nano-indentation measurements of hardness and Young's modulus of many materials have been performed by numerous researchers; nevertheless, many previous attempts for indenting the diamond layer of the PDC cutter have failed. Many researchers mentioned the failure to be due to the breakage of the indenter, and especially, the Berkovich type (Sumiya and Irifune, 2004). Nevertheless, the use of Berkovich probe was successful under very low loads, that is, <3 mN (Couvy, et al., 2011). In our work, nano-indentation hardness and Young's modulus of the diamond layer are measured using a Berkovich indenter using the NanoTest machine manufactured by Micro Materials Ltd., Wrexham, UK. A typical load-penetration plot for the indentation is shown in Fig. 3. Hardness and Young's modulus of the sample were obtained using the approach reported in the literature (Couvy, et al., 2011) but at different settings.

After completing the nano-indentation tests of the diamond layer, it is crucially important to check that the Berkovich probe has not been damaged. To do this, nanoindentation tests were carried out on a ceramic sample before and after the indentation process of the diamond layer. It was observed



Spalling

Chipping and heat checking

Breakage

Fig. 1. Typical failure modes of PCD inserts for rock drill bit (Fang, et al., 2001).

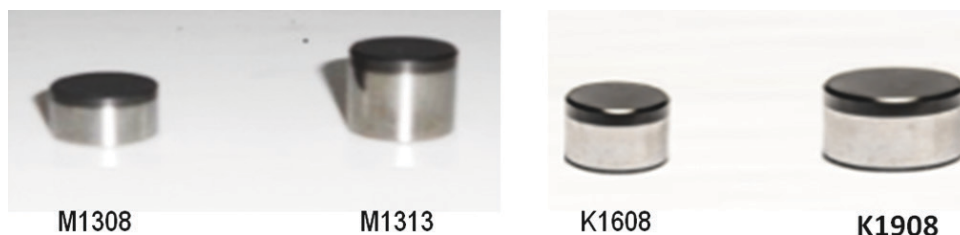


Fig. 2. Oil polycrystalline diamond compact cutters manufactured by two different manufacturers.

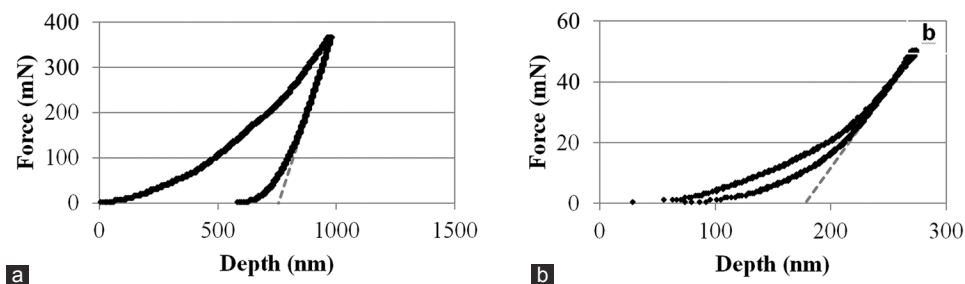


Fig. 3. (a) Applied force against displacement for tungsten carbide-cobalt at fixed load of 350 mN, (b) load versus the indentation depth for the polycrystalline diamond compact-Co at fixed load of 50 mN.

that the hardness and Young's modulus of ceramic before and after were nearly the same and this indicated that the tip of the nanoindenter was intact and not damaged.

The previous reported value of the hardness and Young's modulus of PDC was within the range 50-60 GPa and 776-925 GPa, respectively, depending on the diamond grain size and the percentage of the cobalt binder which varied from 5% to 20% (Dubrovinskaia, 2006), (Osipov, et al., 2010), and Ndlovu (2009). To prevent large fluctuation in the measurement of material properties, microindentation experiments were carried out. A series of microindentation tests were performed on the diamond and the substrate layers of the PDC samples using INSTRON 5566 equipment using Vickers indenter at various loads. Microindentations on diamond coatings require a highly polished test surface to discard the effect of the asperities that might cause undesirable results such as producing unclear indents. Fig. 4 illustrates the indents left after using Vickers probe on the substrate layer of sample K1908 after applying a load of 50 N. Table II demonstrates the average results of the hardness and Young's modulus determined from micro- and nano-indentation tests on both layers of the PDC samples. It is obvious that the standard deviation of the nanoindentation results is much higher than that of microindentation due to the aforementioned reason.

Fracture toughness was determined from the microindentation tests for the diamond and the substrate layers of the PDC inserts.

B. Microstructural properties and the cobalt content of PDC cutters

This part of the work is carried out to study the effect of the microstructural properties of the cutters on the mechanical properties of the diamond and substrate layers. The microstructural properties have been characterized by energy dispersive X-ray (EDX) images. The particles size of the coating (diamond) and the substrate (tungsten-carbide) has been quantified by the Image J software, whereas the weight percentage of the binder (cobalt) in the PDC samples has been determined from EDX element table content and from longitudinal measurement of the binder (cobalt) across the interface between the diamond and the substrate layers using (EDX-Quantline).

Backscattered detector (BSD) images are used for displaying the best resolution of the particle distribution

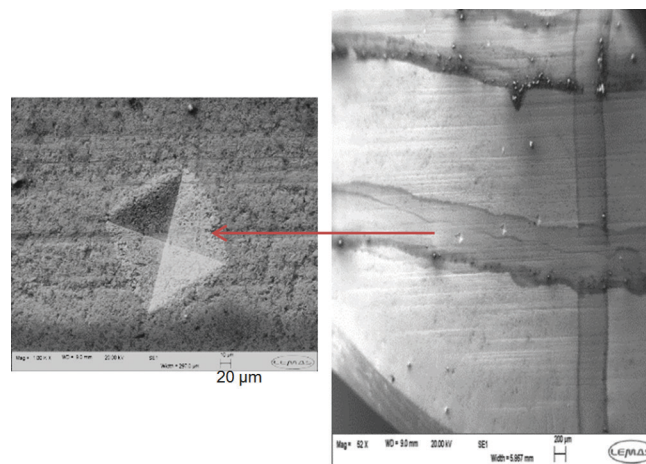


Fig. 4. Vickers imprints on the substrate of sample K190 after applying 50 N load.

compared to normal scanning electron microscope (SEM) images. EDX maps are used for determining the cobalt content in the diamond and the substrate layers of the PDC cutters.

The circular equivalent diameter of the diamond particles and substrate is determined by image J software after analyzing the BSD images. It should be noted that major drawback of this technique is that the size characteristics are based on two-dimensional (2D) image analysis and may not represent the particles third dimension.

Fig. 5 (top) shows the diamond particles (black areas) embedded in the cobalt binder (white areas) for samples M1313 (a) and K1908 (b). The particle size distribution of the diamond grains of samples M1313 and K1908 is shown in Fig. 5 (bottom).

Fig. 6 (top) illustrates the tungsten-carbide particles embedded in cobalt (blue) for (a) sample M1313 and (b) sample K1908, whereas Fig. 6 (bottom) demonstrates the tungsten-carbide grain size distribution for (c) specimen M1313 and (d) sample K1908.

The cobalt content represented as weight percentage is determined from EDX element content at various spectrum areas of the diamond and substrate layers, and then, averaged results with standard deviation are presented in Table III.

To summarize the microstructural obtained results, Table III shows the microstructural properties of two PDC samples from different manufacturers.

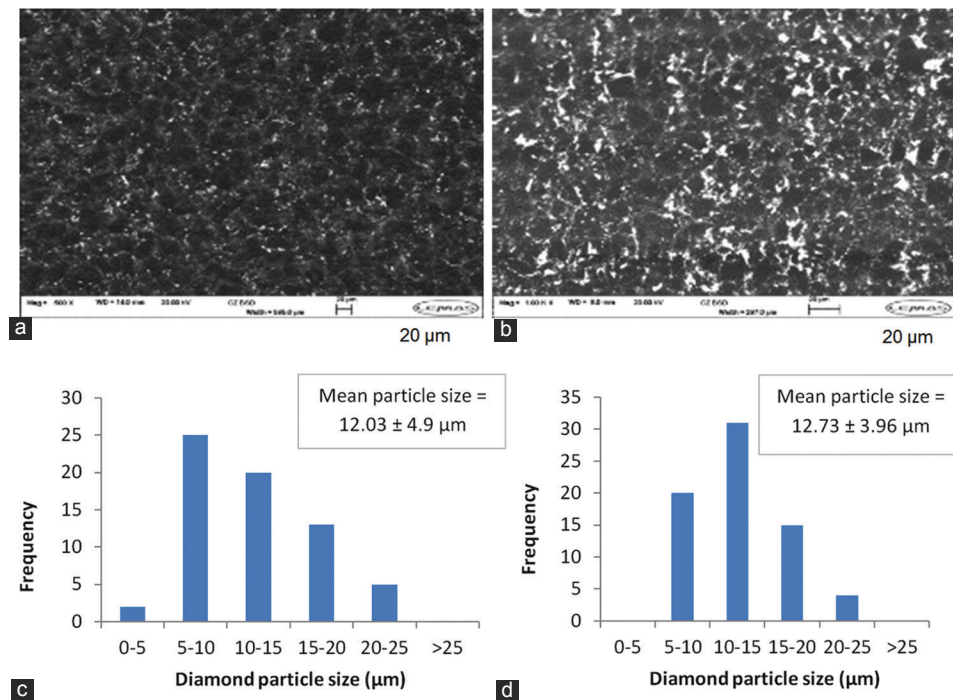


Fig. 5. (Top) Backscattered detector images. (a) sample M1313, (b) sample K1908 of the diamond layer displaying the diamond grains (black) and the cobalt (white), (bottom) diamond particle size distribution of sample M1313, and (c) sample K1908 (d).

TABLE II
MECHANICAL PROPERTIES OF PDC SAMPLES FROM MICRO- AND NANO-INDENTATION TESTS

PDC sample	Vickers hardness (GPa)	Yong's modulus (GPa)	Fracture toughness (MPa.m ^{1/2})	Layer
M1313 (Nano indentation)	16.69±6.59	487.96±161.18	N/A	Substrate
M1313 (Microindentation)	13.072±0.066	516.943±2.169	11.908±2.152	Substrate
K1908 (Microindentation)	12.564±0.257	514.344±0.877	12.277±2.146	Substrate
M1313 (Nanoindentation)	49.36±23.80	807.53±181.98	N/A	Diamond
M1313 (Microindentation)	50.85±0.912	864.534±0.986	9.13±1.219	Diamond
K1908 (Micro indentation)	46.092±0.754	855.63±4.474	9.641±1.064	Diamond

PDC: Polycrystalline diamond compact

TABLE III
STRUCTURAL PROPERTIES OF PDC INSERTS FROM DIFFERENT MANUFACTURERS

Microstructural properties	PDC samples	
	M1313	K1908
Diamond particle size (μm)	12.03±4.9	12.73±3.96
	min<4.52	min<6.9
	max>23.25	max>23.9
WC particle size (μm)	2.52±2.11	2.3 ±1.69
	min<0.38	min<0.3
	max>8.23	max>7.73
Co wt. % (in diamond)	3.26±0.5	4.4±0.51
Co wt. % (in WC-Co)	7.37±0.39	8.82±0.32

PDC: Polycrystalline diamond compact

Increasing the cobalt content for a given particle size causes the fracture toughness to increase, but it usually reduces the hardness (Bellin, et al., 2010c). It is also reported that fine tungsten carbide grain size and a low level of cobalt content lead to higher hardness and good wear resistance, whereas coarse particles and high cobalt content produce low hardness and high wear rate (Mori, et al., 2003; Ndlovu,

2009). Yahiaoui, et al. (2013) stated that the grain size and the content of cobalt are the most significant parameters of PDC cutters as high wear rate is associated with large particle size. Bellin, et al. (2010b) reported that the increasing the cobalt content in the diamond layer and the substrate will increase the fracture toughness, whereas the wear resistance increases with lower cobalt content.

The particle size of the substrate layer of samples M1313 and K1908 is around 2.3-2.5 μm, whereas the cobalt content in the substrate of sample M1313 is slightly lower than sample K1908. Accordingly, it is expected from these results that the abrasion (wear) resistance of sample M1313 is slightly greater than sample K1908, whereas sample K1908 has a better fracture toughness than sample M1313 (as can be seen from Table II).

The hardness of the diamond layer of sample M1313 found to be greater than the hardness of the sample K1908 as shown in Table II. This is mainly due to a lower level of binder content (3.26%) in sample M1313 compared to sample K1908 (4.4%), whereas the grain sizes are not that different.

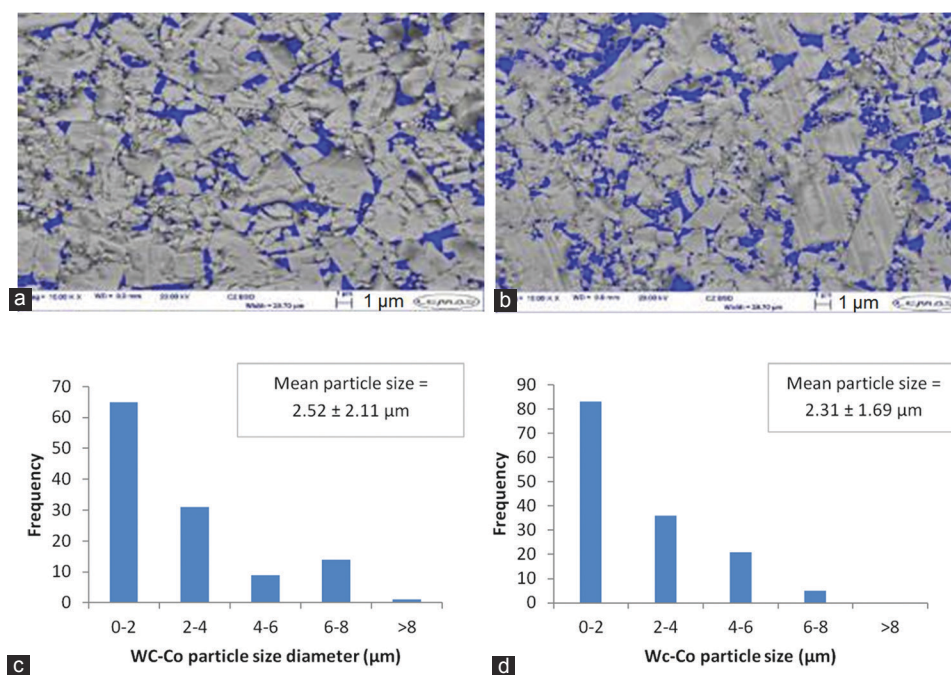


Fig. 6. (Top) BSD images (a) sample M1313, (b) sample K1908 of the substrate layer displaying the tungsten-carbide particles (gray) and the cobalt (blue), (bottom) substrate grain size distribution, (c) Specimen M1313, and (d) specimen K1908.

For the substrate layer, the hardness of the tungsten-carbide layer of sample M1313 is found to be higher than sample K1908 as shown in Table II, and this is attributed to the difference in the cobalt content of the substrate for the two PDC cutters. The cobalt mass weight percentage in sample M1313 is near 7%, whereas sample K1908 has cobalt content of about 9%. The mean grain size of samples M1313 and K1908 is very similar.

C. Microscratch testing

The work presented in this section is focused on quantifying the wear of PDC cutters and the effect of their mechanical properties on the extent of wear. The volume of wear for the PDC cutters was determined experimentally using microscratch and later from nanoscratch tests on different layers of PDC cutters, that is, the diamond layer and tungsten-carbide (substrate layer) by implementing an approach based on the geometry of the removed material after the tests. In addition, this section illustrates how the experimental wear is compared to the predicted wear based on current approaches in the literature. Various wear models are evaluated for micro- and nano-scratch tests on both layers of the PDC samples: Substrate and diamond.

The scratch caused by a sharp indenter produces abrasion wear that would be crucially important for wear mechanism and evaluation. A series of microscratch tests were carried out by applying various loads on the surface of the material and moving the probe to a sufficient sliding distance to produce a scratch. Scratch length and width are the most points of interest for evaluating the wear of the material.

The microscratch tests were performed using an INSTRON 5566 mechanical testing machine and a diamond indenter.

Vickers and spheroconical diamond indenters were used during the microscratch tests on both layers of the PDC samples. The obtained microscratches were examined by SEM, EDX, 2D Talysurf, and three-dimensional interferometer to determine the scratches width and depth as well as for analytical study.

A series of microscratch tests using a Vickers indenter were conducted on both layers of the PDC specimens under various loads. The samples were mounted on an anvil that has a manual controller to alter the sliding distance, whereas the applied load was kept constant. The substrate of the PDC sample was scratched using loads ranging 100-300 N. Measured wear from microscratch tests was compared to the predicted wear based on models in the literature.

The height of the scratch is measured by the 2D profilometer. Careful measurements were carried out using Ultra Precision Talysurf PGI800 with a resolution up to 0.8 nm.

The volume of wear (V_w) is determined experimentally from the geometry of the removed material using the following equation:

$$V_w = \frac{w_s \cdot h_s}{2} X \quad (1)$$

Where w_s is the width of the scratch and is measured by image analysis of SEM records, X is the sliding distance, and h_s is the height of the scratch.

Special care was taken in scratching the surface of the diamond layer, where low loads 10 N-20 N were applied to avoid wrecking the tip of the indenter due to the high resistance of the material surface and a high degree of asperities.

Measured wear from microscratch test is compared to the predicted wear based on approaches in the literature by Rabinowicz (1996), Hutchings (1992), and Ning and

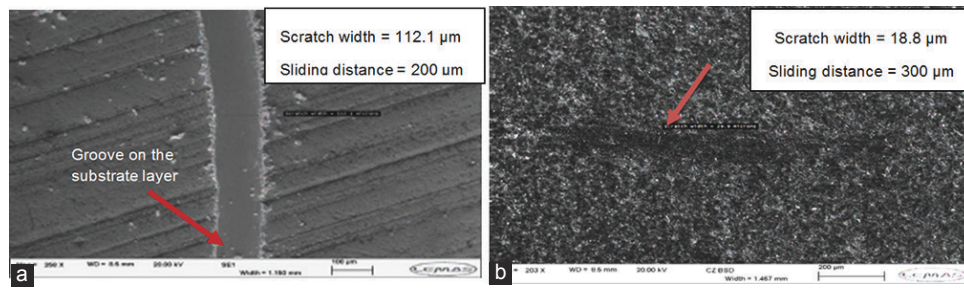


Fig. 7. (a) Groove obtained using a spheroconical indenter at 50 N load on WC-Co, (b) scratch obtained using a spheroconical layer at 10 N on the diamond layer.

Ghadiri (2006) as described by Equations (2), (3), and (4), respectively:

$$V_w = \frac{F \cdot \tan(\beta) \cdot X}{\pi \cdot H} \quad (2)$$

$$V_w = \frac{2F \cdot X}{\pi \cdot H \cdot \tan(\alpha)} \quad (3)$$

$$V_w = \frac{0.07F^4}{K_c \pi^4 H^4} \left(2L + \frac{\pi^{\frac{1}{4}} H^{\frac{1}{4}} F^{\frac{3}{4}}}{17.1K_c} \right) \quad (4)$$

Where F is the applied load (N), X and L are the sliding distances (m), β is the abrasion angle (degrees), H is the hardness of the softest or abraded material (N/m^2), α is the half angle of the abrasive particle (degrees), and K_c is the fracture toughness of the material ($MPa \cdot m^{1/2}$).

Due to the high risk of wrecking the diamond indenter, especially when conducting the micro- and nano-scratch testing on the diamond layer of the PDC samples, additional scratch tests were performed using spheroconical indenter. The use of a spherical tip of the probe is an effective way to reduce the risk of breakage as compared to the use of sharp indenters, particularly when scratching hard coatings (Beake, et al., 2011).

Fig. 7a shows the produced groove after applying 50 N on the tungsten-carbide-cobalt (WC-Co) layer of sample K1908 using spheroconical indenter. The scratch width and sliding distance were 112.1 μm and 200 μm , respectively, whereas Fig. 7b illustrates a scratch obtained after applying 10 N on the diamond layer of sample K1908. The scratch width and sliding distance were 29.9 μm and 2300 μm , respectively. The SEM images showed that the debris resulted from the ploughing action due to the microscratching of sample K1908.

The wear produced using spheroconical indenter from microscratch and later nanoscratch test is determined from the following equation which is found to quantify the wear volume of the x-track as follows (CSM Ltd., 2002):

$$V_w = A_{segment} \cdot L \quad (5)$$

Where $A_{segment}$ is the area of the circular segment as seen from Fig. 8 and could be determined from the following equation:

$$A_{segment} = \frac{1}{2} \cdot R^2 \cdot [\theta - \sin\theta] \quad (6)$$

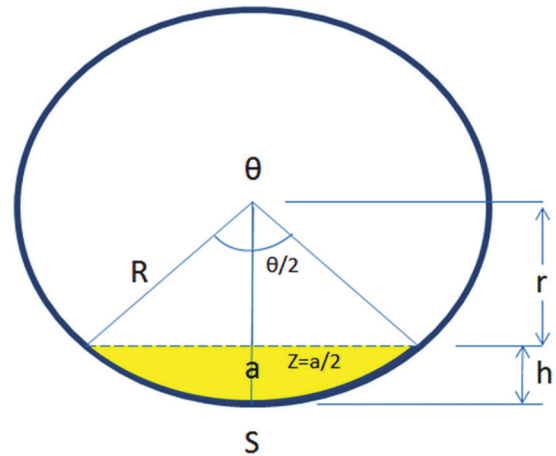


Fig. 8. Sketch of the circular segment of the conical tip that indents the diamond layer.

Where θ is the angle opposing the segment of the circle, and it can be computed from Equation (8):

$$\theta = 2 \cos^{-1} \left(1 - \frac{h}{R} \right) \quad (7)$$

Where R is the radius of the circle and h is the residual depth of the micro- or nano-scratch as shown in Fig. 8.

D. Nanomechanical testing

Nanomechanical testing is a technique that has been used recently for the evaluation of mechanical failure of ceramics and notably the nano-tribological measurements. Nanoscratch testing approach has a preference as it can overcome problems regarding the wreckage of the indenters and the contribution of the machine compliance and surface roughness of the sample (Beake, et al., 2006; 2009; 2013).

In this study, the multiscratch test was conducted on the substrate and the diamond layers of two PDC cutters from different manufactures under specific conditions of fixed load at 500 mN after 200 μm scratch length, loading rate of 20 mN/s, and scratch rate of 10 $\mu m/s$. The Micro Materials Nano Test device has been used for the nanoscratch test. The tip of the spheroconical indenter has a radius of 25 μm . The specimen's surface has been polished before launching the nanoexperiments to minimize surface asperities.

IV. RESULTS AND DISCUSSION

The experimental wear as a result of the microscratch tests using Vickers indenter was compared to the predicted wear from various models as shown in Fig. 9.

It is clearly seen from Fig. 9 that the predicted wear from Hutchings model is the closest to the experimental wear based on Equation (1). Rabinowicz model gave lower wear values than the experimental wear, whereas Ning and Ghadiri model displays higher values than the experimental one. This might be due to the influence of fracture toughness on the equation of Ning and Ghadiri. This finding is applicable for both layers

of the PDC Diamond when Vickers indenter was used to create microscratches on both layers of the PDC inserts.

The obtained wear from nanoexperimental scratch test together with those of microscratch test of the substrate layer for samples K1908 and M1313 is shown in Fig. 10a. It can be seen that the wear of substrate layer for sample K1908 is slightly higher than that of sample M1313.

Similarly, for the diamond layer, wear results obtained from micro- and nano-scratch tests were plotted in Fig. 10b. Similarly, the wear of the diamond layer of sample K1908 is slightly higher than that of sample M1313.

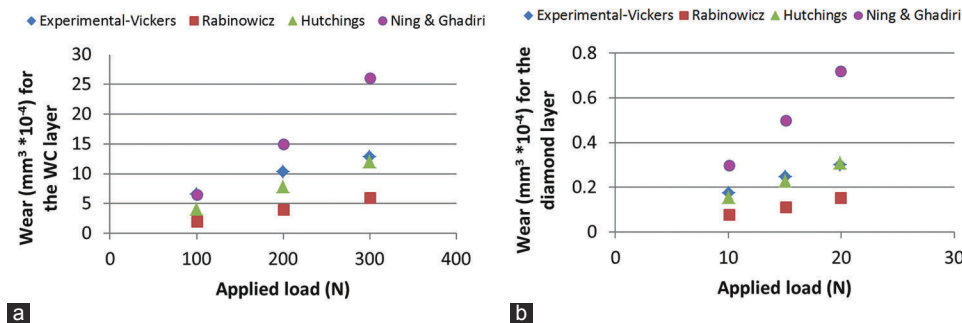


Fig. 9. (a) Wear by various models for the tungsten-carbide layer for sample M1313, (b) wear for various models of wear for the diamond layer for sample M1313.

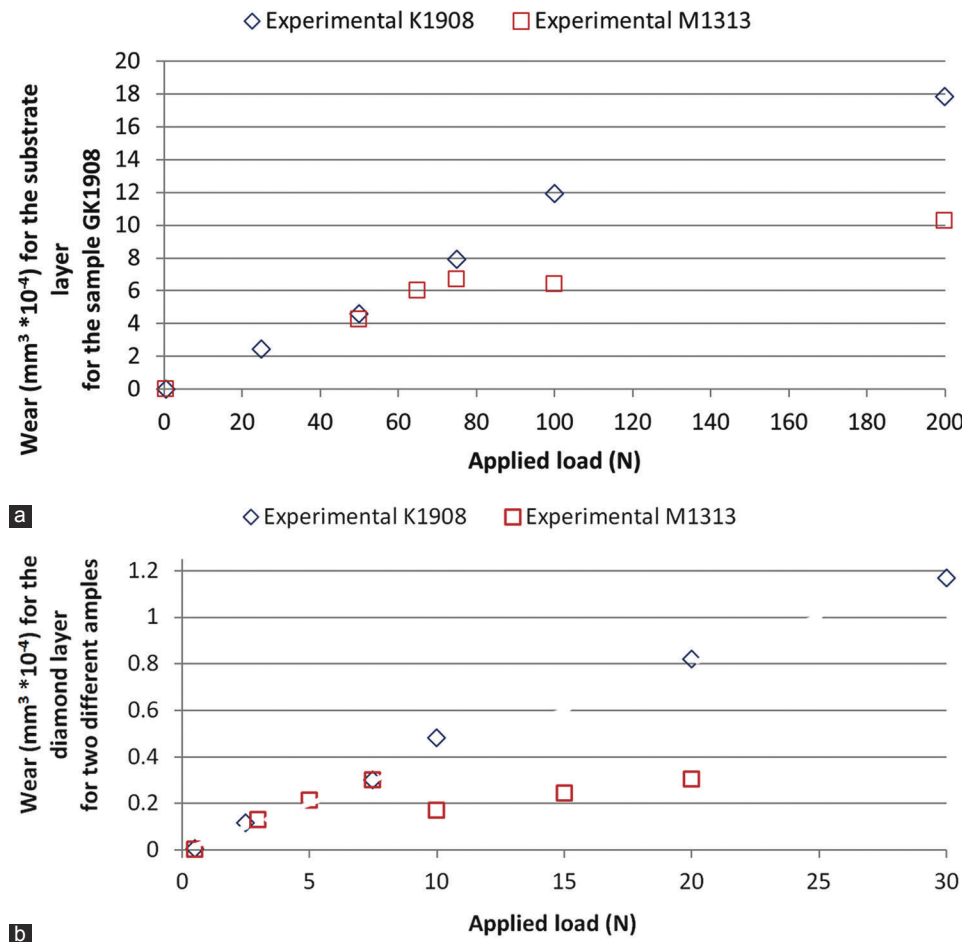


Fig. 10. (a) Experimental wear for the substrate layer of samples K1908 and M1313, (b) experimental wear for the diamond layer of samples K1908 and M1313.

V. CONCLUSIONS

The material properties and wear tendencies of both layers (diamond and substrate) of two PDC bit cutters from different manufacturers (samples M1313 and K1908) were studied using micro- and nano-test techniques. Hardness of the diamond layer of sample M1313 found to be greater than that of the sample K1908. This is mainly due to a lower level of cobalt content in sample M1313 (3.26%) compared to that of sample K1908 (4.4%) as well as slightly smaller grain size of sample M1313 (12.03 μm) compared to that of sample K1908 (12.73 μm).

For the substrate layer, the hardness sample M1313 is found to be higher than that of sample K1908 attributed mainly to the difference in the cobalt content of the substrate of the two PDC cutters. In this work, the wear of PDC samples has also been assessed using micro- and nano-scratch techniques. The tests were carried out on both layers of PDC samples. The results suggest that sample M1313 has higher wear resistance than sample K1908. This is attributed to a higher hardness of sample M1313 as compared to sample K1908 which is a result of different binder (cobalt) content and grain sizes.

Furthermore, the quantitative results suggest that wear of each sample is proportional to the applied force and sliding distance and inversely to the hardness of the material, according to the model of Archard.

It was shown that all the data for both samples can be unified on a curve considering the three parameters mentioned above (load, sliding distance, and hardness), suggesting that wear tendency of samples could be predicted based on the mechanical properties, notably hardness.

The findings of this study could be applied to various types of PDC cutters from different manufacturers to evaluate the intensity of wear as a quality index rather than using the previous traditional abrasion tests.

Nomenclature

$A_{segment}$: Area of the circle's segment (μm^2 , nm^2)

Co : Cobalt (binder)

CED : Circular equivalent diameter

F : Applied load (mN, N)

$F(A)$: Function in Archard equation

H , H_m : Hardness of the material (N/m^2 , GPa)

H_a : Hardness of the abrasive (N/m^2 , GPa)

H : Residual depth (nm, μm)

h_s : Scratch height (μm)

K : Constant for the system or wear coefficient

K_C : Fracture toughness of the material ($\text{MPa}\cdot\text{m}^{1/2}$)

N : Index of incremental depth and sliding distance

R : Radius of the circle (nm, μm)

r : Height of the triangle (nm, μm)

SHN : Scratch hardness number (GPa)

V_w : Volume of wear (μm^3 , mm^3)

WC : Tungsten-carbide

w_s : Scratch width (μm)

X , L : Sliding distance (μm)

α : Half angle of the abrasive particle (degrees)

β : Abrasion angle (degrees)

θ : Angle opposing the segment of the circle (degree).

VI. ACKNOWLEDGMENTS

Special word of thanks is given to Dr. Umair Zafar (Postdoc.) in Ghadiri group for his assistance in carrying out nanoscratch tests at the Institute of Particle Science and Engineering at the University of Leeds, UK. Furthermore, the authors must not forget the precious information given by Prof. Ben Beake (Micromaterials, UK) for his help regarding the nanoscratch test.

REFERENCES

- Archard, J.F., 1953. Contact and Rubbing of Flat Surfaces. *Journal of Applied Physics*, 24(8), pp.981-988.
- Beake, B.D., Vishnyakov, V.M., Valizadeh, R. and Colligon, J.S., 2006. Influence of mechanical properties on the nano-scratch behaviour of hard nanocomposite TiN/Si 3 N 4 coatings on Si. *Journal of Physics D: Applied Physics*. 39(7), pp.1392-1397.
- Beake, B.D., Goodes, S.R. and Shi, B., 2009. Nanomechanical and nanotribological testing of ultra-thin carbon-based and MoST films for increased MEMS durability. *Journal of Physics D: Applied Physics*. 42(6), pp.065301.
- Beake, B.D., Harris, A.J. and Liskiewicz, T.W., 2013. Review of recent progress in nano-scratch testing. *Tribology - Materials, Surfaces and Interfaces*. 7(2), pp.87-96.
- Beake, B.D., Shi, B. and Sullivan, J.L., 2011. Nanoscratch and nanowear testing of TiN coatings on M42 steel. *Tribology-Materials, Surfaces and Interfaces*. 5(4), pp.141-147.
- Bellin, F., Dourfaye, A., King, W. and Thigpen, M., 2010a. The current state of PDC bit technology. *World Oil*. 9, pp.53-58.
- Bellin, F., Dourfaye, A., King, W. and Thigpen, M., 2010b. The current state of PDC bit technology. *World Oil*, 2010, pp.41-46.
- Bellin, F., Dourfaye, A., King, W. and Thigpen, M., 2010c. The current state of PDC bit technology. *World Oil*, 2010, pp.67-71.
- Couvy, H., Lahiri, D., Chen, J., Agarwal, A. and Sen, G., 2011. Nanohardness and Young's modulus of nanopolycrystalline diamond. *Scripta Materialia*. 64(11), pp.1019-1022.
- CSM Instruments., 2002. *Overview of Mechanical Testing Standards*. Available from: http://www.csm-instruments.com/en/webfm_send/42. [Last accessed on 2015 Jun 29].
- Dubrovinskaia, N., Dub, S., Dubrovinsky, L., 2006. Super wear resistance of aggregated diamond nanorods. *Nano Lett*. 6(4), pp.824-826.
- Fang, Z., Griffo, A., White, B., Belnap, D., Hamilton, R., Portwood, G.P., Cox, P., Hilmas, G. and Bitler, J., 2001. Chipping resistant polycrystalline diamond and carbide composite materials for roller cone bits. In: The SPE Annual Technical Conference and Exhibition. New Orleans, Louisiana, USA.
- Geoffroy, H., Minh, D.N., Bergues, J. and Putot, C., 1999. Interaction between Rock and Worn PDC Bit: Theory and Experiments. In: The 9th International Society for Rock Mechanics Congress. Paris. France.
- Hutchings, I.M., 1992. *Tribology: Friction and Wear of Engineering Materials*. Edward Arnold, London.
- Mori, N., Moriguchi, H., Ikegaya, A., Shioya, Y. and Ohbi, K., 2003. Development of Highly Durable Materials for Drilling Hard and Abrasive Rocks. In: The SPE Asia Pacific Oil and Gas Conference and Exhibition. 15-17 April 2003, Jakarta. Indonesia.
- Mouritz, A.P. and Hutchings, I.M., 1991. The Abrasive Wear of Rock Drill Bit Materials. Society of Petroleum Engineers, Paper SPE 24222.
- Ndlovu, S., 2009. The wear properties of Tungsten Carbide-Cobalt Hardmetals from the Nanoscale up to the Macroscopic Scale. A PhD Dissertation Submitted

to the Materials Science and Engineering, University of Erlangen-Nuremberg, Germany.

Ning, Z. and Ghadiri, M., 2006. Distinct element analysis of attrition of granular solids under shear deformation. *Chemical Engineering Science*. 61(18), pp.5991-6001.

Osipov, A.S., Bondarenko, N.A., Petrusha, I.A. and Mechnik, V.A., 2010. Drill bits with thermostable PDC inserts. *Diamond Tooling Journal*. 70(625), pp.31-34. Available from: http://www.dtj-online.com/userfiles/file/Vol70Num625_31-34.pdf. [Last accessed on 2012 Sep 16].

Rabinowicz, E., 1996. *Friction and Wear of Materials*. 2nd ed. John Wiley and Sons, Toronto, ON.

Richardson, R.C., 1968. The wear of metals by relatively soft abrasives. *Wear*. 11(4), pp.245-275.

Sumiya, H. and Irifune, T., 2004. Indentation hardness of nano-polycrystalline diamond prepared from graphite by direct conversion. *Diamond and Related Materials*. 13(10), pp.1771-1776.

Tze-Pin, L., Hood, M., Cooper, G. and Xiaohong, L., 1992. Wear and failure mechanisms of polycrystalline diamond compact bits. *Wear*. 156(1), pp.133-150.

Yahiaoui, M., Gerbaud, L., Paris, J.Y., Denape, J. and Dourfaye, A., 2013. A study on PDC drill bits quality. *Wear*. 298-299, pp.32-41.

Zacny, K. 2012. Fracture and fatigue of polycrystalline-diamond compacts. *SPE Drilling and Completion* 27, pp.145-157.

A Hybrid of Artificial Bee Colony, Genetic Algorithm, and Neural Network for Diabetic Mellitus Diagnosing

Tarik A. Rashid^{1,3}, Saman M. Abdullah^{2,4}

¹Department of Science and Engineering, University of Kurdistan Hewler, Erbil, Kurdistan Region – F.R. Iraq

²Department of Software Engineering, Faculty of Engineering, Koya University, Kurdistan Region – F.R. Iraq

³Department of Software and Informatics Engineering, Salahaddin University, Erbil, Kurdistan Region – F.R. Iraq

⁴Department of Computer Engineering, Ishik University, Erbil, Kurdistan Region – F.R. Iraq

Abstract—Researchers, widely have introduced the artificial bee colony (ABC) as an optimization algorithm to deal with classification and prediction problems. ABC has been combined with different artificial intelligent techniques to obtain optimum performance indicators. This work introduces a hybrid of ABC, genetic algorithm (GA), and back propagation neural network (BPNN) in the application of classifying and diagnosing diabetes mellitus (DM). The optimized algorithm is combined with a mutation technique of GA to obtain the optimum set of training weights for a BPNN. The idea is to prove that weights' initial index in their initialized set has an impact on the performance rate. Experiments are conducted in three different cases; standard BPNN alone, BPNN trained with ABC, and BPNN trained with the mutation based ABC. The work tests all three cases of optimization on two different datasets (primary dataset and secondary dataset) of DM. The primary dataset is built by this work through collecting 31 features of 501 DM patients in local hospitals. The secondary dataset is the Pima dataset. Results show that the BPNN trained with the mutation based ABC can produce better local solutions than the standard BPNN and BPNN trained in combination with ABC.

Index Terms—Artificial Bee Colony, Artificial Neural Networks, Diabetic Mellitus, Evolutionary Algorithms.

I. INTRODUCTION

Artificial neural network (ANN) is an information processing paradigm that simulates the nervous system of the human brain and its cognitive processes. The key features of

an ANN (Priddy and Keller, 2005) are pliability, competence, capacity to simplify, and resolve categorization difficulties, and determining similarity in patterns. ANNs, and their training algorithms have become increasingly important for modeling and optimization in many fields of science and engineering. Among many different ANN models, BP-based trained ANN as a multi-layer structure has been widely utilized rather than other training types due to its great capability in-universe approximation and optimization (Nawi, et al., 2010). Nevertheless, BP-based ANN suffers from a low convergence rate and instability; this would be triggered through falling in local optimum solutions (Karaboga, et al., 2014). For that reasons, numerous procedures for optimizing and enhancing the learning method of the BP-based ANN (Nawi, et al., 2011). In the direction of that end, different global search algorithms have been involved to optimize the weights that initialize a BP trained with Artificial bee colony (ABC) and genetic algorithm (GA) (Nawi, et al., 2014). The idea of searching in ABC, and GA is different. ABC is searching for the best solution among a set of populations through an updating process. The important activities of ABC are to share the indexes of the provided solutions, which are known as food sources. This process in the ABC is called information sharing (Karaboga, et al., 2014; Akay and Karaboga, 2015). However, a typical ABC cannot do this sharing efficiently. Although GA, which also has some populations, can provide efficient index sharing, the process of updating sources has no relation with the learning rate as found in ANN and ABC. GA is just using crossover among the population to get new offspring (Kumar and Verma, 2012). A recent article (Nawi, et al., 2010) surveyed two decades of research and showed that there are numerous ways to search for an optimization of an ANN. It shows that the simplest and best way are to optimize through weight updating. The article also presents different methods for weight updating, because we have found no previous published research on this topic. There are many works utilized different optimization methods in different fields. The most popular methods are practical swarm optimization, ant colony optimization, bacterial foraging optimization, evolutionary algorithm, and GA. In some studies, ABC

ARO-The Scientific Journal of Koya University
Volume VI, No.1(2018), Article ID: ARO.10368, 10 pages
DOI: 10.14500/aro.10368

Received 02 January 2018; Accepted 20 May 2018

Regular research paper: Published 13 June 2018

Corresponding author's, e-mail: tarik.ahmed@ukh.edu.krd

Copyright © 2018 Tarik A. Rashid, Saman M. Abdullah. This is an open-access article distributed under the Creative Commons Attribution License.



outperforms other methods (Karaboga, et al., 2014; Nawi, et al., 2011).

The objective of this article is to combine the mathematical calculation of ABC and the crossover technique of GA to generate a new initialized weights' set that can increase the efficiency of back propagation neural network (BPNN) training and learning. We then apply the proposed approach to the process of diagnosing diabetes mellitus (DM) cases.

The rest of paper is organized as follows: Section 2, describes clinical and soft classification of DM, next, BPNN is presented, in Section 4, nature-inspired algorithm is introduced, then ABC is defined in Section 6, then, GA is explained, followed by an explanation of ANN training with Mutated ABC, in Section 8, details of experimental results are presented, and finally, the key points are concluded.

II. CLINICAL AND SOFT CLASSIFICATION OF DM

DM is a chronic disease in which a patient's body is unable to produce or unable to properly use and store glucose. It is a lifelong condition that affects the body's ability to efficiently use the energy found in food. As of 2014, an estimated 387 million people have diabetes worldwide. From 2012 to 2014, diabetes is estimated to have caused 1.5–4.9 million deaths each year. The number of people with diabetes is expected to rise to 592 million by 2035. The global economic cost of diabetes in 2014 was estimated to be \$612 billion USD (Federation, 2014).

This disease has many types and forms; however, the most popular types are Type 1 (known as insulin-based DM) and Type 2 (known as noninsulin-based DM) (Wild, et al., 2004). Physician must define the type of DM a patient has so that proper medications can be given and so that patients can be instructed on how to minimize side effects of the disease. Recently, many soft computing models have been built to diagnose and classifying DM cases into either Type 1 or Type 2. Some soft models can predict the rate of glucose in the blood for DM patients based on various predictors. One of the most popular soft computation tools that utilized for DM distinguisher is ANN (Association, 2014).

III. BPNN

BPNN is one of the most effective ANN supervised learning algorithms. It causes an ANN to learn through the process of minimizing errors at the output layer's neurons. Errors in the hidden layer of any BPNN can also be minimized based on the rate of errors in the output layer. This computation is the core fundamental of the learning process in any BP-based ANN structure. Through this process, a BPNN calculates and adjusts the weights utilizing gradient descent method (Atakulreka and Sutivong, 2007; Dai and Liu, 2012; Ojha, et al., 2016; Ojha, et al., 2017). Through this weights adjustment, BPNN can minimize the error rate at the output layer. Errors at the output layer correspond to the sum of the squares of the errors recorded between the actual and desired outputs, as indicated in Eq. (1).

$$E_p = \sum_{i=1}^j (d_i - y_i)^2 \quad (1)$$

In (1), d is the desired output and y is the actual output. E represents the total sum of errors that can be obtained for the P pattern, whereas i is the i^{th} neuron and j is the number of the output neuron. BPNN uses the Gradient Descent method as indicated in Eq. (2), to minimize the rate of E_p .

$$W_{ki} = -\mu \frac{\partial E_p}{\partial W_{ki}} \quad (2)$$

The variable in Eq. (2), is the weight located between the i^{th} neuron of the $n-1$ layer, and k^{th} neuron in the n layer. The output layer errors ∂_o , and the hidden layer errors ∂_i can be obtained using Eq. (3) and (4), respectively.

$$\partial_o = \mu (d_i - y_i) f'(y_i) \quad (3)$$

$$\partial_i = \mu \sum_j \partial_j W_{ij} f'(y_i) \quad (4)$$

Based on the error rates that obtain in both hidden and output layers, weights can be adjusted to calculate new weights, using Eq. (5) at the hidden layer, Eq. (6) at the output layer, and Eq. (7) for updating the bias values.

$$W_{ij}(K+1) = W_{ij}(K) + \mu \partial_o y_i \quad (5)$$

$$W_{ij}(K+1) = W_{ij}(K) + \mu \partial_i y_i \quad (6)$$

$$b_i(K+1) = b_i(K) + \mu \partial_i \quad (7)$$

In the past three equations, K is the number of epochs and μ is the learning rate. These equations are the core of learning for any BP based NN structure. The learning is the process of updating the weight values that connecting layers through existing neurons (Atakulreka and Sutivong, 2007; Dai and Liu, 2012; Ojha, et al., 2016; Ojha, et al., 2017). The new value of any weight depends on the learning rate and the rate of errors computed in the neurons of the output layer. The value of the learning rate is simply a fixed number between (0, 1), and the value that initializes each weight laid between neurons of two layers is chosen randomly between (-1, +1). With such initialization of the learning rate and the weight values, PBNN falls into local minima.

IV. NATURE INSPIRED ALGORITHM

These are swarm intelligence and bio-inspired algorithms that would form a hot topic in the expansions of new algorithms inspired by nature (Karaboga, et al., 2014; Nawi, et al., 2014; Akay and Karaboga, 2015; Kumar and Verma, 2012). These are regarded as nature-inspired metaheuristic algorithms that are based on swarm intelligence, biological, physical, and chemical organizations. As a result, these algorithms can be called swarm-intelligence-based, bio-inspired based, physics-based, and chemistry-based, reliant on the foundations of stimulation. It can be said that not all of these different algorithms are effectual and successful (Karaboga, et al., 2014; Nawi, et al., 2014; Akay and Karaboga, 2015; Kumar and Verma, 2012). Some of these algorithms have established to be extremely good, consequently, they have become frequently implemented and modified for solving real-world problems. Although

the research in this area of interest is very dynamic and self-motivated purely for the reason that problems with which researchers and scientists are typically conscious are becoming progressively complex because of size and other aspects. Moreover, recent problems are gathering up constantly on which existing approaches are not dynamic. This gives us the awareness that the Nature Inspired Algorithms and Swarm Intelligence techniques have been there for researchers and scientists in various fields and finalized it for them. That is why now and in the foreseeable future, we need to look as if to attain loads of inspiration from these nature-inspired algorithms. Current Nature-Inspired Algorithms would cover the ABC Algorithm, the Bat Algorithm, and many others (Karaboga, et al., 2014; Nawi, et al., 2014; Akay and Karaboga, 2015; Javadi, et al., 2010; Gen, and Cheng, 1997). The above algorithms have been very fruitful in terms of solving various applications, if they are gaged against initial Nature-Inspired Algorithms such as the GA and others (Gen, and Cheng, 1997). Besides, some of them, for instance, the GA, would have very few parameters that can be randomly set (Kumar and Verma, 2012). We also need to be watchful, since the number of new nature-inspired algorithms is receiving greater. This will make it very difficult for researchers, scientists, and users to select appropriate algorithms for solving their applications. Thus, it is imperative to step back and see the differences among these algorithms, and how they are related to each other. It can be seen that some of these algorithms are nothing more than a reuse of prior optimization ideas. It is worth saying that this problem will bring us to an action plan to be taken by researchers and scientists in general and the action plan is to make a list and group these algorithms, or maybe list out these algorithms in terms of how these algorithms are constructed, their performance, precision, computation complexity, memory, and power usage, etc.

V. ABC

ABC is a population-based optimization algorithm that tries to achieve global minimum (Karaboga, et al., 2014; Akay and Karaboga, 2015). It is a stochastic optimization algorithm that mimics the foraging behavior of the honeybee. Solutions in this algorithm have multi-dimensional search space, which is represented as a food source. Only three types of bees (employed, onlooker, and scout) can maintain the solutions that are given by ABC algorithm. Scout bees will locate the best food source. They will then return to the hive, where other bees onlookers will be recruited to the food source for collection. At this point, the bees are now "employed" in the collection of the food source. By analogy, the fundamental idea of the ABC algorithm is for an agent to look for the best solution. It starts by selecting a random solution among existing space of possible solutions; after that, it continues attempting to find better solutions, while also abandoning the unpromising ones. The iteration of the ABC stops when it reaches either the maximally optimal solution or if or no better suboptimal solution can be found.

The ABC starts with initializing the solutions randomly, as indicated in Eq. (8). Then, the new food source location is updated and obtained by Eq. (9).

$$x_{i,j} = x_{min,j} + rand[0,1] \times (x_{max,j} - x_{min,j}) \quad (8)$$

Where:

$i = 1, 2, \dots, N$ and $j = 1, 2, \dots, D$.

$x_{i,j}$ is the parameter to be optimized for i^{th} employ bee, N is the employ bee number.

D is the dimensional size of solution. j is the associated solution in D space with the i^{th} employ bee.

$x_{max,j}$ and $x_{min,j}$ are the upper and lower bound for the .

$$v_{i,j} = x_{i,j} + \phi(x_{i,j} - x_{k,j}) \quad (9)$$

In Eq. (9), $x_{i,j}$ is the i^{th} employed bee, and $v_{i,j}$ is the new solution for the $x_{i,j}$. $x_{k,j}$ is a neighbor bee for the $x_{i,j}$. ϕ is selected randomly $[-1,1]$. $j \in \{1, 2, \dots, D\}$ and $k \in \{1, 2, \dots, N\}$ selected randomly.

The new food position (solution) will be memorized in an onlooker for one of the n employers, based on the result of the fitness function. The detailed pseudo-code for the ABC algorithm is given below:

Step-1: Initialize the population of solutions $x_{i,j}$, $i = 1..N$, and $j = 1..D$

Step-2: Evaluate the population

Step-3: iteration=1

Step-4: repeat

Step-5: Produce new solutions $v_{i,j}$ for the employed bees using (9) and evaluate them

Step-6: Calculate the fitness values for the solutions $x_{i,j}$

Step-7: Produce the novel solutions $v_{i,j}$ for the onlookers from the solutions $x_{i,j}$ selected depending on the evaluation or fitness function

Step-9: if occurs, control the scout's uncontrolled solution and randomly exchange that with a novel $x_{i,j}$ solution.

Step-10: Keep the optimal solution attained until now.

Step-11: iteration=iteration+1

Step-12: while waiting for iteration that is equal to maximum iteration number (MIN).

VI. GA: MUTATION OR SWAPPING PROCESS

GA is a method for moving from one population to a new population using a kind of "natural selection" or inspired operators of selection, crossover, and mutation. These three rules are involved in each iteration for producing new individuals for future generations. After selecting an individual, GA uses two rules for creating the next generation. The first rule is a crossover, where new generation comes from a combination of two parents. The second rule is a mutation in which a parent will be reordered to get new generation. The last rule creates random changes on a parent to generate a new child. In most cases, it swaps an element or elements in the parent set. Sometimes, the mutation is only a reordering already existing element.

The number of elements involved in the swapping process affects the time complexity of the process. Involving many elements decreases the complexity measure. However, involving many elements in a swap, on the other hand,

decreases the possibility rate of the swapping impact on finding the global minima for a problem. This article proposes a window that slides bidirectionally from both sides of the weight's vector to the center. The size of this window will be checked in the coming section so that the perfect number of elements that should be involved in the swapping process can be obtained. Figure 1 shows an example of the process of sliding and swapping elements.

In this example, the window size has been set up on two elements, which means that at each slide two elements will be involved in the mutation or swapping process.

The example above shows a vector with 14 elements. The figure clearly shows the direction of sliding, which starts at both ends of the vector forwarding to the center. Step1-A shows the element at their original positions in the vector. Step 1-B shows that the swapping has occurred. Accordingly, two elements have swapped their positions. At Step 2, the windows have shifted just over one element. Step 3 shows the shifting and sliding process. This step also shows the changes that occurred with the position of elements.

Two crucial factors should be noted. The first is the size of the window, and the second is the window's sliding size. Tests have been done to identify these two factors. The aim of this swapping is to get different sequences of elements within the same vector, which means the change has occurred at the position or the index of each element. This requires placing an element in as many various positions in the same vector as possible. Through different tests, the suitable window's size selected as two, and sliding size is one. The other alternatives, such as two or more, showed two main shortages. The first is duplicating and removing many elements. The second is reducing the possibility of getting a new sequence of elements.

VII. ANN TRAINING WITH MUTATED ABC

The core fundamental of training ANN is presented in Eq. (8). Through this equation, a new set of weights is generated

from the old set based on learning and error rates. ANN with Back-Propagation learning stacks more often with the problem of local minimum through using such a way of weight updating. The reason for facing such a problem is going back to the structure of the ANN or the way that the ANN is trained (Nawi, et al., 2014). To solve this problem, some solutions have been proposed. The most common is using optimum algorithms, which is somewhat time-consuming. Another way is to focus on initialization methods of the weights. An additional method is to train the neural network more than once; each time the neural network will be initialized randomly on different weights. All these methods can help us find the global optimum of the training (Akay and Karaboga, 2015).

The only difference between neural network and other optimization methods is in the means by which of weights are updated. Equations (6) and (9) show two ways of weight updating that are used in ANN and ABC, respectively. The question is how the accuracy of an ANN will be if the network is trained through Eq. (9) instead of Eq. (6)? Another alternative to repeatedly initialize an ANN on different weights is swapping the weights and changing their locations. Thus, within these two processes, the problem of trapping the ANN in the local minima can be solved. Figure-2 shows the process of the training an ANN through these weights updating and relocations in two simple loops. The outer loop is to initialize and update the weights for an ANN using the Eq. (9). Then, if the global minima are not obtained, the mutation or swapping weights will be tested as the inner loop. The size of the weightings set will be defined with the structure definition of an ANN.

The steps below show the pseudo-code of the mutation based ABC optimization for training ANN:

- Step A: Through the predefined structure of the ANN (by which the structure should fit the problem that the ANN is designed for) the size of the initial set (weights) is dynamically defined.*
- Step B: Initializing the ABC algorithm through the steps that are shown in the section of ARTIFICIAL BEE COLONY. Get the first source of weights.*

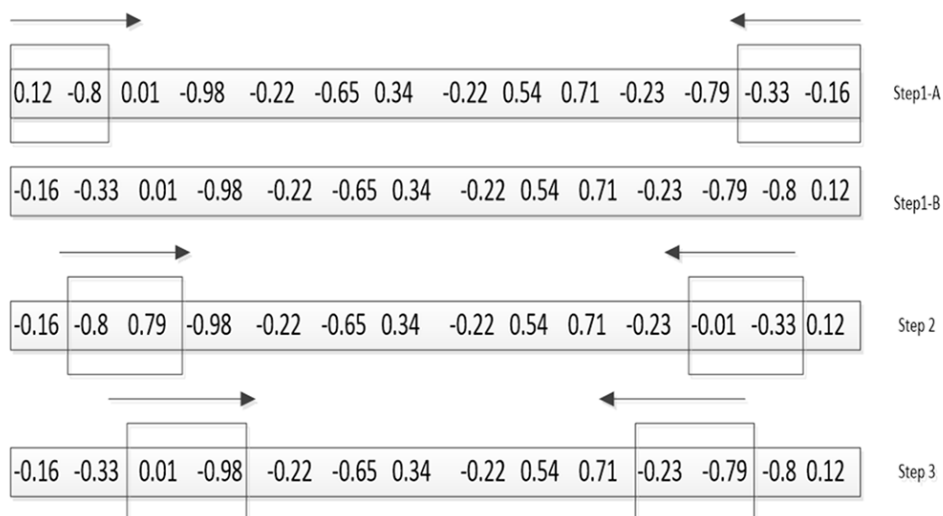


Fig. 1. Sliding and swapping elements.

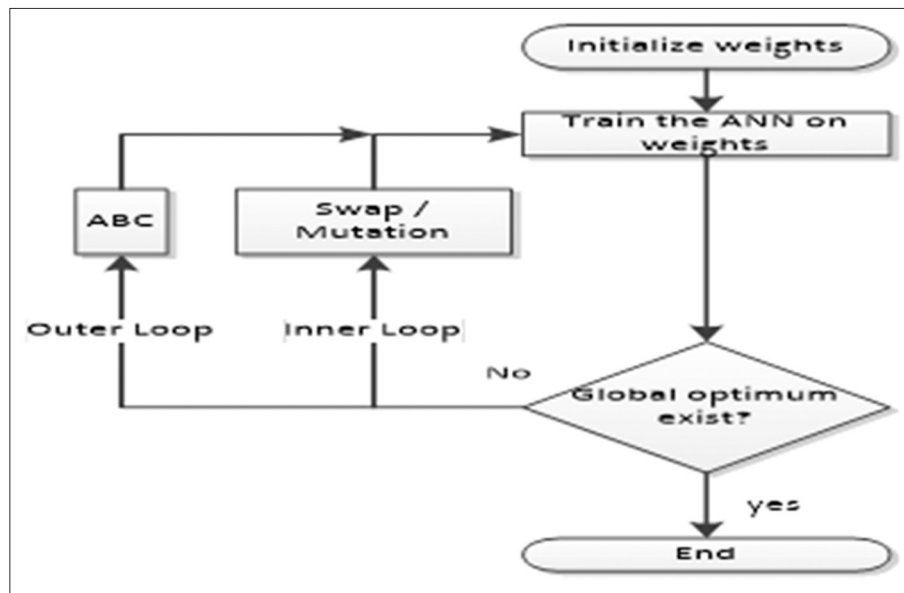


Fig. 2. The process of mutation artificial bee colony training of artificial neural network.

Step C: Do the mutation between the elements in the initial set of weights (get from Step B).

Step D: Initialize the ANN training, validation, and testing.

Step E: Compare the obtained performance with the previous one. Select the best.

Step F: Repeat Step C until no new offspring will be obtained. Repeat the B until no more sources are available.

VIII. SIMULATION AND EXPERIMENTAL WORKS

Various experimental tests are carried out, and details of these can be described as follows:

A. BPNNs

The BPNN has three layers, where they are connected trimly through the neurons that lay at each layer, and the weights that lay between two neurons of two different layers. The first layer is input layer, which the number of neurons there should be equal to the number of the features that are selected as significant for a problem. The subsequent layer is the hidden layer, which enables the BPNN to achieve better performance. The last layer is the output, where the actual output is expected. Fig. 3 shows a typical structure of a BPNN (Ojha, et al., 2017). The structure of the BPNN for both datasets is not the same. For the local dataset, the number of features is 13 (Rashid, et al., 2016); however, for the Pima dataset, the input features are 8 (UCI, Pima India Dataset, 2015).

This means that the input layer for both cases has 13 and 8 neurons, respectively. For both cases, the neurons at the hidden layer are 10 and at the output layer is one. The only difference in both structures is the number of neurons at the input layer. Therefore, the set of initial weights and biases will be different too (151 for local dataset and 101 for Pima dataset). The training function that used by this work is “trainlm” function.

The activate function proposed for neurons in the hidden layer structure is sigmoid function. The neuron at output layer has a linear activate function.

The process of ANN’s training has been tested in three different situations. The first is training ANN normally, which means updating the weights of the ANN per Eq. (6). The second situation is forcing the proposed ANN to update their weights and bias values per Eq. (9), which is the equation that used by ABC algorithm. The last scenario is the same as the second scenario; however, the positions of the initialized weights in the second scenario will be changed (swapped) based on the steps of GA. For all scenarios, the performance indicator measured is calculating the accuracy rate based on the true and false classification rates.

B. Normal Training of BPNN

“Trainlm” is the most common training function used in BPNN. It is also known as the Levenberg-Marquardt optimization algorithm (Priddy and Keller, 2005). The main target of this learning function is to train the network until a goal is achieved through the adjustment of the weights’ values that initialized the network. Through this learning process, the BPNN minimizes the errors that obtained at output layer. The training process of the BPNN terminates immediately when the goal is obtained. However, the obtained goal is not guaranteed to be optimal, as the BPNN depends on gradient descent method. Another factor that terminates the training is the number of failure validation checks. The BP algorithm stops training when the validation check reaches the predefined maximum number. This situation of BP is an indicator of trapping into a local problem, where no performance improvements can be achieved as the training directs the network to the worst situation of learning.

BPNN starts to find solutions from an initial point and continues until the steepest point (a point down toward the

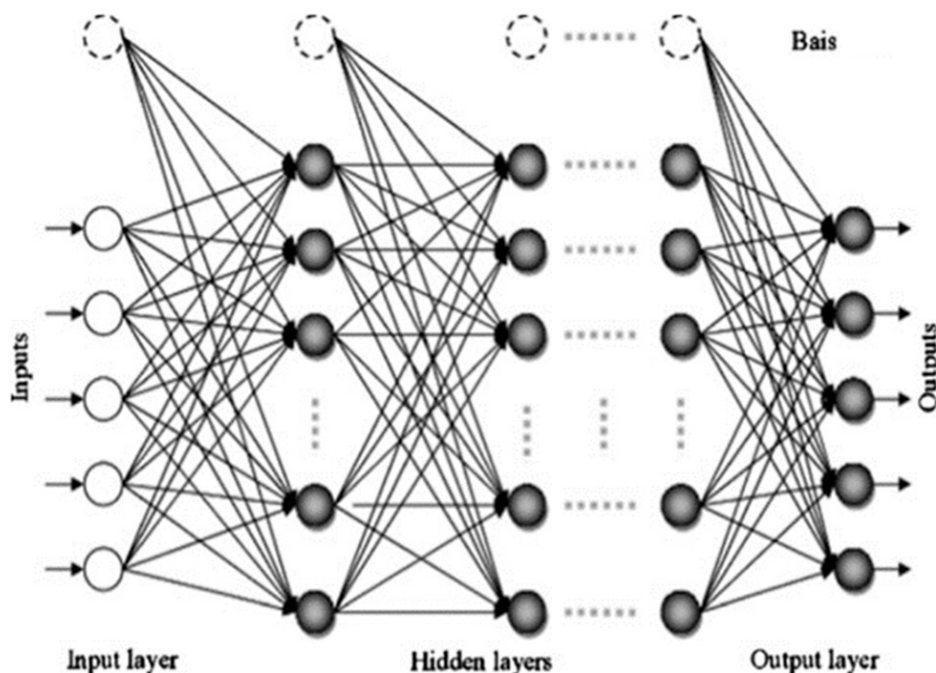


Fig. 3. Typical structure for backpropagation neural network (Priddy and Keller, 2005).

optimum minimization). Two parameters affect the training of the BPNN. The first is called learning rate, in which the value is ranged between zero and one. A small value increases the iteration number, and a large value avoids the BPNN to find the optimum solution. To address that, this work tests the training of the BPNN with two datasets. For each dataset, the network has been initialized with 300 initial sets. Each set has w number of weights and b number of bias values. This work needs to initialize the proposed BPNN 300 times, and each time the initial weights have a different number.

The performance of the BPNN for both dataset and for each set of initial weights will be recorded. Then, the minimum and maximum performance for each dataset will be selected and compared, as shown in Table I. Table 1 also shows the CPU time, which measured by iterations, for both datasets. This performance indicates that the network has found a solution. However, it is not clear whether the solution is optimum. Nevertheless, Fig. 4 makes clear that the no further improvement can be obtained from that solution, as the validation check shows that training is going in the wrong direction. Even more, the gradient degree at the same epoch (iteration = 8) is going up, which confirms trapping the network into a solution where no better solution could be reached.

Fig. 5 shows the performance of a BPNN that normally trained with 300 different sets of the initial weights. The network starts each time training with an initial set of weight and bias values (1×151), which obtained randomly.

Normally, when the BPNN enters the training phase, the values of the weights and the biases will be randomly initialized in the range of $-1, +1$. The figure shows numerous solutions, which obtains when the initial weight has been changed. The figure also explains the impact of the initial weight on the process and the direction of the training phase of the BPNN. This means that the BPNN can achieve better

TABLE I
BPNN PERFORMANCE WITH NORMAL TRAINING

Datasets	Performance (MSE)		CPU time
	Best	Worst	
Pima	0.1324	0.1856	23.2
Local data	0.1298	0.1926	95.4

BPNN: Back propagation neural network

learning if the weights and biases are initialized with proper values. However, the BPNN has no ability to change the initial values of weights and biases after the training phase begins. Therefore, the BPNN cannot change the direction of learning when the network has been initialized with improper values of weights and biases.

To overcome this problem, BPNN should be able to find a proper set of weight and bias values among available alternatives.

Practically, researchers follow the *K-fold* method (Kohavi, 1995) to determine the best solution or the optimal average of the obtained solutions. They run the training phase of a BPNN several times. With each run, the accuracy of the network will be preserved. Then, after *K-fold*, either the best accuracy will be selected or (in most cases) the average of available solutions will be calculated. With such a process, it is not guaranteed that the best solution is the optimum, because there might exist a set of weights and biases that makes BPNN yield higher accuracy than that obtained through the *K-fold* method. Therefore, with such a process there is no guarantee that the best solution found is the optimum solution.

C. ABC based BPNN training

The core of the training in BPNN is updating the weights to minimize errors at the output stage. To achieve this, the set

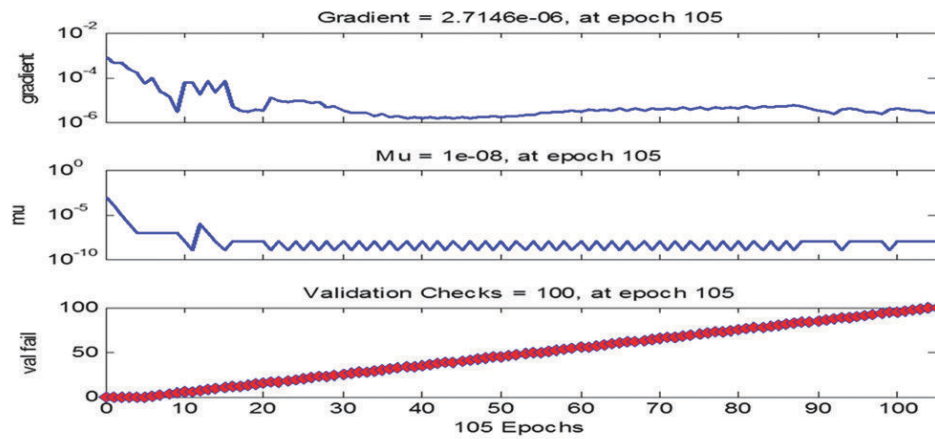


Fig. 4. Failed validation for better solution obtaining.

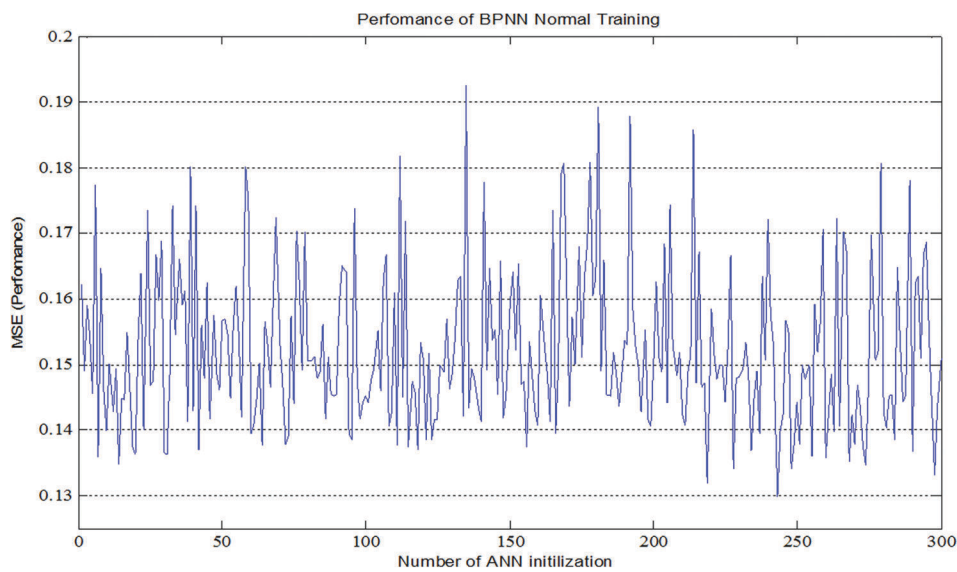


Fig. 5. Performances of normal trained Backpropagation neural (local dataset).

of initialized weights of the network will be updated based on (6). The network uses only one set of initial weights and based on the error rate at the output stage, and the learning rate the new set of weights will be calculated for the next round of training. This means that only one set of weights is utilized in the training process. The idea of involving the ABC algorithm in this work is for utilizing various sources (sets) of weights as initialized weight, where the BPNN can start with. It is a kind of collaboration between these two techniques to find out the perfect set of weights that directs BPNN to find the perfect (optimal) solution. The main changes on the process of the weight updating have been presented in this work, which, are initializing the weight approximately 300 times. As a result, each time the process of updating the weight is going on through the Eq. (9) instead of Eq. (6). Fig. 6 shows the training performance, which becomes more stable than that found in Fig. 5. The local minima solution that obtained through this weight initialization and updating was not found in the obtained performance when the network trained normally.

ABC can serve BPNN with finding the proper set of weights and biases value among the n numbers of the population. However, there is a possibility of getting a better solution than the combination of the BPNN with ABC would do.

All elements in the sets have the same index during training a BPNN with ABC. The question is about the possibility of improving the accuracy of a BPNN when an element with an index of (i,j) can be swapped with another element that has an index $(i+n,j+n)$ when $n \neq 0$.

To test the impact of mutation the weight's indexes on the performance of the BPNN, this article checks the performance of the network with a single set of weights (1×81) for the local dataset. As mentioned in Section 5, the sliding window is shifting by one element each time with doing the mutation on two elements. Accordingly, each single set of weights that have (1×81) dimension can be used to generate 80 different sets that are having the same elements of the mother set. However, in each iteration, the elements will be in different indexes. Fig. 7 shows that a

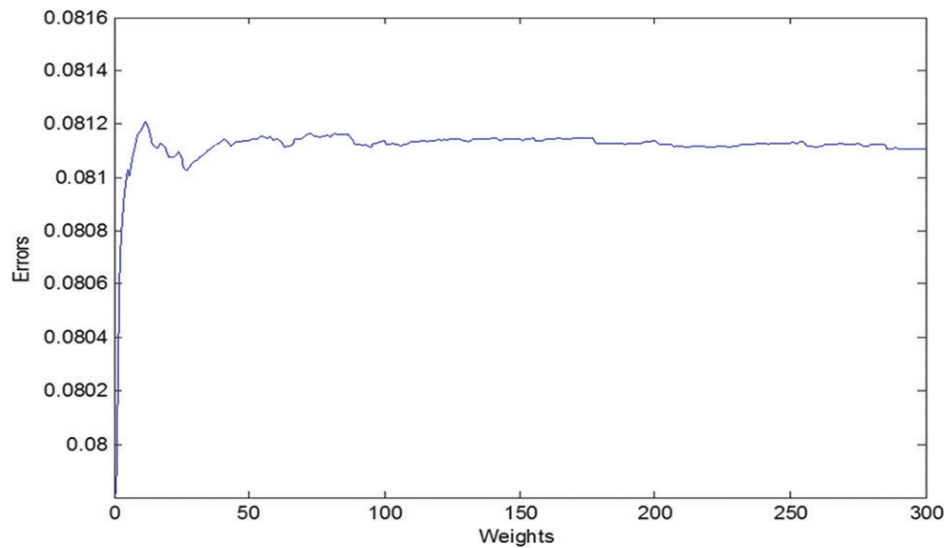


Fig. 6. Backpropagation neural network training based on artificial bee colony source (weights) initializing and updating.

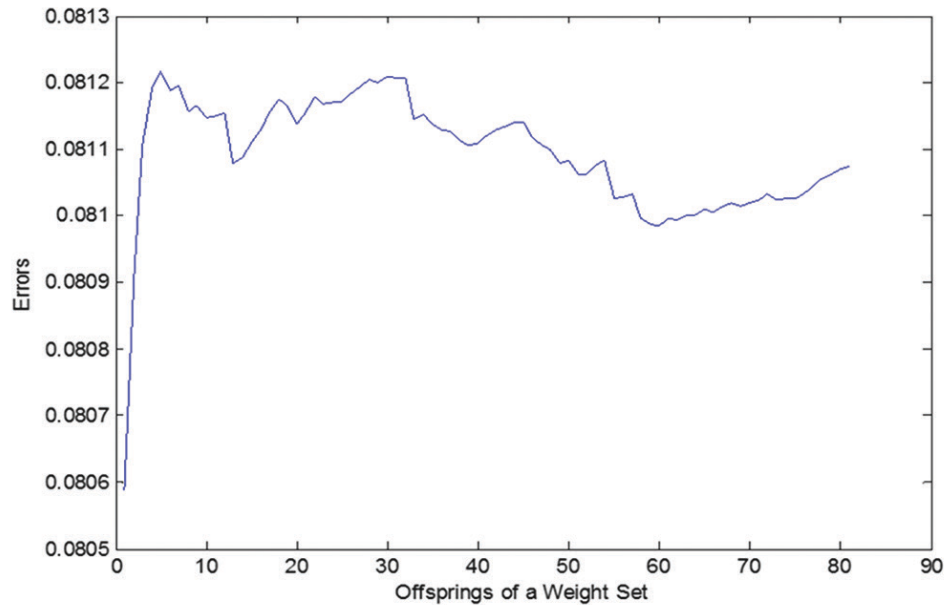


Fig. 7. The 81 offspring of a weight set with different performance.

set of weights can be used to generate different offspring, and with each, the network gives a specific performance. As a set of weights which has been mutated, based on the process explained in Section 5, 81 sets of weights have been obtained. Then, each set has been used to initialize the BPNN. After that, only one observation is used to test the network performance, with a change of offspring on that original set of weights. Results show that different performances have been obtained due to the change of the indexes of the elements inside the set weight just for a single observation. From those performances, and based on the concept of the ABC algorithm, the best performance can be selected as the global minima for that observation.

For the Pima dataset, the above-mentioned procedure and what has been illustrated in Fig. 7 will be repeated. However,

the number of the offspring, in this case, will be 51, as the number of input attributes will be reduced to eight.

Fig. 8 shows the 51 performances that have been obtained for observation with each offspring weight. Considering the locally prepared dataset, the training performance based on 501 local observations can be illustrated as shown in Fig. 9.

This research article assesses the performance of the network with four parameters (CPU time, number of epochs, MSE, and Accuracy) for testing the impact of mutation of the weight's indexes on the performance of the BPNN, the workstation used for the experimentation was equipped with a 2.5 GHz Core-i5 processor and 4-GB of RAM. The simulations are carried out using MATLAB 2013a software. We employed two different data sets to check the impact of the proposed approach of this work on

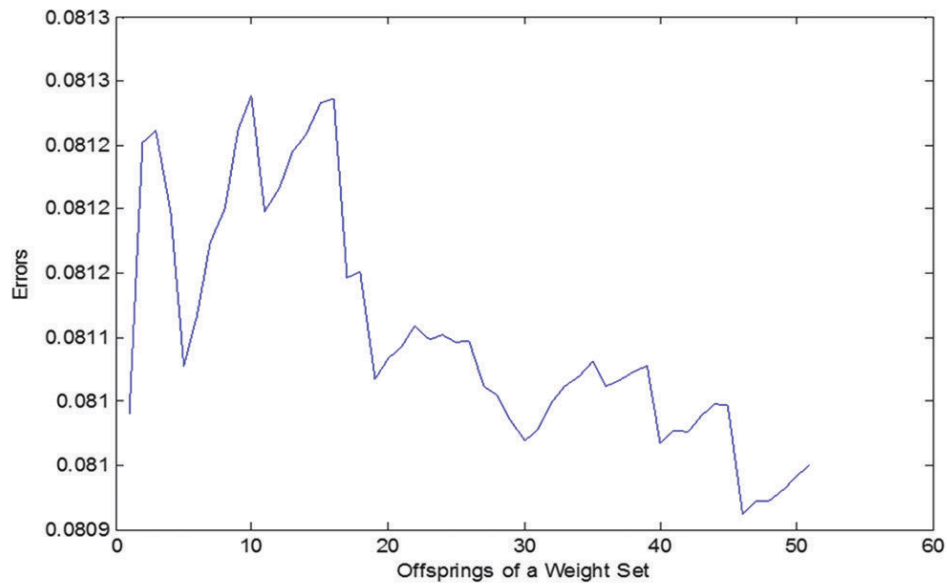


Fig. 8. The 51 offspring of a weight set for Pima dataset with different performances.

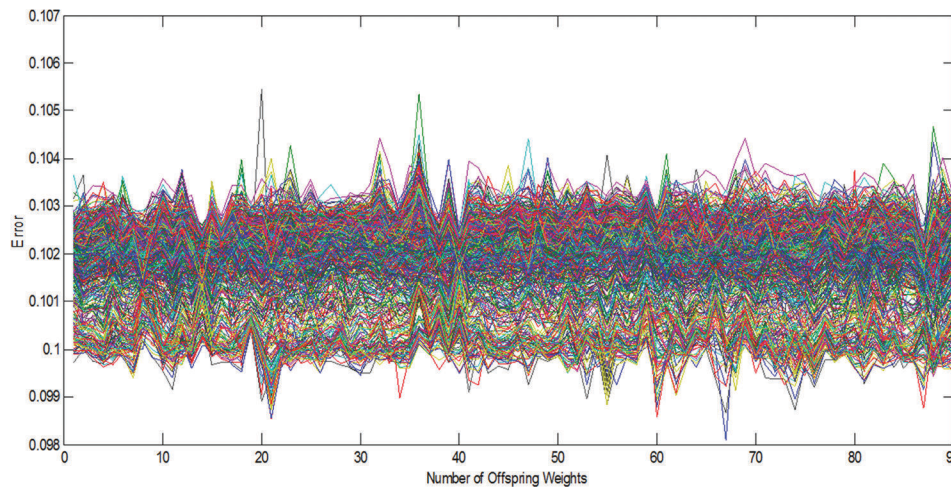


Fig. 9. Network training with 501 observations (each with 91 offspring).

the performance measures. We applied four criteria to three methods: ANN alone, ANN with ABC optimization, and ANN-ABC with weight mutation. Tables II and III show the performance measures of the tests on ANN, ANN-based ABC and ANN-based ABC with weight mutation for both local and Pima datasets, respectively. The tests show that accuracy is improving with the change of weight initialization of the BPNN. The normal initialization cannot improve the accuracy of the trained BPNN within a wide range. The improvement just recorded for a few points of a percent.

IX. CONCLUSION

It is a fact that BPNN can give different performances when initialized with different values of weights. This means that changing the values of weights for a BPNN affects the performance of that network. However, if a network initializes with same values of weights, it gives the same performance

TABLE II
TESTING THE APPROACH WITH LOCAL DATASET

Algorithms/performance measure	ANN	ANN-based ABC	ANN-based ABC with weight mutation
CPU	76.2	123.6	149.4
Epoch	500	1000	1000
Error	0.132	0.0047	0.0013
Accuracy%	93.2	96.11	98.38

ANN: Artificial neural network, ABC: Artificial bee colony

TABLE III
TESTING THE APPROACH WITH PIMA DATA SET

Algorithms/performance measure	ANN	ANN-based ABC	ANN-based ABC with weight mutation
CPU	23.2	95.5	113.1
Epoch	1000	1000	1000
Error	0.197	0.09	0.0045
Accuracy%	89.99	94.77	97.32

ANN: Artificial neural network, ABC: Artificial bee colony

if the training process is repeated for unlimited iterations. The target of changing the weight's values for a network is optimizing the performance (avoiding local optima). Many algorithms have been combined with BPNN, such as ABC, for maximizing the performance. With such algorithms, sets of initial weights are randomly generated, and the best set of weights will be selected based on the best performance obtained. We investigated the impact of the indexes of each weight inside the initialized set on the BPNN performance. Through optimized algorithms, weights are initialized statically (no changes in their indexes have been made). When an index of weight inside the initialized set changes, the performance is also changed, as shown in Figs. 7 and 8 with Tables II and III. This means that there is a possibility of getting better performances if the indexes of weights are changed.

The figures and tables show that initializing weights randomly as done by ANN performs less efficiently and accurately than ANN combined with ABC. However, when the combination of ANN and ABC supported by index sliding of GA, the resulting performance is optimal. It is not the impact of changing the sources (as in the ABC algorithm), it is instead the impact of changing the indexes of the weights too. With such combinations, ABC can force the training process of any BPNN to become more optimal in classification.

Another important problem solved in this article is overfitting of ANN training. We tested the approach with two different datasets, which means the proposed approach is generalized for the different dataset. This also means that our approach overcomes the problem of overfitting.

X. ACKNOWLEDGMENT

The authors would like to thank the editorial office of the journal for reviewing of the manuscript. Furthermore, the authors would like to thank both Mr. Edward Bassett from the English Language Centre (a Juris Doctorate from the University of Missouri-Columbia Law School (USA) and a Master's in Fine Arts (Creative Writing) from the University of Southern Maine (USA) and Mr. Shalaw Najat Ghani (MA in TESOL), from Valparaiso University for their continuous effort in editing the manuscript.

REFERENCES

- Akay, B. and Karaboga, D., 2015. A survey on the applications of artificial bee colony in signal, image, and video processing. *Signal, Image and Video Processing*, 9(4), pp. 967-990.
- American Diabetes Association., 2014. Diagnosis and classification of diabetes mellitus. *Diabetes Care*, 37(Supplement 1), pp. S81-S90.
- Atakulreka, A. and Sutivong, D., 2007. Avoiding local minima in feedforward neural networks by simultaneous learning, in *AI 2007, Advances in Artificial Intelligence*, Springer. Berlin Heidelberg, pp. 100-109.
- Dai, Q. and Liu, N., 2012. Alleviating the problem of local minima in Backpropagation through competitive learning, *Neurocomputing*, 94, pp. 152-158.
- Gen, M. and Cheng, R., 1997. *Genetic Algorithms and Engineering Design*, John Wiley & Sons, New York.
- International Diabetes Federation., 2014. IDf Diabetes Atlas, IDf. International Diabetes Federation. Available from: <http://diabetesatlas.org/resources/2017-atlas.html>. [Last retrieved on 2014 Nov 29].
- Javadi, M.R., Mazlumi, K. and Jalilvand, A., 2011. Application of GA, PSO and ABC in optimal design of a stand-alone hybrid system for north-west of Iran, in *Electrical and Electronics Engineering (ELECO)*, 2011 7th International Conference on, pp. I-203-I-210.
- Karaboga, D., Gorkemli, B., Ozturk, C. and Karaboga, N., 2014. A comprehensive survey: Artificial bee colony (ABC) algorithms and applications. *Artificial Intelligence Review*, 42(1), pp. 21-57.
- Kohavi, R., 1995. A Study of Cross-Validation and Bootstrap for Accuracy Estimation and Model Selection. *Proceedings of the Fourteenth International Joint Conference on Artificial Intelligence*. Vol. 2. Morgan Kaufmann, San Mateo, CA, pp. 1137-1143.
- Kumar, R. and Verma, R., 2012. Classification rule discovery for diabetes patients by using genetic programming. *International Journal of Soft Computing and Engineering*, 2(4), pp. 183-185.
- Nawi, N.M., Ghazali, R. and Salleh, M.N.M., 2010. The development of improved back-propagation neural networks algorithm for predicting patients with heart disease. In: *Information Computing and Applications*, Springer, Berlin. pp. 317-324.
- Nawi, N.M., Ghazali, R. and Salleh, M.N.M., 2011. Predicting patients with heart disease by using an improved back-propagation algorithm, *Journal of Computing*, 3(2), pp. 53-58.
- Nawi, N.M., Rehman, M.Z. and Khan, A., 2014. A new bat based back-propagation (BAT-BP) algorithm, In: *Advances in Systems Science*, Springer, Berlin. pp. 395-404.
- Ojha, V.K., Abraham, A. and Snášel, V. 2017. Metaheuristic design of feedforward neural networks: A review of two decades of research, *Engineering Applications of Artificial Intelligence*, 60, pp. 97-116.
- Ojha, V.K., Dutta, P., Chaudhuri, A. and Saha, H. 2016. Convergence Analysis of Backpropagation Algorithm for Designing an Intelligent System for Sensing Manhole Gases. In: *Hybrid Soft Computing Approaches*, Springer, Berlin, pp. 215-236.
- Priddy, K.L., and Keller, P.E., 2005. *Artificial Neural Networks: An introduction*. SPIE Press, Bellingham.
- Rashid, T.A., Abdullah, S.M., and Abdullah, R.M., 2016. An Intelligent Approach for Diabetes Classification, Prediction and Description, In: Snášel, V., Abraham, A., Krömer, P., Pant, M., Muda, A., editors. *Innovations in Bio-Inspired Computing and Applications. Advances in Intelligent Systems and Computing*, Vol. 424. Springer, Cham.
- UCI. 2015. Pima India Dataset. UCI Machine Learning Repository. Available from: <https://www.archive.ics.uci.edu/ml/datasets/Pima+Indians+Diabetes>.
- Wild, S., Roglic, G., Green, A., Sicree, R., King, H. 2004. Global prevalence of diabetes estimates for the year 2000 and projections for 2030. *Diabetes Care*, 27(5), pp. 1047-1053.

Solidworks Simulation of Mechanical Properties of Recycled Plastics/Nanocomposite Faces Sandwich Panels

Ahmad T. Azeez and Serwan S. Mohammed

Department of Manufacturing Engineering, Faculty of Engineering, Koya University,
Daniel Mitterrand Boulevard, Koya KOY45, Kurdistan Region - F.R. Iraq

Abstract– Sandwich panels are lightweight, high strength materials desired by engineers for various applications. However, many contributions cited the replacement of the metallic surfaces with reinforced polymeric composites for additional weight reduction purpose but none observed for recycled plastics. Accordingly, this work plans to investigate the mechanical behavior of sandwich panels made of recycled plastic/Nano reinforced composites under tension, compression, and bending load using Solidworks simulation. The data were obtained from previous works, and the complementary data were collected using different approaches. All models revealed that polycarbonate (PC) skin dominated over polypropylene and high-density polyethylene due to the highest modulus of elasticity. However, the results indicated that the core unless reinforced the outer skins will be separated as a result of residual strain at interfaces. Consequently, the core of PC skin sandwich panel reinforced with two thin sheets which lead to improvement in loading endurance from 500 to 1500N without exceeding the allowable limits of the materials and leading to the birth of environmentally intimated material termed green sandwich panel.

Index Terms–Recycled plastic skins, reinforced core, sandwich panels, solidworks.

I. INTRODUCTION

Sandwich panels are constructions of composite materials that provide engineers with desired properties as high mechanical performance accompanied by low weight. Sandwich panels consist of layers in which the outer thin metallic, polymeric, or fiber reinforced polymeric (GFRP) composites shields provide the desired mechanical properties as tensile strength, stiffness, and compression strength (Ramakrishnan, et al., 2015). The inner core of the panels consists of lightweight but mechanically weak materials

such as rigid polyurethane foam which is usually used to enhance the bulk properties of the panels. However, the cons of the core can be excluded off by combining it in between two skins of higher mechanical features (De Almeida, 2009). On the other hand, replacement of metallic skins with other materials that offer lightweight and high strength properties with low cost is a novel goal for researchers. For instance (Azmi, et al., 2017), used glassed fiber composites to shield the polyurethane foam core sandwich. The core itself reinforced additionally with coconut coir fibers to optimize the mechanical and physical properties of the sandwich panels. Bending test showed that modulus of the flexural ratio of sandwich composites to the naked core was 3084%. Furthermore, the probability of replacing reinforced concrete in the bridge deck with glass reinforced polymers foam core composites has been studied by Tuwair, et al., 2015. Three types of composites were investigated. Type1 high-density polyurethane (HDPE) foam and Type 2 low- density polyurethane foam reinforced with two-dimensional GFRP network, whereas Type 3 was trapezoidal-shaped polyurethane foam armored with extra GFRP web. The mechanical tests showed that Type 3 outperformed both Type 1 and Type 2 due to the weakness and the softness of the first two inner core types.

In addition (Kumar and Soragaona, 2014), optimized the design parameter of multilayer sandwich panels by optimizing the ratio of the outer sheets thickness to the overall thickness of the sandwich panels. The specimens were fabricated in a different manner that they consisted of multilayer sandwich panels', that is, face- core- face- core- face in which two thicknesses of the faces (1 mm and 2 mm) were examined and compared to face-core-face composites. The practical works showed that multilayer composites stiffness was superior to the normal design.

Utilizing the recycled plastics in sandwich panels unlike the virgin polymeric composites is still a fertile land for investigations. Moreover, knowing the disastrous effects of the plastic wastes on the environment will motivate us toward exploiting them as second-hand materials instead of tossing them in landfills. It is well known that the accumulation of polymeric wastes damages the ecological system. Take burning pit as an example, In Iraq, US military had burned

ARO-The Scientific Journal of Koya University
Volume VI, No. 1(2018), Article ID: ARO.10394, 6 pages
DOI: 10.14500/aro.10394

Received 08 April 2018; Accepted 04 June 2018

Regular research paper: Published 21 June 2018

Corresponding author's e-mail: ahmad.taifor@koyauniversity.org

Copyright © 2018 Ahmad T. Azeez and Serwan S. Mohammed. This

is an open access article distributed under the Creative Commons

Attribution License.



147 tons of waste per day in 2008 and abundant pollutants emitted into the air as combustion results causing long-term hygienic impacts. The most dangerous pollutant was highly toxic dioxins related to burning of plastic waste as rejected water bottles (Azeez, 2017). Accordingly, this research work for the 1st time reports on modeling sandwich panels from rubbish plastic/nanoparticles composites outer skins. The power of finite elements will be utilized to characterize the digital samples of sandwich panels using Solidworks software. The samples will be investigated under different work conditions based on technical data cited from previous literature.

II. METHODOLOGY

A. Technical Data of the Materials

The studied sandwich panel in this study consists of recycled plastic/nanofiller composite outer skins and polyurethane foam in between. The technical data from previous works have been taken into consideration in order to implement Solidworks. Hence, the materials that are candidate to replace the metallic surfaces of ordinary sandwich panels due to their superiority as observed in the literatures are recycled polypropylene (PP)/3% carbon nanotubes (CNT) composite (Liu and Gao, 2011) symbolized as PPC, recycled HDPE/4% nano graphene composite (Reddy, 2006) termed (HDPEC), and recycled polycarbonate (PC)/3% CNT composite (Zhang, et al., 2017) abbreviated as PCC. Accordingly, yield strength, ultimate strength, and modulus of elasticity were directly extracted from aforementioned works. Unfortunately, not all data were found in the articles, so they had to be collected through different scenarios. For instance, tensile test overwhelmed the mechanical characterization of the materials, and no record was found for compressive strength. To estimate the compression property required for Solidworks, the same trend will be followed as in the tensile test. For example, the tensile strength of virgin PP is 34.1 MPa and after one run of recycling the strength degraded by 2% to 33.39 MPa (Mahendrasinh, et al., 2013). By the addition of only 3% of CNT, the strength of the recycled PP increased by 71.75% (Liu and Gao, 2011). Now, assuming that the PP behavior is similar in compression and tension, one can approximately estimate the compressive strength of PPC by following the same fluctuating in its property. Therefore, if the compressive strength of pristine PP is 55 MPa (eFunda Polymers, n.d.) then after one batch of recycling it will reduce about 2% to 53.9 MPa which will, in turn, shift up about 71.75% to 94.46 MPa by considering the improvement effect of 3% CNT addition. Following the same procedure, the compressive strength of HDPEC and PCC estimated to be 33.44 and 56.1 MPa, respectively. However, the effect of recycling and improvement and the virgin values of compression strength of HDPEC and PCC with their sources can be found in the Appendix I. On the other hand, no contribution found regarding the effect of recycling and improvement on the Poisson's ratio and the effect on density could be worthless. Consequently, the simple rule of the mixture was used to

find the Poisson's ratios and the densities (Appendix II). Finally, the technical data used to run Solidworks are listed in Table I.

III. MODELING AND SIMULATION

A. Flatwise Compression Test

The specimen of the sandwich panel for the compressive wise test is modeled according to ASTM C 365/C 365M-05 with dimensions $20 \times 25 \times 25$ mm. The faces thicknesses were taken as 2 mm each. Load of 500N applied on the top surface while the bottom constrained. The key scope of this test is to characterize the load capacity of the structure under compression condition (ASTM, 2005).

B. Flatwise Tensile Test

The main goal of flatwise tensile is to determine the bonding integrity between the core and the faces. The samples were designed following ASTM C297/C297M-04 standards with same dimensions and load condition of flatwise compression test (ASTM, 2004).

C. Bending Test

Sandwich panels are widely used as roofing in construction materials; hence, they are vulnerable to bending due to their load condition. As a result, the flexural test is conducted in our study to optimize the performance of the structure based on the outer skin mechanical endurance. Samples with dimensions of $560 \times 25 \times 20$ mm were designed according to ASTM 7249/7249M-12 and subjected to the distributed load of resultant 500N, and the gravity was also considered. The thicknesses of the outer surfaces were 2 mm each as in the previous tests (ASTM, 2012).

IV. RESULTS AND DISCUSSION

A. Flatwise Compressive Simulation

The results of finite element analysis of flatwise compression properties of sandwich panels are shown in Fig. 1. PCC faces sandwich panels overwhelmed the others mechanically due to highest stress endurance (4274KPa) compared to 2824 and 2946 KPa for PPC and HDPEC skins, respectively. However, the highest stress value in PCC was accompanied with least deformation of about 0.85 mm compared to more than 0.9 mm for the other faces indicating the rigidity of PC skin.

TABLE I
TECHNICAL DATA OF MATERIALS

Properties of Materials	PPC	HDPEC	PCC	Polyurethane foam
Elastic modulus (MPa)	243	507.913	6000	13.61 ^a
Poisson's ratio	0.417	0.45	0.418	0.33 ^b
Shear modulus (MPa)	85.7	175	2115.65	5.11
Mass density Kg/m ³	917	973	1386.8	32 ^a
Tensile strength (MPa)	39.69	12.4	54	0.485 ^a
Compression strength (MPa)	94.46	33.865	65	0.287 ^a
Yield strength (MPa)	39.69	11	54	0.265 ^a

^aSparks and Arvidso, 1984, ^bDai, et al., 2015

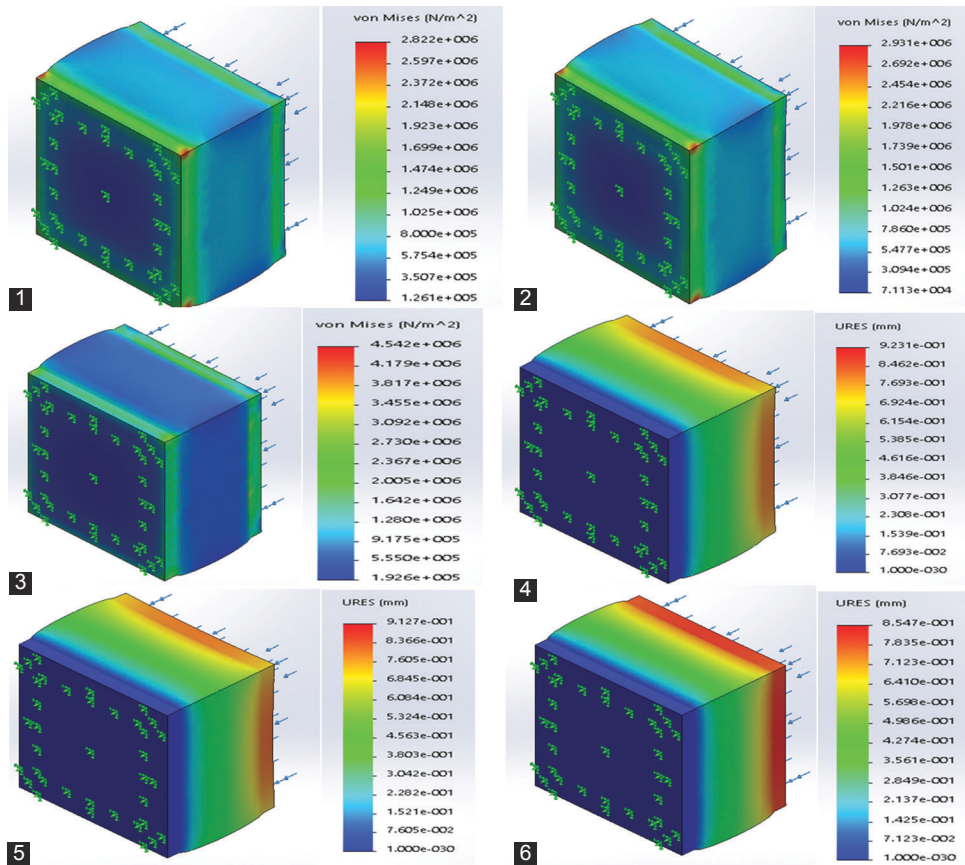


Fig. 1. (1-3) Von Mises stress, (4-6) displacement results for PPC, HDPEEC, and PCC.

Since the Solidworks models simulated elastically, the previous behaviors can be explained according to the modulus of elasticity, which is at highest value in recycled PC as listed in Table I.

On the other hand, despite that lower displacement leads to lower strain, an inverse trend observed in PCC at shield/core interfaces where the strain was highest as shown in Table II. This problem will be discussed briefly in the next section.

B. Flatwise Tensile Simulation

Results of the flatwise tensile test were comparative to compression test listed in Table II with negligible difference in the values. The spectrums of the strain throughout the thickness indicate the main concern to be considered otherwise splitting of the faces from core occurs that are the residual strain at the interfaces colored in red as shown in Fig. 2 The main cause of such strain concentration is the divergence of the materials properties at a specific point instead of gradual variation (Attiah and Azeez, 2014).

To support this physical point of view, we may calculate the ratios of Hock modulus differences between the surface and core. The modulus fraction of the PCC to polyurethane foam determined to be 99.77% compared to 97.3% and 94.3% for HDPEEC and PPC, respectively.

Accordingly, the strain concentration in PCC sandwich panels exceeded the others as stated in Table II due to sharp differences in the modulus of elasticity. On the other hand,

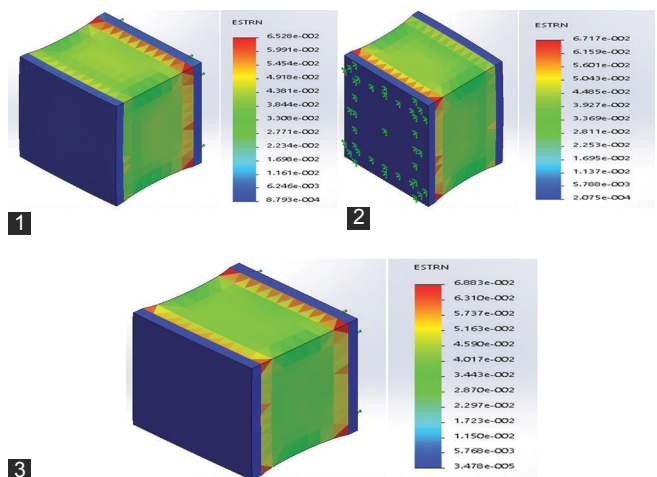


Fig. 2. Residual strain at interfaces in (1) PPC, (2) HDPEEC, and (3) PCC.

TABLE II
THE RESULTS OF FLATWISE COMPRESSION TEST

Sandwich panels	Von Mises stress (KPa)	Strain (mm/mm)	Deformation (mm)
PPC	2822	6.534E-2	0.9231
HDPEEC	2931	6.714E-2	0.9127
PCC	4542	6.888E-2	0.8547

the yield strain of polyurethane foam as reported by Sparks and Arvidso, 1984, is about 3% whereas the strain in all

models exceeded the double which will lead to peeling the skin from the core unless the foam reinforced.

The best model which is PCC skin was redesigned and the foam armored with a 1.5 mm strips with the same

TABLE III
FLEXURE TEST RESULTS

Sandwich panel	Von Mises stress (MPa)	Strain (mm/mm)	Deflection (mm)
PPC	6.631	2.267E-2	21.7
HDPEC	7.869	1.844E-2	16.15
PCC	13.43	1.368E-2	4.248

material of the skin. This modification not only protected the core but also leads to triple improvement in the bearing capacity from 500N to 1500N without exceeding the maxima of the materials Fig. 3. The maximum stress was 39.42 Mpa with only 0.2739mm deformation and 3% strain at the interface.

C. Bending Simulation

The resistance of the construction materials to deflection is a top concern for civil engineers since the majority of the loading condition in buildings, and specifically, the roofing is bending.

However, Solidworks modeling in flexure also emphasized the superiority of recycled PCC over the other. The distribution of Von Mises stress, strain, and the deflection within the structure is listed in Table III.

Again PCC endured the highest stress with a minimum deflection in midpoint as this is clear in Fig. 4. In addition to that, fortunately, all results were within the allowable limits provided by Table I.

V. CONCLUSIONS

All models revealed that PCC dominates over PPC and HDPEC due to high stiffness. However, the core should be reinforced to prevent separation at interfaces because of strain concentration. This is proposed to support the foam with two thin sheets of PCC. The subsequent modification in the design leads to spectacular results. The loading capacity multiplied 3 times, and the resulted values never exceeded

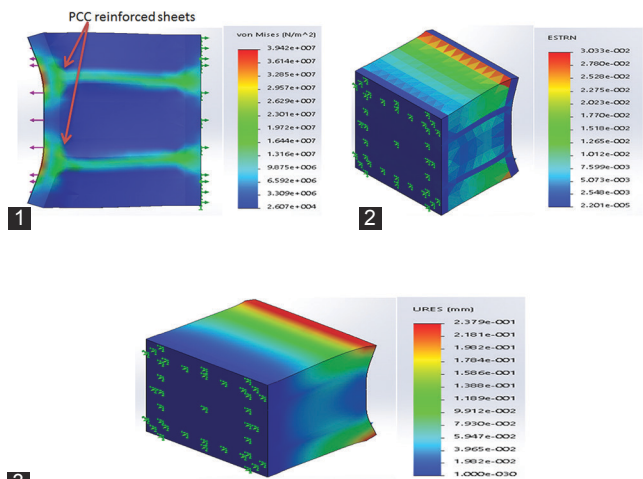


Fig. 3. (1) Von Mises stress, (2) strain, and (3) displacement in reinforced core in PCC sandwich panel.

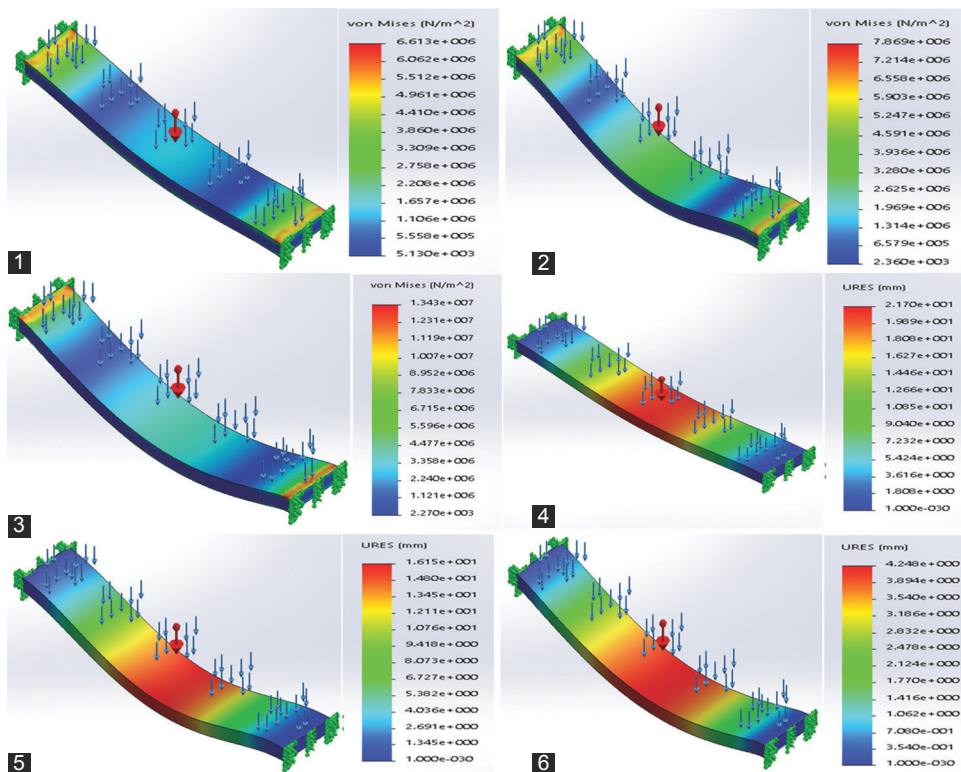


Fig. 4. (1-3) Von Mises stress, (4-6) deflections for PPC, HDPEC, and PCC respectively.

VI. APPENDICES

APPENDIX A

THE EFFECT OF RECYCLING AND NANO IMPROVEMENT ON THE MECHANICAL PROPERTIES OF THE MATERIALS

Materials	Virgin Properties	Effect of recycling	Effect of filler on recycled properties	Sources
HDPE behavior in tensile		16.6% degradation ^a	63.3% increase ^b	(Jiun, et al., 2016) (Reddy, 2006)
HPEC compression strength (MPa)	24.82 ^e	20.7	33.865	(Corneliussen, 2002)
PC behavior in tensile		2% increase ^d	Not significant ^e	(Ronkay, 2013) (Zhang, et al., 2017)
PCC compression strength (MPa)	55 ^f	56.1	56.1	(Kingston, et al., 2014)

APPENDIX B

DENSITIES AND POISSONS' RATIO OF THE MATERIALS

Types of materials	Density Kg/m ³	Poisson's ratio	Sources
PP	908	0.42	Typical engineering properties of PP, (2014)
HDPE	965	0.45	Typical engineering properties of HDPE, (2014)
Poly carbonate	1380	0.42	AZO materials
Nanotube and grapheme	1400 ^a	0.3 ^b	(Kumar, et al., 2018) (Zhao and Shi, 2011)

the allowable limits of the materials. On the other hand, shielding the panels with recycled polymeric strengthened composites leads to a new concept which may be termed as green sandwich panels.

REFERENCES

- ASTM. 2004. *C297/C 297M: Standard Test Method for Flatwise Tensile Strength of Sandwich Constructions*. ASTM International, West Conshohocken, PA, United States.
- ASTM. 2005. *C365/C 365M: Standard Test Method for Flatwise Compressive Properties of Sandwich Cores*. ASTM International, West Conshohocken, PA, United States.
- ASTM. 2012. *D7249/D7249M: Standard Test Method for Facing Properties of Sandwich Constructions by Long Beam Flexure*. ASTM International, West Conshohocken, PA, United States.
- Attiyah, A.A., Azeez, A.T., 2014. Design and modelling of (Fe/ZrO₂) functionally graded materials (Part I). *Engineering and Technology journals*, 32 Part (A), 7, pp. 1843-1858.
- Azeez, A.T., 2016. "A review of wood plastic composites effect on the environment. *Journal of Babylon University/Engineering Sciences*, 2(25), pp. 360-367.
- Azmi, M.A., Abdullah, H.Z. and Idris, M.I., 2013. Properties of polyurethane foam/coconut coir fiber as a core material and as a sandwich composites component. *IOP Conference Series: Materials Science and Engineering*, 50(012067), pp. 1-6. Available from: <http://www.iopscience.iop.org/article/10.1088/1757-899X/50/1/012067/meta>. [Last accessed on 2017 Nov 26].
- AZO materials Polycarbonate (PC). Available from: <https://www.azom.com/properties.aspx?ArticleID=2008>. [Last accessed on 2018 Feb 28].
- Beer, F.P., Johnston, E.R., DeWolf, J.T., 2006. *Mechanics of Materials*. 4th ed. McGraw Hill, USA.
- Corneliussen, D.R., 2002. HDPE Properties. Available from: <http://www.maropolymeronline.com/Properties/HDPE%20Prop.asp>. [Last accessed on 2018 Feb 22].
- Dai, B., Zhou, G., Sun, J., Chen, M. and Wang, J., 2015. Experimental study on the mechanical properties of looped fabric reinforced foam core sandwich composite. *Journal of Composite Materials*, 0(0), pp. 1-15.
- De Almeida, M.I.A., 2009. Structural behavior of composite sandwich panels for applications in the Construction Industry. *MS. Thesis, Instituto Superior Tecnico, Universidade Tecnica de Lisboa*.
- eFunda Polymers: Properties of polypropylene {homopolymer, unfilled}. Available from: http://www.efunda.com/materials/polymers/properties/polymer_datashet.cfm?MajorID=pp&MinorID=1. [Last accessed in 2018 Feb 21].
- Jiun, Y.L., Tze, C.T., Moosa, U. and A Tawawneh, M., 2016. Effects of recycling cycle on used thermoplastic polymer and thermoplastic elastomer polymer. *Polymers and Polymer Composites*, 24(9), pp. 735-740.
- Kingston, C., Zepp, R., Andrady, A., Boverhof, D., Fehir, R., Hawkins, D., Roberts, J., Sayre, P., Shelton, B., Sultan, Y., Vejins J.V. and Wohlleben, W. 2014. Review release characteristics of selected carbon nanotube polymer composites. *Carbon*, 68, pp. 33-57.
- Kumar, L., Jenni, L.V., Haluska, M., Roman, C. and Hierold, C., 2018. Mechanical stress relaxation in adhesively clamped carbon nanotube resonators. *AIP Advances*, 8(25118), pp. 025118.
- Kumar, V.M., Soragaona, B., 2014. Fabrication and evaluation of multilayered polyurethane foam core sandwich panels for static flexural stiffness. *Procedia Engineering*, 12th Global Congress on Manufacturing and Management, GCM, 97, pp. 1227-1236.
- Liu, Y., Gao, J., 2011. Mechanical properties and wear behavior of polypropylene/carbon nanotube nanocomposites. *Advanced Materials Research*, 299-300, pp. 798-801.
- Mahendrasinh, M.R., Hemul, V.P., Lata, M.R. & Naynika, K.P., 2013. Studies on mechanical properties of recycled polypropylene blended with virgin polypropylene. *International Journal of Science Invention Today*, 2(3), pp. 194-203.
- Ramakrishnan, K.R., Guerard, S., Maheo, L., Shankar, K. and Viot, P., 2015. Development of a finite element model for the simulation of parabolic impact of sandwich panels. *EDP Sciences*, 94(01018), pp. 01018(1-5).
- Reddy, R.J., 2006. Preparation, characterization and properties of injection molded graphene nanocomposites. *MS. Thesis, B.Tech, Jawaharlal Technological University, Andhra Pradesh, India*.
- Ronkay, F., 2013. Effect of recycling on the rheological, mechanical and optical properties of polycarbonate. *Acta Polytechnica Hungarica*, 10(1), pp. 209-220.
- Sparks, L.L. and Arvidso, J.M., 1984. *Thermal and Mechanical Properties of Polyurethane Foams and a Survey of Insulating Concretes at Cryogenic Temperature*. Colorado: National Bureau of Standards U.S. Department of Commerce Boulder, Colorado 80303: NBS Publication.

Tuwair, H., Hopkins, M., Volz, J., ElGawady, M.A., Mohamed, M., Chandrashekhara, K. and Birman, V., 2015. Evaluation of sandwich panels with various polyurethane foam-cores and ribs. *Composites Part B*, 79, pp. 262-276.

Typical Engineering Properties of Polypropylene. 2014. Available from: <https://www.ineos.com/globalassets/ineos-group/businesses/ineos-olefins-and-polymers-usa/products/technical-information--patents/ineos-engineering-properties-of-pp.pdf>. [Last access on 2017 Dec 21].

Zhang, J., Bello, D., Isaacs, J.A., Jozokos, T., Mead, J., 2017. The effect of recycling on the structure and properties of carbon nanotube-filled polycarbonate. *Material for Energy, Efficiency and Sustainability: Tech Connect Briefs*, 2, 308-311.

Zhao, P. and Shi, G., 2011. Study of Poisson's ratios of graphene and single-walled carbon nanotubes based on an improved molecular structural mechanics model. *Tech Science Press SL*, 5(1), pp. 49-58.

Determination of Natural Radioactivity and Radiological Hazards of ^{226}Ra , ^{232}Th , and ^{40}K in the Grains Available at Penang Markets, Malaysia, Using High-purity Germanium Detector

Najeba F. Salih

Department of Physics, Faculty of Science and Health, Koya University, Koya KOY45, Kurdistan Region, F.R. Iraq

Abstract— In the present study, the concentrations of ^{226}Ra , ^{232}Th , and ^{40}K and their radiological hazards in 18 types of grain samples, collected from local markets in Penang, Malaysia, are investigated using high-purity germanium detector (HPGe). The results indicated that the concentration of ^{226}Ra , ^{232}Th , and ^{40}K in grain samples was ranged from 56.97 to 86.13 Bq.kg⁻¹, from 34.71 to 52.14 Bq.kg⁻¹, and from 517.05 to 997.59 Bq.kg⁻¹, respectively. The results of the average annual ingestion dose of natural radionuclides of ^{226}Ra , ^{232}Th , and ^{40}K were found to be 66.555, 35.199, and 15.328 μSv y⁻¹, respectively. This results are below the standard worldwide value (290 μSv y⁻¹) that was reported by UNSCEAR. Therefore, the studied samples are considered safe in terms of the radiological health hazards, and there is no health hazard from the grain in this region.

Index Terms— ^{226}Ra , ^{40}K , Grain gamma rays, Natural Radioactivity, radiological hazards.

I. INTRODUCTION

Natural radionuclides are present in every human environment; earth material, water, air, foods, and even our own body contain naturally occurring radioactive. The main natural radioactive sources of ionizing radiation are the long-lived ^{238}U , ^{232}Th , and their decay series and the ^{40}K (Tawalbeh et al., 2011). Radioactive elements such as uranium and thorium are also present in the atmosphere of cement plants (Adil et al., 2018). Analysis of these radionuclides in foodstuff is an important part of the environmental monitoring program. These natural radioactive sources are the largest contributor of the radiation doses received by humanity (Abdulaziz et al., 2013). Naturally occurring potassium ^{40}K is present

virtually in all foodstuff as primary constituent of cellular material (Abdulaziz et al., 2013; Rohit et al., 2014; Awudu et al., 2012; Cumhur and Mahmut, 2013). Radionuclides can enter the human body through inhalation and ingestion. The ingested radionuclides could be concentrated in certain parts of the body (Tawalbeh et al., 2011); therefore, ingestion of radionuclides through food intake may account for a substantial fraction of the average radiation doses to various organs of the body, and this may also represent one of the important pathways for long-term health considerations (Jibiri et al., 2007; Al-Masri et al., 2004). For example, it has been estimated that at least one-eighth of the mean annual effective dose due to natural sources can be attributed to the intake of food (Jibiri et al., 2007; Gabdo et al., 2015).

Food is known to contain natural and artificial radionuclides that, after ingestion, contribute to an effective internal dose. It has been estimated that a large portion, at least one-eighth, of the mean annual dose due to natural sources is caused by the intake of food. Average radiation doses to various organs of the body also represent an important pathway for long-term health considerations. ^{232}Th , ^{238}U (^{226}Ra), and ^{40}K are three long-lived naturally occurring radionuclides present in the earth crust. They generally enter the human body through the food chain (Rafat and Fawzia, 2013). Measurements of natural radioactivity in environmental elements have been carried out in different countries to establish baseline data from the natural radiation levels (Ahmad et al., 2015). The data on the radioactivity of radium, thorium, and potassium in food are directly related with the safety of population; therefore, this study aimed to provide the basic radiometric data of radioactive in the grain food. The primary purpose of this study is to determine the activity concentration levels of ^{226}Ra , ^{232}Th , and ^{40}K in the different types of grain that are available in Penang markets, Malaysia, to ensure that food safety is not compromised and the effective doses due to ingestions are within the specified safety limits. Several studies have been performed in different countries to determine the radionuclide concentration in different food samples and dose assessment

ARO-The Scientific Journal of Koya University
Volume VI, No.1 (2018), Article ID: ARO.10327, 7 pages
DOI: 10.14500/aro.10327

Received: 08 November 2017; Accepted: 18 June 2018

Regular research paper: Published 30 June 2018

Corresponding author's, email: najeba.farhad@koyauniversity.org

Copyright © 2018 Najeba F. Salih. This is an open-access article distributed under the Creative Commons Attribution License.



from consumption of that foodstuff by the population (Awudu et al., 2012). As grain and its products are the main component of daily serving such as breads, rice, and pasta, it is considered as a staple food. The levels of radioactive materials in some grains consumed by population need to be carefully measured so as to forecast any possible associated radiological risk.

II. METHODOLOGY

A. Sample Collection and Preparation

In the present study, to determine grain radionuclides' concentration, an experiment was carried out on 18 types of grain samples collected from local markets of Penang city, Malaysia. Afterward, the samples were immediately brought to laboratory within 1 day to prepare the grain samples and to keep them accordingly. Each sample was crashed into fine powder form by blender and passed through sieve with mesh to produce particle sizes of <0.249 mm and hence to obtain uniform sample powder (homogenous), which is in line with the study of Shafaei et al., 2011. 300 g of each grain sample was weighted using electrical balance; then, the samples put in small plastic tube and sealed to prevent the leakage of radon gas and then stored separately for 1 month to allow radioactive equilibrium stage between ^{226}Ra and ^{232}Th and its short-lived decay products before performing radioactivity measurements (Murat et al., 2010; Usikalu et al., 2014). Then, the radionuclides of ^{226}Ra , ^{232}Th , and ^{40}K in grain samples were measured using high-purity germanium spectroscopy (HPGe detector) (Bashir et al., 2012).

B. Statistical Analysis

Statistical descriptions were performed using SPSS (Statistical Package for the Social Sciences) for Windows, standard version 22.0. Analysis of the data was carried out by frequency distributions (Pearson correlation) to assess the statistical significance in the three radionuclides measured in the grain samples.

C. Gamma Spectrometry Analysis

In the present work, the measurements of natural radioactivity levels were performed by gamma-ray spectrometry, using a HPGe detector connected to a multichannel analyzer. A high power supply that generates a high voltage (0–1500 V) to the detector through an amplifier at 1332 keV of ^{60}Co source, having ability to differentiate the gamma-ray energies, was utilized which is in agreement with the study of Gordana et al., 2015. The gamma spectrometry was shielding by a thick shield (5 cm) of lead encasing the HPGe detector (the inner diameter is 10 cm, and height is 50 cm). The background radiation was determined using an empty container with dimensions similar to that of the samples. The analysis was fixed at the duration of 86,400 s to produce a gamma spectrum that is agree with previous studies (Mohammed et al., 2015; Augustine et al., 2015). The samples were then placed on the top of the detector and were counted for 86,400 s in an attempt to

attain minimum counting error in accordance with the study of Matthew et al., 2015.

D. Efficiency and Energy Calibrations

In this study, before the analysis of the samples, the calibrations of gamma energy and efficiency calibration for the system were performed using standard sources from the International Energy Agency IAEA, such as ^{60}Co , ^{137}Cs , ^{22}Na , ^{241}Am , and ^{226}Ra , that is in agreement with the study of Hossain et al., 2012. Certified standards of known activities were used to derive the calibration curve for energy and the efficiency of the HPGe detector since the efficiency is an important parameter of HPGe detector (Khandaker, 2011). The efficiency calibration curve of HPGe detector is shown in Fig. 1. Furthermore, the absolute efficiency of the HPGe detector for gamma-ray energies was calculated using the following equation (Njinga et al., 2015):

$$\varepsilon = \frac{\text{CPS}}{A_t \times I_\gamma} \times 100\% \quad (1)$$

Where CPS is counts per second, A_t presents activity of the source, and I_γ is gamma-ray intensity per decay.

The analyses of radionuclides of the grain samples were carried out based on the energy peaks of the progenies. The concentrations of the decay products of ^{214}Pb (295.224 keV, 18.7% and 351.932 keV, 35.8%) and ^{214}Bi (609.312 keV, 45%; 1120.287 keV, 14.8%; and 1764.494 keV, 15.65%) were taken to indicate ^{226}Ra , whereas the specific activity of ^{232}Th has been calculated based on the energy peaks of ^{212}Pb (238.632 keV, 47.3%), ^{228}Ac (911.204, 29% and 968.971 keV, 17.5%), and ^{208}Tl (583.191, 84.5%), but the activity concentration of ^{40}K was assessed directly from its gamma-ray peak of 1460.83 KeV, 10.67% (IAEA, 1989) which is in compliance with studies made by Darwish et al., 2015; Raymond et al., 2016; and Mohammad et al., 2015. After correcting the background, the concentrations of the radionuclides of ^{226}Ra , ^{232}Th , and ^{40}K of the grain samples were calculated by subtracting the area of prominent gamma-ray energy from the background radiation using the following equation (Nisar, 2015; Banzi et al., 2017):

$$\text{Concentration (Bq.kg}^{-1}\text{)} = (C - C_{\text{background}}) / t p_\gamma \varepsilon w \quad (2)$$

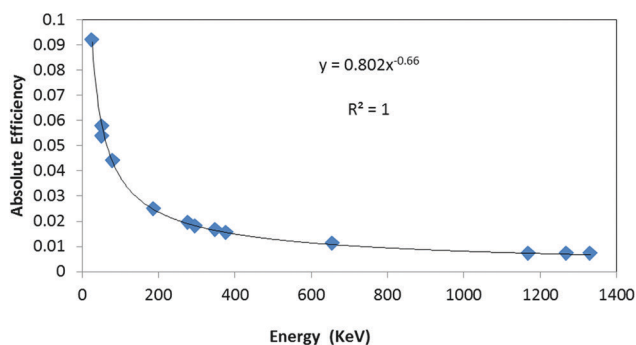


Fig. 1. Efficiency calibration curve for the high-purity germanium detector.

Where C is net area under peak, $C_{background}$ is net area of background radiation, t is time of counting (sec), P_{γ} is the absolute transition probability, ϵ is detector efficiency for the corresponding peak, and w is weight of the grain sample in kg (Njinga et al., 2015).

III. CALCULATION OF CONCENTRATION OF RADIONUCLIDE and HAZARD INDICES

A. Concentration of Radionuclides

The concentration of radionuclides of ^{226}Ra , ^{232}Th and ^{40}K in a unit of Bq.kg^{-1} has been calculated using the relation in the study of Murtadha et al., 2017, and Nisar, 2015.

B. Hazard Indices

Assessment of radiological hazard

The relationship between radiation risk and natural radionuclides of ^{226}Ra , ^{232}Th , and ^{40}K can be determined by different radiation hazard indices. In the presented study, three hazard indices were considered, which are as follows (Okeme et al., 2017):

Radium equivalent activity: The radium equivalent activity (Raeq), which is a single index, used to describe the gamma output from different mixtures of radium, thorium, and potassium in the material. It was calculated from the following equation (Nisar, 2015; Al-Hamed et al., 2017):

$$\text{Raeq} = C_{\text{Ra}} + 1.43C_{\text{Th}} + 0.077C_{\text{K}} \quad (3)$$

Where C_{Ra} , C_{Th} , and C_{K} are activity concentrations of ^{226}Ra , ^{232}Th , and ^{40}K , respectively.

Alpha index: The excess alpha radiation due to the radon inhalation originating from the grain samples is assessed through alpha index, and it was <1 . Alpha index ($I\alpha$) was calculated according to the following equation (Gordana et al., 2015).

$$I\alpha = C_{\text{Ra}}/200 \quad (4)$$

Annual ingestion dose: The annual ingestion dose (E_{ING}) for human was coming from consumption of grain, owing to the ingestion of radionuclides. The average consumption of grain product is $(3.3) \text{ kg y}^{-1}$ that was reported by the United Nations Scientific Committee on Effects Atomic Radiations in 2000 (UNSCEAR, 2000). Therefore, 3.3 kg per year has been considered for the estimation of radiation dose to the adult population in Penang (Kritsanuwat et al., 2014). The E_{ING} was calculated using the following equation (Murtadha et al., 2017; Rafat and Fawzia, 2013; Adjirackor et al., 2014):

$$E_{\text{ING}} = A_1 \times C \times \text{FDC}_{\text{ING}} \quad (5)$$

Where E_{ING} is the annual ingestion dose ($\mu\text{Sv y}^{-1}$), A_1 is the activity concentration (Bq.kg^{-1}) of the investigated radionuclides in the vegetables, C is the consumption rate ($3.3) \text{ kg y}^{-1}$ (Kritsanuwat et al., 2014; Ononugbo et al., 2017) depending on the type of samples, and FDC_{ING} is the ingestion dose coefficient of the ^{226}Ra , ^{232}Th , and ^{40}K which was 0.2, 0.23 ($\mu\text{Sv Bq}^{-1}$), and 6.2 (nSv Bq^{-1}), respectively (Murtadha et al., 2017).

IV. RESULTS AND DISCUSSION

The concentrations of ^{226}Ra , ^{232}Th , and ^{40}K were successfully measured through gamma-ray spectrometry in different types of grain. Eighteen samples of grain (different types) were analyzed using high resolution gamma-ray spectrometry with high pure germanium detector. The concentration distribution of ^{226}Ra , ^{232}Th , and ^{40}K in the samples found in Bq.kg^{-1} was divided among various sources which include cereals: Wheat, Oats, rice, maize, kamut, buckwheat, barley, rye, and millet and legumes: Clover, alfalfa, beans, mesquite, lentils, peas, soybeans, lupins, and carob, as given in Table I. The radionuclides of ^{226}Ra , ^{232}Th , and ^{40}K in grains are not uniformly distributed, and hence, the radionuclide concentration (Raeq) in Bq.kg^{-1} is used to compare the specific activity of materials containing different amounts of ^{226}Ra , ^{232}Th , and ^{40}K . It was calculated using the formula given by Equation (2). The concentration of ^{226}Ra , ^{232}Th , and ^{40}K in grain samples ranged between minimum and maximum values as follows: 56.97 Bq.kg^{-1} and 86.13 Bq.kg^{-1} , 34.71 Bq.kg^{-1} and 52.14 Bq.kg^{-1} , and 517.05 Bq.kg^{-1} and 997.59 Bq.kg^{-1} , respectively. Table I also shows that the maximum values of concentration were found in ^{40}K among the three natural radionuclides studied in the grain samples. The mean concentration was observed to be highest for ^{40}K , followed by ^{232}Th , and the lowest mean concentration was for ^{226}Ra ($766.44 > 72.03 > 46.38$) because ^{40}K is an essential element for living organisms; therefore, the ^{40}K radioactivity cannot be avoided.

The concentration for natural radionuclides indicates that concentrations for all radionuclides are higher than

TABLE I
THE CONCENTRATION OF ^{226}Ra , ^{232}Th , AND ^{40}K IN GRAINS, CEREALS, AND LEGUMES SAMPLES

Code of samples	Types of grain samples	Specific activity of ^{226}Ra , ^{232}Th , and ^{40}K (Bq.kg^{-1})		
		^{226}Ra	^{232}Th	^{40}K
	Cereals			
GS01	Wheat	64.87	49.57	517.05
GS02	Oats	70.52	48.44	995.90
GS03	Rice	86.13	51.82	618.13
GS04	Maize	67.12	47.61	992.81
GS05	Kamut	66.87	52.14	809.32
GS06	Buckwheat	71.21	50.34	814.59
GS07	Barley	56.97	34.71	986.02
GS08	Rye	66.81	48.25	643.52
GS09	Millet	73.69	41.81	602.06
	Legumes			
GS10	Alfalfa	77.09	43.51	855.70
GS11	Clover	68.41	44.21	611.36
GS12	Beans	72.72	43.85	954.44
GS13	Peas	78.82	47.13	620.18
GS14	Lentils	69.32	42.47	572.36
GS15	Mesquite	74.22	45.35	997.59
GS16	Carob	81.06	50.09	636.79
GS17	Lupins Carob	78.58	49.97	963.16
GS18	Soybeans	72.12	43.51	605.02
Ave		72.03	46.38	766.44
Mix		86.13	52.14	997.59
Min		56.97	34.71	517.05

the world median values except for ^{226}Ra which is agreed with the previous study reported by Matthew et al., 2015. Lowest concentration of ^{226}Ra (56.97 Bq.kg^{-1}) and ^{232}Th (34.71 Bq.kg^{-1}) was found in Barley samples, but Barley sample has highest radionuclides of ^{40}K ($986.02 \text{ Bq.kg}^{-1}$). Therefore, the lowest concentration of ^{226}Ra was found in Barley (56.97 Bq.kg^{-1}) and highest concentration of ^{226}Ra was found in rice (86.13 Bq.kg^{-1}) with the average concentration of ^{226}Ra (72.03 Bq.kg^{-1}), and the lowest concentration of ^{232}Th was found in Barley (34.71 Bq.kg^{-1}) and highest concentration of ^{232}Th was found in kamut (52.14 Bq.kg^{-1}) with the average concentration of ^{232}Th (46.38 Bq.kg^{-1}); furthermore, the lowest concentration of ^{40}K was found in wheat ($517.05 \text{ Bq.kg}^{-1}$) and highest concentration of ^{40}K was found in mesquite ($997.59 \text{ Bq.kg}^{-1}$), with the average of concentration for ^{40}K ($766.44 \text{ Bq.kg}^{-1}$). The mean concentration of ^{232}Th (46.38 Bq.kg^{-1}) was slightly higher than the World's average (30 Bq.kg^{-1}) (UNSCEAR, 2000). The highest activity concentration of ^{232}Th was found in kamut (52.14 Bq.kg^{-1}). The highest activity concentration of ^{226}Ra was found in rice (86.13 Bq.kg^{-1}) and the highest activity concentration of ^{40}K was found in the both mesquite ($997.59 \text{ Bq.kg}^{-1}$) and oats ($995.90 \text{ Bq.kg}^{-1}$), whereas lowest concentration of ^{232}Th was found in barley (34.71 Bq.kg^{-1}), lowest concentration of ^{226}Ra was found in barley (56.97 Bq.kg^{-1}), and lowest concentration of ^{40}K was found in wheat ($517.05 \text{ Bq.kg}^{-1}$) among the samples when compared to other samples in this study, as shown in Table I and Fig. 2.

In Table II, the activity ratio of ^{232}Th - ^{226}Ra was ranged between 0.564 in alfalfa sample and 0.779 in kamut sample with an average value of 0.646, the activity ratio of ^{40}K - ^{226}Ra was ranged between 7.17 in rice sample and 17.31 in barley sample with an average value of 10.77, and the activity ratio of ^{40}K - ^{232}Th was ranged between 10.43 in wheat sample and 28.41 in barley sample with an average value of 16.74.

In addition, the external irradiation radon and its short-lived products are also hazardous to the respiratory organs. The alpha radiation producing from the grain is estimated through alpha index should be less than 1 and is calculated according to the equation (Awudu et al., 2012) and average value of I_α is 0.360 Bq.kg^{-1} that is <1 , as shown in Table III, which is in agreement with the study of Gordana et al., 2015,

because the recommended limit concentration of ^{226}Ra is 200 Bq.kg^{-1} for which $I_a=1$ (Gordana et al., 2015).

It is clear from the results of Table IV that the average annual ingestion dose of natural radionuclides of ^{226}Ra , ^{232}Th , and ^{40}K was 66.555 , 35.199 , and $15.328 \mu\text{Sv y}^{-1}$, respectively. These obtained values are significantly below the total worldwide annual effective ingestion dose of ^{226}Ra , ^{232}Th , and ^{40}K that was $290 \mu\text{Sv y}^{-1}$, reported by UNSCEAR, 2000, and Kritsanuwat et al., 2014; Asaduzzaman et al., 2014). Furthermore, the average annual ingestion dose of grain was found to be below the values recommended, $250\text{--}400 \mu\text{Sv y}^{-1}$, as reported by the WHO, 2011. The differences could be due to the variation in the consumption of the grain and the natural environment in these countries. However, the average total annual ingestion dose in the grain samples is low and, therefore, is not harmful to human health.

TABLE II
THE RATIO OF ^{232}Th , ^{226}Ra , AND ^{40}K IN THE GRAIN SAMPLES UNDER STUDY

Code of samples	Types of grain samples	The ratio of specific activity of ^{226}Ra , ^{232}Th , and ^{40}K		
		^{232}Th - ^{226}Ra	^{40}K - ^{226}Ra	^{40}K - ^{232}Th
	Cereals			
GS01	Wheat	0.764	7.97	10.43
GS02	Oats	0.687	14.12	20.56
GS03	Rice	0.601	7.17	11.92
GS04	Maize	0.709	14.79	20.85
GS05	Kamut	0.779	12.11	15.52
GS06	Buckwheat	0.707	11.44	16.18
GS07	Barley	0.609	17.30	28.41
GS08	Rye	0.722	9.63	13.33
GS09	Millet	0.567	8.17	14.41
	Legumes			
GS10	Alfalfa	0.564	11.09	19.66
GS11	Clover	0.646	8.93	13.83
GS12	Beans	0.603	13.12	21.76
GS13	Peas	0.597	7.86	13.16
GS14	Lentils	0.613	8.25	13.47
GS15	Mesquite	0.611	13.44	21.99
GS16	Carob	0.618	7.85	12.71
GS17	Lupins	0.636	12.25	19.27
GS18	Soybeans	0.603	8.38	13.91
Ave		0.646	10.77	16.74
Mix		0.779	17.31	28.41
Min		0.564	7.17	10.43

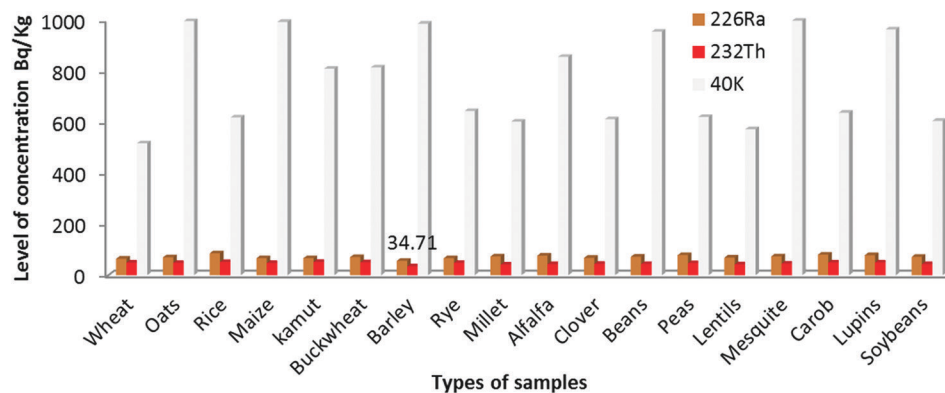


Fig. 2. The concentration of radionuclides in the samples as the function of the types of samples.

TABLE III
RADIATION HAZARD INDICES OF GAMMA RAY IN THE GRAIN SAMPLES

Code of samples	Raeq (Bq.kg ⁻¹)	Iα (Bq.kg ⁻¹)
GS01	175.568	0.324
GS02	216.485	0.352
GS03	207.840	0.431
GS04	211.646	0.335
GS05	203.752	0.334
GS06	205.929	0.356
GS07	182.525	0.285
GS08	185.367	0.334
GS09	179.832	0.368
GS10	205.211	0.385
GS11	178.697	0.342
GS12	208.928	0.363
GS13	193.970	0.394
GS14	174.132	0.346
GS15	215.893	0.371
GS16	201.738	0.405
GS17	224.209	0.393
GS18	180.939	0.360
Ave	197.370	0.360
Mix	224.209	0.430
Min	174.131	0.285

TABLE IV
THE ANNUAL INGESTION DOSE ESTIMATE IN THE GRAIN SAMPLES

Code of samples	Types of grain samples	Annual ingestion dose of ²²⁶ Ra, ²³² Th, and ⁴⁰ K (μSv y ⁻¹)		
		²²⁶ Ra	²³² Th	⁴⁰ K
Cereals				
GS01	Wheat	59.939	37.623	10.341
GS02	Oats	65.160	36.765	19.918
GS03	Rice	79.584	39.331	12.362
GS04	Maize	62.018	36.136	19.856
GS05	Kamut	61.787	39.574	16.186
GS06	Buckwheat	65.798	38.208	16.299
GS07	Barley	52.640	26.345	19.720
GS08	Rye	61.732	36.621	12.870
GS09	Millet	68.089	31.734	12.041
Legumes				
GS10	Alfalfa	71.231	33.024	17.114
GS11	Clover	63.210	33.555	12.227
GS12	Beans	67.193	33.282	19.088
GS13	Peas	72.829	35.771	12.403
GS14	Lentils	64.051	32.234	11.447
GS15	Mesquite	68.579	34.420	19.959
GS16	Carob	74.899	38.018	12.736
GS17	Lupins Carob	72.608	37.927	19.263
GS18	Soybeans	66.638	33.024	12.100
Ave		66.555	35.199	15.3289
Mix		79.584	39.574	19.959
Min		52.640	26.345	10.341

A. Correlation between Laboratory Data Analysis and the Radionuclides (²²⁶Ra, ²³²Th, and ⁴⁰K)

From Table V, it can be observed that positive correlation exists among the three radionuclides and annual ingestion dose. Pearson correlation showed significant strong positive correlations (1.000**, *p* value <0.001) for each annual ingestion dose of ²²⁶Ra with the concentration ²²⁶Ra, annual

TABLE V
PEARSON CORRELATION AMONG RADIONUCLIDES PARAMETERS AND LABORATORY DATA

Laboratory data				
Variables	Correlations	²²⁶ Ra	²³² Th	⁴⁰ K
²²² Ra concentration	Pearson correlation	1.000	0.459	-0.173
	<i>P</i> value	<0.001	0.055	0.479
²³² Th concentration	Pearson correlation	0.459	1.000	-0.131
	<i>P</i> value	0.055	<0.001	0.603
⁴⁰ K concentration	Pearson correlation	-0.173	-0.131	1.000
	<i>P</i> value	0.479	0.603	<0.001
Annual ingestion dose of ²²⁶ Ra	Pearson correlation	1.000**	0.459	-0.173
	<i>P</i> value	<0.001	<0.055	0.479
Annual ingestion dose of ²³² Th	Pearson correlation	0.459	1.000**	-0.131
	<i>P</i> value	0.055	<0.001	0.603
Annual ingestion dose of ⁴⁰ K	Pearson correlation	-0.173	-0.131	1.000**
	<i>P</i> value	0.479	0.603	<0.001

**Correlation is high significant at the 0.01 level (two-tailed), correlation is significant at the 0.05 level (two-tailed)

ingestion dose of ²³²Th with the concentration ²³²Th, and annual ingestion dose of ⁴⁰K with the concentration ⁴⁰K. This correlation among variables indicates similar source and behavior in the environment, but not significant correlations (*P* = 0.479) were found between ²²⁶Ra and ⁴⁰K and no significant correlations (*P* = 0.603) were found between ²³²Th and ⁴⁰K. Therefore, the correlation of ²²⁶Ra and ²³²Th was more stronger than the correlation of ⁴⁰K, as shown in Table V.

V. CONCLUSIONS

A study of natural radioactivity in the grain samples is usually done to gain information about the levels of harmful of radioactivity in environment and to understand the behavior of natural radionuclides. Therefore, the grain samples for eating are considered to be safe for inhabitants. It is suggested that the values reported in the current study can be considered as within the “normal level” of radiation and is below the worldwide averaged value. The baseline data of this type will almost certainly be of importance in making estimations of population exposure. The purpose of this study is to analyze the level of radioactivity of ⁴⁰K, ²²⁶Ra, and ²³²Th in the different types of grain that is available in Penang markets, Malaysia to determine the effective doses of ⁴⁰K, ²²⁶Ra, and ²³²Th in the samples due to ingestions which are within the specified safety limits. Hence, there is no radiological risk in the grain samples in the Penang market, and the results of this study indicated that radionuclide intake due to grain consumption has no consequence on public health. Hence, results concluded that all the three radionuclides contribute significantly to gamma-ray emission at the sampling points.

REFERENCES

Abdulaziz, A., and El-Taher, A., 2013. A study on transfer factors of radionuclides from soil to plant. *Life Science Journal*, 2(10), pp.532-539.

Adil, M.H., Abdullah, K.O., Kharman, A.F., and Dara, F.H., 2018. Radon concentration in the work atmosphere of cement plants in the sulaymaniyah area,

Iraq. *ARO-The Scientific Journal of Koya University*, 6(1), pp.7-12.

Adjirackor, T., Darko, E.O., Emi-Reynolds, G., Kpeglo, D.O., Awudu, R., and Owusu, J.B., 2014. Radiological study of soil, fertilizer and foodstuffs in some selected farming communities in the greater Accra region, Ghana. *Elixir Nuclear and Radiation Physics*, 77, pp. 29112-29118.

Ahmad, N., Jaafar, M., and Alsaffar, M., 2015. Natural radioactivity in virgin and agricultural soil and its environmental implications in Sungai Petani, Kedah, Malaysia. *Pollution Journal*, 1(3), pp.305-313.

Al-Hamed, S.A., Wahby, M.F., and Aboukarima, A.M. 2017. Evaluation of natural radionuclides, cesium-137 and radiological hazard indices of agricultural soils in Saudi Arabia. *Journal of Nuclear Technology in Applied Science*, 5(1), pp.27-42.

Al-Masri, M.S., Mukallati, H., Al-Hamwi, A., Khalili, H., Hassan, M., Assaf, H., Amin, Y., and Nashawati, A. 2004. Natural radionuclides in Syrian diet and their daily intake. *Journal of Radioanalytical and Nuclear Chemistry*, 260(2), pp.405-412.

Asaduzzaman, K.H., Mayeen, U.K., Amin, Y.M., Bradley, D.A., Mahat, R.H., and Nor, R.M., 2014. Soil-to-root vegetable transfer factors for ^{226}Ra , ^{232}Th , ^{40}K , and ^{88}Y in Malaysia. *Journal of Environmental Radioactivity*, 135, pp.120-127. Available from: <http://www.elsevier.com/locate/jenvrad>.

Augustine, K.A., Morounfolu, A.O., and Peter, O.A., 2015. Radiological safety assessment and determination of heavy metals in soil samples from some waste dumpsites in Lagos and Ogun state, south-western, Nigeria. *Journal of Radiation Research and Applied Sciences*, 8(1), pp.148-153.

Awudu, A.R., Faanu, A., Darko, E.O., Emi-Reynolds, G., Aduko, O.K., Kpeglo, D.O., Otoo, F., Lawluvi, H., Kpodzro, R., Ali, I.D., Obeng, M.K., and Agyeman, B., 2012. Preliminary studies on ^{226}Ra , ^{228}Ra , ^{228}Th and ^{40}K concentrations in foodstuffs consumed by inhabitants of Accra metropolitan area, Ghana. *Journal of Radioanalytical and Nuclear Chemistry*, 291(3), pp.635-641.

Banzi, F., Msaki, P., and Mohammed, N. 2017. Assessment of radioactivity of ^{226}Ra , ^{232}Th and ^{40}K in soil and plants for estimation of transfer factors and effective dose around Mkuju river project, Tanzania. *Mining of Mineral Deposits*, 11(3), pp.93-100.

Bashir, G.M., Mohammad, S.J., Azhar, A.R., and Farouk, A.I. 2012. Determination of radioactive elements and heavy metals in sediments and soil from domestic water sources in northern peninsular Malaysia. *Environmental Monitoring and Assessment*, 184(3), pp.5043-5049.

Cumhur, C., and Mahmut, D., 2013. A preliminary study on ^{226}Ra , ^{232}Th , ^{40}K and ^{137}Cs activity concentrations in vegetables and fruits frequently consumed by inhabitants of Elazig Region, Turkey. *Journal of Radioanalytical and Nuclear Chemistry*, 295(2), pp.1245-1249.

Darwish, D.A.E., Abul-Nasr, K.T.M., and El-Khayatt, A.M. 2015. The assessment of natural radioactivity and its associated radiological hazards and dose parameters in granite samples from South Sinai, Egypt. *Journal of Radiation Research and Applied Sciences*, 8(1), pp. 17-25.

Gabdo, H.T., Ramli, A.T., Saleh, M.A., Sanusi, M.S., Garba, N.N., and Aliyu, A.S., 2015. Radiological hazard associated with natural radionuclide concentrations in the northern part of Pahang state Malaysia. *Environmental Earth Sciences*, 73(10), pp.6271-6281.

Gordana, K.P., Dragana, J.T., Jelena, D.N., Milica, M.R., Marija, M.J., and Natasa, B.S., 2015. Measurement of radioactivity in building materials in Serbia. *Journal of Radioanalytical and Nuclear Chemistry*, 303(3), pp.2517-2522.

Hossain, I., Sharip, N., and Viswanathan, K.K., 2012. Efficiency and resolution of HPGe and NaI(Tl) detectors using gamma-ray spectroscopy. *Scientific Research and Essays, Academic Journals*, 7(1), pp.86-89.

IAEA. 1989. Measurement of Radionuclides in Food and the Environment. *A Guidebook. International Atomic Energy Agency, Vienna*, Vol. 295. STI/DOC/10/295 ISBN 92-0-125189-0, ISSN 0074-1914.

Jibiri, N.N., Farai, I.P., and Alausa, S.K. 2007. Activity concentrations of ^{226}Ra ,

^{232}Th , and ^{40}K in different food crops from a high background radiation area in Bitsichi, Jos Plateau, Nigeria. *Biophysics and Biological Physics*, 46(1), pp. 53-59.

Kaleab, B. 2014. Teff: Nutrient composition and health benefits. *International food Policy Research Institute*, 67, pp.1-20.

Khandaker, M.U., 2011. High purity germanium detector in gamma-ray spectrometry. *International Journal of Fundamental Physical Sciences (IJFPS)*, 1(2), pp.42-46.

Kritsananuwat, R., Chanyotha, S., Kranrod, C., and Pengvanich, P. 2014. Transfer Factor of ^{226}Ra , ^{232}Th and ^{40}K from Soil to Alpinia Galangal Plant Grown in Northern Thailand To Cite this Article: IOP Conference Series: *Journal of Physics: Conference Series*, 860(1), pp.1-9.

Kritsananuwat, R., Chanyotha, S., Kranrod, C., and Pengvanich, P. 2014. Transfer factor from soil to alpinia galangal plant grown in northern Thailand to cite this article. IOP Conference Series: *Journal of Physics: Conference Series*, 860, pp. 1-9.

Matthew, T.K., Siti, A., Ab, A., Mayeen, U.K., Asaduzzaman, K., and Yusoff, M.A. 2015. Evaluation of radiological risks due to natural radioactivity around Lynas Advanced Material Plant environment, Kuantan, Pahang, Malaysia. *Environmental Science and Pollution Research*, 22(17), pp.13127-13136.

Mohammad, W., Manzoor, A., and Sajid, I. 2015. Assessment of the risk associated with the gamma-emitting radionuclides from the soil of two cities in Central Karakorum. *Journal of Radioanalytical and Nuclear Chemistry*, 303(1), pp.985-991.

Mohammed, S.A., Mohamad, S.J., Norlaili, A.K., and Nisar, A. 2015. Distribution of ^{226}Ra , ^{232}Th , and ^{40}K in rice plant components and physico-chemical effects of soil on their transportation to grains. *Journal of Radiation Research and Applied Sciences*, 8(3), pp.300-310.

Murat, B., Önder, K., and Yavuz, Ç. 2010. The effects of physicochemical properties on gamma emitting natural radionuclide levels in the soil profile of Istanbul Sayhan Topcuoglu. *Environmental Monitoring and Assessment*, 163(1-4), pp.15-26.

Murtadha, S.H.A., Mohamad, S.J., and Salih, N.F., 2017. Estimation of annual effective dose due to natural radioactivity in ingestion of vegetables from Cameron Highlands, Malaysia. *Environmental Technology and Innovation*, 8(5), pp.96-102.

Nisar, A., 2015. Natural Radioactivity, Radon Concentration and Heavy Metals in Soil and Water in Kedah Malaysia. *PhD Thesis, Doctor of Philosophy, Universitains Malaysia*.

Njinga, R.L., Jonah, S.A., and Gomin, M. 2015. Preliminary investigation of naturally occurring radionuclides in some traditional medicinal plants used in Nigeria. *Journal of Radiation Research and Applied Sciences*, 1(1), pp.1-8.

Okeme, I.C., Hamed, S.O., Olaluwoye, M.O., Araromi, O.I., and Emeje, K.O. 2017. Determination of activity concentration and radiological parameters of natural radionuclides for soil samples from Kogi State University Staff Nursery and Primary School, Kogi State. *Advances in Applied Science Research*, 8(1), pp.36-41.

Ononugbo, C.P., Avwiri, G.O., and Ikhuwui, S.O., 2017. Estimation of natural radioactivity levels in some food spices commonly used in Nigeria and its radiological risks. *Journal of Scientific Research and Reports*, 16(3), pp.1-9.

Rafat, M.A., and Fawzia, A. 2013. Estimation of annual effective dose to the adult Egyptian population due to natural radioactive elements in ingestion of spices. *Advances in Applied Science Research*, 4(5), pp.350-354.

Raymond, L., Njinga, V., and Tshivhase, M., 2016. Lifetime cancer risk due to gamma radioactivity in soils from Tudor Shaft mine environs, South Africa. *Science Direct Journal of Radiation Research and Applied Sciences*, 9(3), pp.310-315.

Rohit, M., and Pankaj, B. 2014. Assessment of radiation hazards due to the concentration of natural radionuclides in the environment. *Environmental Earth Sciences*, 71(2), pp.901-909.

Shafaei, M.A., Saion, E., Wood, K., Naghavi, K., and Rezaee, K.H. 2011. Evaluation of ^{40}K in vegetables collected Malaysia by determination total

potassium using neutron activation analysis. *Journal of Radioanalytical and Nuclear Chemistry*, 288(10), pp.599-602.

Tawalbeh, A.A., Abumurad K.M., Samat, S.B., and Yasir, M.S. 2011. A study of natural radionuclide activities and radiation hazard index in some grains in Jordan. *The Malaysian Journal of Analytical Sciences*, 15(1), pp.61-69.

UNSCEAR. 2000. *Effects of Ionizing Radiation: Report to the General Assembly*. Vol. 2. With Scientific Annexes B, United Nations, New York.

Usikalu, M.R., Akinyemi, M.L., and Achuka, J.A., 2014. Investigation of gamma radiation levels in soil samples collected from some locations in Ogun State, Nigeria. *International Conference on Environment Systems Science and Engineering. IERI Procedia Journal*, 56(9), pp.156-161.

WHO. 2011. *International Food Safety Authorities Network, Information on Nuclear Accidents and Radioactive Contamination of Foods*. 20 Avenue Appia Vol. 30. World Health Organization, 1211 Geneva 27, Switzerland, pp.159-165.

General Information

ARO's Mission: ARO seeks to publish those papers that are most influential in their fields or across fields and that will significantly advance scientific understanding. Selected papers should present novel and broadly important data, syntheses, or concepts. They should merit the recognition by the scientific community and general public provided by publication in ARO, beyond that provided by specialty journals.

We welcome submissions from all fields of natural science and technology, and from any source. We are committed to the prompt evaluation and publication of submitted papers. ARO is published biannually; selected papers are published online ahead of print.

Submission

Manuscripts should be submitted by the correspondent authors of the manuscript via the on-line submission page. Regardless of the source of the word-processing tool, only electronic Word (.doc, .docx, .rtf) files can be submitted on-line. There is no page limit. Only online submissions are accepted to facilitate rapid publication and minimize administrative costs. Submissions by any other one but the authors will not be accepted. The submitting author takes responsibility for the paper during submission and peer review. If for some technical reason submission through the email is not possible, the author can contact ARO.journal@koyauniversity.org for support. Before submitting please check ARO's guide to authors thoroughly to avoid any delay in the review and publication process.

Authors are explicitly responsible for the language of their texts. Paper should be submitted in a well written in understandable English. Authors should not expect the editor or editorial board to rewrite their paper. Prior to submission, authors should have their paper proofread by a possible academic native speaker of English.

- Submit the Article with contact Information
- File name should be your article title
- Don't submit your article in multiple journal, we are taking only minimum time for review process. please don't waste our time
- Once the paper is accepted, it can't be withdrawn
- Please follow publication ethics and regulation
- Avoid plagiarism and copied material
- Strictly Follow ARO's Template

Terms of Submission

Papers must be submitted on the understanding that they have not been published elsewhere and are not currently under consideration by another journal or any other publisher. ARO accepts original articles with novel impacts only. Post conference papers are not accepted "as is", however, regular papers on the same topic but with a different title can be submitted. The new paper should contain significant improvements in terms of extended content, analysis, comparisons with popular methods, results, figures, comments, etc. Please do not forget that the publication of the same or similar material in ARO constitutes the grounds for filing of an (auto) plagiarism case.

The submitting author is responsible for ensuring that the article's publication has been approved by all the other co-authors. It is also the authors' responsibility to ensure that the articles emanating from a particular institution are submitted with the approval of the necessary institution. Only an acknowledgement from the editorial office officially establishes the date of receipt. Further correspondence and proofs will be sent to the author(s) before publication unless otherwise indicated. It is a condition of submission of a paper that the authors permit editing of the

paper for readability. All enquiries concerning the publication of accepted papers should be addressed to aro.journal@koyauniversity.org.

Peer Review

All manuscripts are subject to peer review and are expected to meet standards of academic excellence. Submissions will be considered by an editor and “if not rejected right away” by peer-reviewers, whose identities will remain anonymous to the authors.

Guide to Author

We welcome submissions from all fields of science and from any source. We are committed to the prompt evaluation and publication of submitted papers. Selected papers are published online ahead of print. Authors are encouraged to read the instructions below before submitting their manuscripts. This section arranged into an overview speedy guidelines below and more detailed at the bottom section of this page

Manuscript Preparation

Submitting your manuscript will be in two stages namely before final acceptance and after.

Stage one:

At the first stage manuscript needs to be prepared electronically and submitted online via the online submission page in a Word (.doc, .docx, .rtf) format of one column double-spaced page, Times New Roman font type, and 12 p font size. A pdf version of the submitted manuscript should be submitted too. All authors' names, affiliations, e-mail addresses, and mobile phone numbers should be typed on a cover page, indicating the correspondent author.

Stage two:

- File type: MS-Word version 2003 or later.
- Format: The preferred format of the manuscript two-column template with figures and captions included in the text. This template can be downloaded via the following link. Please follow instructions given in the template; <http://aro.koyauniversity.org/about/submissions#onlineSubmissions>
- Text: All text is in Times New Roman font. The main text is 10-point, abstract is 9-point font and tables, references and captions are 8-point font.
- Figures: Figures should be easily viewed on a computer screen.

Units of Measurement

Units of measurement should be presented simply and concisely using System International (SI) units.

Title and Authorship Information

The following information should be included;

- Paper title.
- Full author names.
- Affiliation.
- Email addresses.

Abstract

The manuscript should contain an abstract. The abstract should be self-contained and citation-free and should not exceed 200 words.

Introduction

This section should be succinct, with no subheadings.

Materials and Methods

This part should contain sufficient detail so that all procedures can be repeated. It can be divided into subsections if several methods are described.

Results and Discussion

This section may each be divided by subheadings or may be combined.

Conclusions

This should clearly explain the main conclusions of the work highlighting its importance and relevance.

Acknowledgements

All acknowledgements (if any) should be included at the very end of the paper before the references and may include supporting grants, presentations, and so forth.

References

References must be included in the manuscript and authors are responsible for the accuracy of references. Manuscripts without them will be returned. ARO is following Harvard System of Referencing. (Learn how to import and use Harvard Styling in your Microsoft Office by following this link:

<http://bibword.codeplex.com/releases/view/15852>)

Preparation of Figures

Upon submission of an article, authors are supposed to include all figures and tables in the PDF file of the manuscript. Figures and tables should be embedded in the manuscript. Figures should be supplied in either vector art formats (Illustrator, EPS, WMF, FreeHand, CorelDraw, PowerPoint, Excel, etc.) or bitmap formats (Photoshop, TIFF, GIF, JPEG, etc.). Bitmap images should be of 300 dpi resolution at least unless the resolution is intentionally set to a lower level for scientific reasons. If a bitmap image has labels, the image and labels should be embedded in separate layers.

Preparation of Tables

Tables should be cited consecutively in the text. Every table must have a descriptive title and if numerical measurements are given, the units should be included in the column heading. Vertical rules should not be used.

Copyright

Open Access authors retain the copyrights of their papers, and all open access articles are distributed under the terms of the Creative Commons Attribution License, which permits unrestricted use, distribution and reproduction in any medium, provided that the original work is properly cited.

The use of general descriptive names, trade names, trademarks, and so forth in this publication, even if not specifically identified, does not imply that these names are not protected by the relevant laws and regulations.

While the advice and information in this journal are believed to be true and accurate on the date of its going to press, neither the authors, the editors, nor the publisher can accept any legal responsibility for any errors or omissions that may be made. The publisher makes no warranty, express or implied, with respect to the material contained herein.

ARO Reviewer/Associate Editor Application Form

ARO is a scientific journal of Koya University (p-ISSN: 2410-9355, e-ISSN: 2307-549X) which aims to offer a novel contribution to the study of Science. The purpose of ARO is twofold: first, it will aim to become an ongoing forum for debate and discussion across the sciences and Engineering. We hope to advance our problem solving capacity and deepen our knowledge regarding a comprehensive range of collective actions. Second, ARO accepts the challenges brought about by multidisciplinary scientific areas and aspires to expand the community of academics who are able to learn from and help to produce advances in a variety of different disciplines.

The Journal is seeking reviewers who can provide constructive analysis of papers thus enhancing overall reputation of the Journal. If any expert is interested in participating of the review process, we highly encourage you to sign up as a reviewer for our Journal and help us improve our presence in domain of your expertise. Appropriate selection of reviewers who have expertise and interest in the domain relevant to each manuscript are essential elements that ensure a timely, productive peer review process. We require proficiency in English.

How to apply

To apply for becoming a reviewer of ARO, please submit the application form by following the link:

<http://aro.koyauniversity.org/user/register>

To apply for becoming a member of the Editorial Board of ARO, please submit the application form by following the link: <http://aro.koyauniversity.org/pages/view/AEB>

Both Associate Editor and Reviewers should specify their areas of research and expertise. Applicants must have a doctorate (or an equivalent degree), and if Master degree they need to have significant publishing experience. Please note that;

- You will need to write your full official name.
- Please provide an email which reflects your official name, such as nameOne.NameTwo@... , or your institute's official email.
- All data need to be written in English.

Note: For more information, kindly visit the following websites:

1. aro.koyauniversity.org.
2. <http://libweb.anglia.ac.uk/referencing/harvard.htm>.
3. <http://bibword.codeplex.com/releases/view/15852>.

INDEXING



Koya University is a young University established in 2003 and it is located in the city of Koya (Koysinjaq), short distance to the East of regional capital city of Erbil (Arbil, Hewlêr) in Kurdistan Region of Iraq. It is on the foothills of beautiful High Mountain. Its campus has been carefully laid out to embrace the beautiful mountainous nature. The Koya University has a Faculty system which enhances the interactions between similar academic fields. Today, Koya University has four Faculties: Engineering, Science and Health, Humanities and Social Sciences and Education in addition to the School of Medicine, which all consist of twenty-five scientific departments in different fields, such as Petroleum Engineering, Geotechnical Engineering, Software Engineering, Physics, Chemistry, Clinical Psychology, Social Science, Medical Microbiology and Sport Education.

ARO-The Scientific Journal of Koya University is a biannual journal of original scientific research, global news, and commentary in the areas of Science and Technology. ARO is a Peer-reviewed Open Access journal with CC BY-NC-SA 4.0 license. It provides immediate, worldwide and barrier-free access to the full text of research articles without requiring a subscription to the journal, and has no article processing charge (APC). ARO Journal seeks to publish those papers that are most influential in their fields or across fields and that will significantly advance scientific understanding. ARO Journal is a member of ROAD and Crossref agencies and has got ESCI, DOAJ seal, SHERPA/RoMEO deposit policy, and LOCKSS archiving policy.



Aro the Scientific Journal Office
Koya University (KOU)
University Park
Danielle Mitterrand Boulevard
Koya KOY45, Kurdistan Region - Iraq